POWDER BED SURFACE QUALITY AND PARTICLE SIZE DISTRIBUTION FOR METAL ADDITIVE MANUFACTURING AND COMPARISON WITH DISCRETE ELEMENT MODEL

A Thesis

presented to

the Faculty of California Polytechnic State University,

San Luis Obispo

In Partial Fulfillment

of the Requirements for the Degree

Master of Science in Mechanical Engineering

by

Irene Yee

March 2018

COMMITTEE MEMBERSHIP

TITLE:	Powder Bed Surface Quality and Particle Size Distribution for Metal Additive Manufacturing and Comparison with Discrete Element Model
AUTHOR:	Irene Yee
DATE SUBMITTED:	March 2018
COMMITTEE CHAIR:	Andrew Davol, Ph. D Professor of Mechanical Engineering
COMMITTEE MEMBER:	Xuan Wang, Ph. D Professor of Industrial and Manufacturing Engineering
COMMITTEE MEMBER:	Hans C. Mayer, Ph. D Professor of Mechanical Engineering

ABSTRACT

Powder Bed Surface Quality and Particle Size Distribution for Metal Additive Manufacturing and Comparison with Discrete Element Model

Irene Yee

Metal additive manufacturing (AM) can produce complex parts that were once considered impossible or too costly to fabricate using conventional machining techniques, making AM machines an exceptional tool for rapid prototyping, one-off parts, and labor-intensive geometries. Due to the growing popularity of this technology, especially in the defense and medical industries, more researchers are looking into the physics and mechanics behind the AM process. Many factors and parameters contribute to the overall quality of a part, one of them being the powder bed itself. So far, little investigation has been dedicated to the behavior of the powder in the powder bed during the lasering process. A powder spreading machine that simulates the powder bed fusion process without the laser was designed by Lawrence Livermore National Laboratory and was built as a platform to observe powder characteristics. The focus for this project was surface roughness and particle size distribution (PSD), and how dose rate and coating speed affect the results. Images of the 316L stainless steel powder on the spreading device at multiple layers were taken and processed and analyzed in MATLAB to access surface quality of each region. Powder from nine regions of the build plate were also sampled and counted to determine regional particle size distribution. As a comparison, a simulation was developed to mimic the adhesive behavior of the powder, and to observe how powder distributes powder when spread.

ACKNOWLEDGMENTS

I would first like to thank Dr. Davol for being the calm and collected advisor that I needed for this thesis. Your guidance always put me right back on track while your positivity calmed my nerves. I would like to thank Dr. Mayer for always asking the questions that push me to keep thinking and improving. From you, I have learned to take pride in my work. I would also like to thank Dr. Wang for all of his support throughout this project. I am grateful for the opportunities and encouragement you provided and your willingness to help at a moment's notice.

Thank you to Lawrence Livermore National Laboratory for giving me this wonderful opportunity and for providing other opportunities at Cal Poly for students to explore the learn-by-doing motto. To the amazing and brilliant people at LLNL who made this thesis possible, Thomas Pluschkell, Matt Roberts, Carlos Esquivel, Matt Wraith, Steve Burke, Ann Mycroft, Stephen Knaus, Manuel Iniguez, and Otis Walton, thank you for bringing your curiosity, enthusiasm, and experience to this project.

I have endless thanks to give to my family for their love and encouragement of everything I pursue. I especially want to thank my Dad for everything he has done and sacrificed so that Kelly, Warren, and I can have the best future possible.

Thank you to Emily Woods, Judy Lantaca, Nathan Harry, Adam Menashe, Tyler Price, Vivian Fong, and Kim Tran for your friendship and words of affirmation. Each one of you made me feel at home no matter where I was, and I could not have asked for better friends to anchor me through my graduate year.

Finally, I would like to thank Grant Pocklington for his patience, understanding, care, and unwavering support. Your willingness to do anything and everything to make sure my sanity was in check was very much appreciated, and I really could not have completed this thesis without you.

TABLE OF CONTENTS

Page

LIST OF TABLES

Page

LIST OF FIGURES

Page

NOMENCLATURE

h	=	Layer height …….	μm
d	=	Dose rate …….....	-
v	=	Coating speed …….....	mm/s
Ra	=	Roughness average …….....	μm
RMS	=	Root mean square roughness…….	μm
m	=	Mass ……..	kg
m^*	=	Effective mass ……...	kg
f_c^i	=	Contact force acting on particle i …….	N
I	=	Moment of inertia …….	Kg-m^2
ω	=	Angular velocity……	rad/s
t	=	Total torque on a particle …….….	N-m
F	=	Total force …….	N
k	=	Hertz stiffness ……...	-
δ	=	Particle overlap …….	μm
v	=	Relative velocity ……...	m/s
E	=	Young's Modulus …….	Pa
E^*	=	Effective Young's Modulus …….....	Pa
a	=	Contact radius ……...	μm
β	=	Damping ratio ……...	-
e	=	Coefficient of restitution ……...	-
r	=	Particle radius ……...	μm
G	=	Shear modulus …….....	Pa
ν	=	Poisson's ratio …….....	-
A	=	Contact area …….....	m^2
k_{CED}	=	Cohesive Energy Density …….	J/m^3
ρ	=	Density …….	kg/m^3
$dt_{rayleigh}$	=	Rayleigh time ……	μs

1. INTRODUCTION

Additive manufacturing (AM) has emerged as a popular manufacturing process in the last decade due to its ability to produce complex parts faster and more efficiently than traditional methods. As opposed to removing material from a solid block to reveal a part, additive manufacturing joins material together in layers to form a predesigned shape. A variety of materials including polymers, metals, ceramics, composites, and biological materials can be used with this method [1]. AM technology has allowed scientists to model research ideas, doctors to replicate body geometries to prepare for surgeries, and hobbyists to create in the comfort of their own homes.

1.1 Additive Manufacturing Basics

The most familiar example of additive manufacturing is the plastic 3D printer. These machines are readily available on the market starting at just a couple hundred dollars and are compact enough to fit on a desk. With the aid of a computer design program, any object that can be modeled can also be printed. The digital model is then "sliced" into layers in preparation for printing. Many methods of printing are available, but the most common technique is fusion deposition modeling in which plastic filament is heated and extruded through a nozzle onto a platform in roughly 0.15mm layers that stack to form a 3D shape [2,3].

In medical, aerospace, and automotive industries, metal is another popular AM material. Almost any metal alloy or pure element that can be melted is suitable for this process. Powders made for metal AM are typically made using gas atomization, which produces highly spherical particles that densely pack when printing (see Fig. 1-1). Metal is

melted in a vacuum chamber, and once the metal leaves the nozzle, jets of inert gas shear the liquid metal into fine droplets that disperse and cool into solid spheres as they fall to the bottom of the chamber [4]. The powder particle size produced can range from 10μm to 100μm and the powder is sieved to achieve the desired range for proper flow for a particular machine or application.

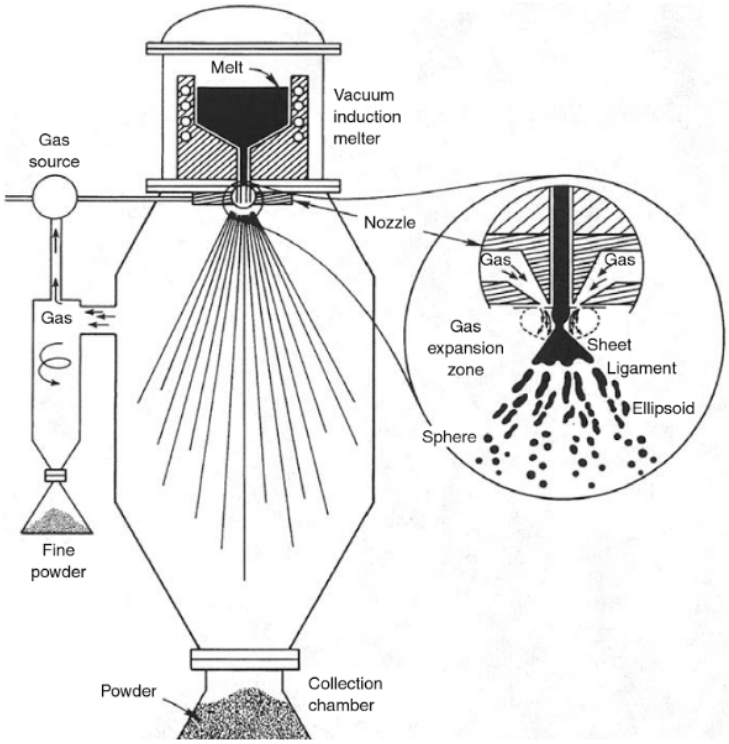

Figure 1-1. Apparatus for gas atomization. [5]

With metal AM, different methods of fabrication such as powder bed fusion, direct energy deposition, and binder jetting all have the same basic steps, whether the method uses powder or wire [6]. Currently, Lawrence Livermore National Laboratory (LLNL) is using the powder bed fusion (PBF) process to print metal parts using the selective laser melting technique (SLM). Generally, a PBF system works by using a blade to rake or a

roller to compress powder over the build area. The build platform is lowered by a distance (around 10 to 50 microns when used with a distribution of particles from 10 to 100 microns) and the powder platform is lifted 2 to 4 times the layer height to ensure the powder supplied can distribute over the entire build plate when the recoating blade pushes the powder over. An energy source, an electron beam or laser beam, melts the powder into a 2D shape and penetrates a couple of layers deep, as presented in Fig. 1-2. This process repeats until a solid three-dimensional part is produced [7].

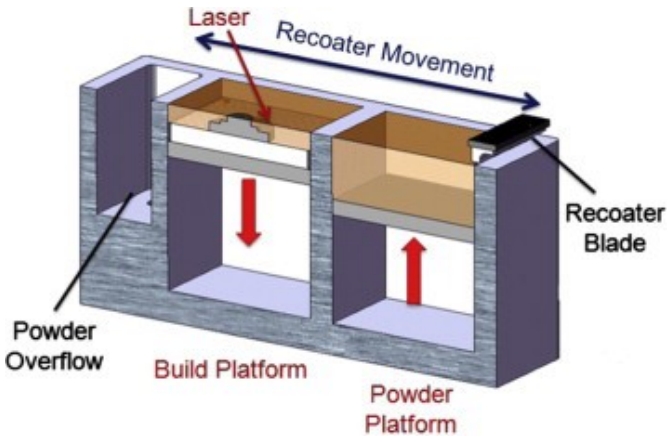

Figure 1-2. Powder bed fusion process with recoating blade to rake powder over to the build platform [8].

1.2 Advantages and Disadvantages of Additive Manufacturing

The appeal of AM for industry and for the average consumer is that if a customized part is needed, that part can be designed and printed at home or at work, possibly within the span of a day. Usually, if a custom part is desired, a drawing with specified dimensions would be sent out to a machine shop, and after a few weeks the part would be completed and delivered. In manufacturing, the largest percentage of cost for a part comes from labor, which makes revising a design and producing another prototype expensive. A traditionally manufactured part needs to undergo multiple processes in order to be completed, whereas

with AM, one process builds the part to near completion. The only time spent on labor when using an AM machine is preparing the design file for print and setting up the machine. The rest of the work is done by the computer, resulting in lower production costs. In addition, the turn-around time for AM is much faster than for conventional machining, allowing parts to be iterated many times over, making AM printers a preferred tool for rapid prototyping.

This technology gives way to new opportunities in design, as designers are not limited to the capabilities of conventional methods, such as using a mill or a lathe [9]. Intricate internal cavities and complicated geometries that would otherwise be unattainable or too costly are now possible with AM. Complete, nested assemblies can be printed in one go instead of making each individual part and joining them together. Assemblies can be reduced into fewer parts by printing in live features such as hinges or chain links. These opportunities in design lead to part optimization by reducing excess material. Another area for customization is materials, which can be combined to improve strength and flow properties. Though an AM part still requires finishing operations to reach final dimensions, the part is close to the final shape with less overall material waste than if completed with material removal processes.

For most companies, the uncertainty of quality is what prevents them from adopting AM for mass production. Owning an AM machine requires extensive testing and engineering to guarantee a part will print as expected with consistency. Parameters need to be experimented with to determine the best recipe to prevent poor surface finish, warping, residual stresses, cracks, and porosity, which can all cause a part to fail during a print. Machines currently lack a method of detecting failure, allowing prints to continue only to

be discovered unusable at the end [10]. AM is also not suitable for large scale production or simple operations since modern chain manufacturing will always produce parts more cost effectively and efficiently than printing one part at a time with AM.

1.3 Objective

LLNL wants to understand the AM process better to improve the quality of parts and to expand on the capabilities of the process itself. They are exploring the design of lightweight, high strength, and optimally shaped components, and refining the AM process would allow them to build such structures more reliably and with better quality control [11]. This thesis is to support the efforts made by the LLNL in this field.

Research about AM has mostly focused on simulating and analyzing the lasering process, with an emphasis on energy absorption, melt pool behavior, residual stresses, distortion, and thermal conditions [12]. Parameters that contribute to the results of the print, such as laser power, coating speed, layer thickness, etc. have also been studied for the best results. These characteristics have been investigated and modeled, but one area which is still not well understood is the behavior of powder as it spreads across the build plate, as well as the powder bed conditions. Tests for particle distribution and flow behavior for metal powders do exist, but most tend to be off the build plate under different conditions. By studying the powder properties across the print bed, the results may bring to attention how the process can be improved or controlled.

To analyze the effects of the coating process, LLNL has built a machine that replicates the PBF spreading process. This powder spreader performs the process without taking time away from production machines that are used for manufacturing. Since the laser is absent, the spreader is easily portable and only requires the use of a fume hood.

This also means that the powder will be spreading over unfused layers since a part cannot be built. The primary difference between realistic manufacturing conditions is that the spreading process will not be performed under an inert gas which might produce different cohesion properties but conducting the experiment in air should be sufficient for testing.

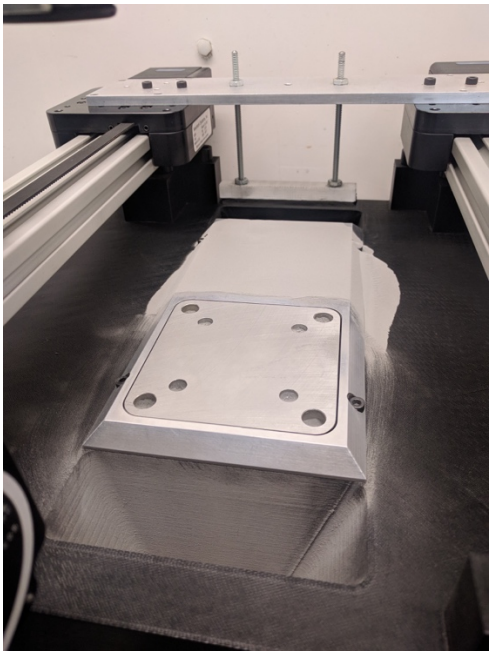

Figure 1-3. Build plate (front) and powder supply (back) from the powder spreading machine designed by LLNL to replicate the powder bed fusion process.

The main characteristics of interest for this project were particle size distribution and surface roughness, since these were the two characteristics that could be evaluated using the powder spreading machine. The surface roughness and particle size distribution were analyzed with changes in dose rate and blade speed to see how these controllable parameters affect the powder bed. Since the behavior of powder was difficult to visualize, a discrete element simulation was also be created to provide additional insight into the spreading process and to compare with the experiment to see if similar results were produced.

2. LITERATURE AND BACKGROUND

The current need in metal AM machines is an in-situ metrology process that can detect defects such as fractures, warping, and porosity, and stop the machine from continuing, or adjust machine parameters based on observations, since current machines do not provide feedback [7]. But for that to be realized, there needs to be an understanding of how changes in certain factors affect the final product. The PBF process involves a large number of input parameters and factors, which makes controlling the final dimensions and material properties difficult. Extensive testing is required to predict how the input, process, and environmental parameters such as laser parameters, scan patterns, build environment (inert gas), or the humidity of a particular day affect the outcome. One input that could be better understood is the behavior of powder, especially during the spreading process, since the packing and distribution of the particles can contribute to the macroscopic characteristics of the finished part.

2.1 Tests for Evaluating Powder Properties

Powder characteristics are important for ensuring repeatable metal AM parts. Typically, AM machine vendors specify powder size, distribution, shape, and handling for the best performance. Powders used for AM are usually assumed to be spherical with a unimodal particle size distribution for good packing in a powder bed, and sufficient mechanical properties that can be achieved at near full density. The metal powder that was used for the powder spreading tests in this thesis was 316L stainless steel (316L SS), which is a common powder material for metal additive manufacturing. The material is made of nickel, chromium, molybdenum, iron, copper and manganese in proportions defined in Table 2-1. The powder particles ranged from 10 microns to 60 microns in diameter. The

powder distribution and range can vary depending on the technique of metal AM being used. Part quality is significantly affected by the particle size distribution, shape, and how well the powders blend together for use.

Table 2-1. Metals present in the 316L SS powder and composition provided by the manufacturer.

Metal	Percentage
Nickel	3-14%
Chromium	1-20%
Iron	40-95%
Molybdenum	1-4%
Copper	0-4%
Manganese	0-2%

Any test should begin with powder sampling, since measuring an entire batch of powder is impractical. Ideally, powder should be sampled while in motion, poured or tumbled, to ensure that the sample collected represents the distribution in the batch. If the powder cannot be poured, static samples can be obtained with a "sample thief" tool at multiple locations, see Fig. 2-1. In the case of the experiment for this thesis, a sample thief was too large and was not available, so as much powder as possible was scooped into a vial, and then resampled when tested. In addition to defining sampling techniques, the National Institute of Standards and Technology (NIST) is making efforts to develop standards and procedures for additive manufacturing materials and measurement methods to characterize powder. In [13], test methods for identifying size, morphology, composition, density, flow, and thermal properties of powder are listed.

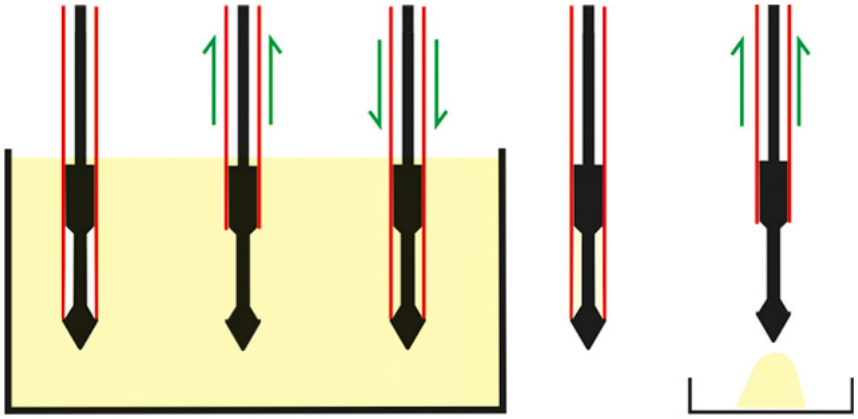

Figure 2-1. A sample thief is placed in a batch of powder. The sheath is opened, and powder is trapped and removed from the batch. *Sample Powder Thief.* QAQC LAB.

One of the powder characteristics observed in the experiment is the particle size distribution of the powder bed. Particle size is an important factor that dictates the minimum layer thickness when the powder is spread across the build plate. The simplest method of determining particle size distribution is sieve analysis, in which the sample is shaken through sieves until the amount left is constant, and the particle count for each mesh size is determined. Powder size can also be evaluated optically with a scanning electron microscope, transmission electron microscope, or an optical light microscope [13,14]. Imaging using X-ray computer tomography (CT), a method in which a sample is embedded in epoxy, scanned at many different angles, and then recreated as a 3D structure, can also determine particle size and morphology [14]. Some devices use laser diffraction which determines particle size by analyzing the light scattered at different angles by the particles and correlating the results to the Mie theory of light scattering [13,14].

Though there are many ways to characterize the bulk properties of powders, the main densities to look at are bulk density and tapped density [15]. Bulk density, also known as apparent density, is the mass of the material divided by the total occupied volume which

includes pores and interparticle voids. This value can be calculated by filling a graduated cylinder with a known mass of material, or by using a Hall flowmeter funnel or a Carney flowmeter funnel as discussed in [13]. This value is often difficult to repeat, since the slightest disturbance can result in a different bulk density measurement. Handling also plays a significant part in the bulk density, since packing can cause a range of bulk densities. Tapped density is obtained by mechanically tapping the container of bulk powder until the volume sees little change and dividing the mass by the resulting volume. Comparing the tapped density to the bulk density provides valuable information about the interparticle interactions that are present in bulk properties that resist powder flow. The powder's flowability can be quantified using the Hausner Ratio, defined as the ratio of the tapped density and the bulk density measured according to ASTM D781-09 [16], which gives insight into the flowability and cohesiveness of a powder. The size distribution and the morphology of particles influence how particles pack together, since spherical power particles can achieve high densities and finer particles can fill in voids between larger particles. Though this project did not involve density experiments due to the limitations of the powder spreader, density is an important factor that should be tested extensively in the future.

Measuring density and particle size distribution directly from a PBF system is especially difficult because the above methods do not reflect the ways in which the powder is used, and as such, may not represent the density or distribution formed by spreading powder in layers. Jacob et al. [17] uses the term powder bed density to differentiate from packing, tap, and apparent density definitions used to measure bulk powders. They developed an in-situ method to powder bed density directly inside a PBF machine by

building a cylindrical container that would encase and protect powder samples at multiple regions of the build area. The thin walled top was punctured and the powder inside was poured out, for mass and volume calculation, and they saw that the powder bed density increased away from the dispenser bin, but only with a 0.3% difference. Other than Jacob et al., very few researchers have evaluated the true characteristics of the powder bed.

2.2 Imaging Methods for Surface Roughness

The preferred method for this thesis to identify surface roughness would be a non-contacting measuring method, such as scattered light or interferometry. Surface texture or roughness is defined by Ra, the average of the surface microscopic peaks and valleys, or RMS, the root mean square roughness. Ra is the most common measurement, but is not sensitive to large peaks and valleys that might be present, unlike RMS. To calculate Ra,

$$Ra = \frac{1}{l}\int_0^l Z(x)dx \tag{2-1}$$

where l is the length evaluated, and Z is the heights along the length. Alternatively, the RMS value is calculated by:

$$RMS = \sqrt{\frac{1}{l}\int_0^l Z(x)^2 dx} \tag{5-3}$$

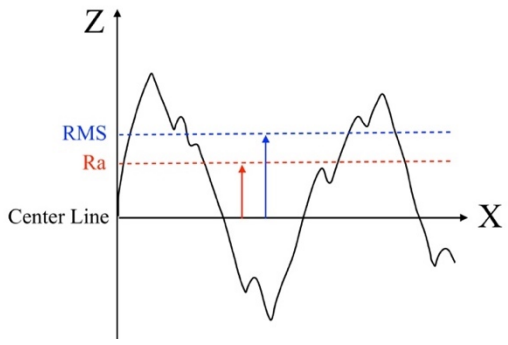

Figure 2-2. How Ra and RMS are measured with a surface profile.

Traditionally these measurements are made by a profilometer which uses a stylus or probe that runs along a surface to detect distances and generates a profile that shows the various heights up to microns. The disadvantage of something like this is that a stylus would damage the profile of a powdered surface and typically requires the object or sample to fit on a slide, which is the same reason why an interferometer was also not considered.

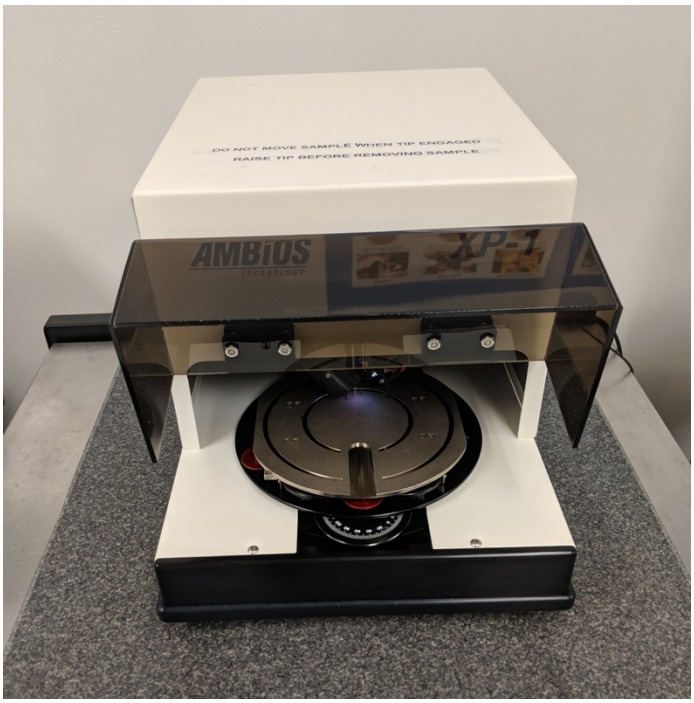

Figure 2-3. AMBiOS XP-1 profilometer used for a sandpaper test in 4.4.1.

Kayahan et al. [18] proposed a method called statistical properties of binary images to obtain surface roughness measurements based on binary speckle images from a laser on a metal surface. When a laser, which is composed of coherent light, is directed onto a surface, the light scattered creates a speckle pattern with bright and dark regions. They implemented this method to find a relationship between the bright and dark regions and surface roughness, which could hold potential as an in-process measurement technique. They showed that as the normalized brightness to dark ratio decreased, the roughness increased as a first order exponential decay function. Several other studies have

implemented a similar method in determining surface roughness using light scattering [19-21]. Even though most of the research on binary speckle pattern imaging uses coherent light which was not available, the same principles and techniques were tried and experimented with in this project.

2.3 Simulations

Much of the research for additive manufacturing focuses on the temperature distribution and stresses developed during the sintering or melting process and uses the finite element method for simulation [22]. Finite element works for observing macro level stresses, strains, and temperatures of a solid body, but does not work for analyzing the micro-mechanical interactions between discontinuous materials such as powder particles. The discrete element method (DEM) has been the most popular method amongst studies for simulating powder bed particle phenomena [23]. DEM is a numerical method for modeling the dynamics of solid particles, which involves solving Newton's equations of motion, translational and rotational, for every powder particle at each timestep, and the contact forces are calculated using contact models.

Some have looked at particle distributions and random packing without the influence of a blade or a roller to understand how the distribution alone might affect the density of the powder bed in an effort to choose optimal parameters. Xiang et al. [24] focused on particle packing using three different size distributions: monosize, bimodal, and Gaussian in various layer thicknesses, randomly packed in a defined space. They used DEM and a nonlinear Hertzian contact model for their simulation. Particles were randomly packed together and layered in different thicknesses. The resulting packing density, the total volume of particles divided by space volume, and coordination number, which is a

good indication of porosity, was observed. They found that the initial packing density and coordination number of the monosize distribution was the largest for every layer thickness, and that as layer thickness increased, the packing density increased for every distribution and trended towards being stable. After the initial layer was compressed 20 microns, the different size distributions showed relatively small differences in packing density (60-63%) and become relatively stable with increasing layer thickness. The compressed packing density was quite an increase from the uncompressed powder bed initially, especially with the smaller layer thicknesses. Zhou et al [26] performed similar powder packing simulations using a sequential addition packing algorithm but achieved different results. Compared to monosized packing, their results showed that a bimodal distribution increases packing density and average coordination number is decreased. Ganeriwala et al. [25] did a reduced order discrete element model to simulate deposition and particle to underneath substrate interactions were modeled with finite difference method to reduce computations times to allow for more process optimization exploration. The particles were dropped into the domain by gravity onto a layer similar to [26] and the rain model used in [27], since they believed it was sufficient assuming that powder is not compressed during deposition by a blade or a roller. With their coupled discrete element – finite difference model, they showed that while bimodal distribution should increase loose bed density, the smaller particles may vaporize during the scanning process, causing gas bubbles that would decrease final density and strength.

Others have chosen to simulate the spreading process with a blade or a roller pushing the powder over the build plate. Parteli and Poschel [28] ran DEM simulations to investigate powder layer characteristics using a roller as a coater to distribute PA12

powder. They integrated adhesion and van der Waals forces, complex particles, and a viscoelastic model to the DEM library in LIGGGHTS, a DEM solver. From their simulations, higher process speed produced looser packing with larger voids between particles and ripples on the surface. They also experimented with different size distributions, which surprisingly showed that a coarser distribution resulted in a smaller surface roughness value. This could be due to smaller particles forming larger agglomerates. Herbold et al. [29] at LLNL has been investigating powder-bed simulations for additive manufacturing as well. They used truncated size distributions that reflected a realistic sample set and a minimum simulation sample size of 40 particles square by 10 particles deep in order to shorten run time and to demonstrate the capability of DEM simulations to generate realistic powder bed based on size segregation and packing distributions.

Key differences in the approaches of some of these simulations lies in the powder characterization and the contact model chosen. Some of the research mentioned above [24,25] used a Hertzian model, which, when used alone, does not account for adhesion of van der Waals forces acing on deformable spheres that is in the JKR model used by [28,29]. Most simulations also use spherical particles, which are a good approximation of AM powders based on photos from SEM [29], but for other powders, such as the PA12 powder used by Parteli and Poschel, it is not accurate.

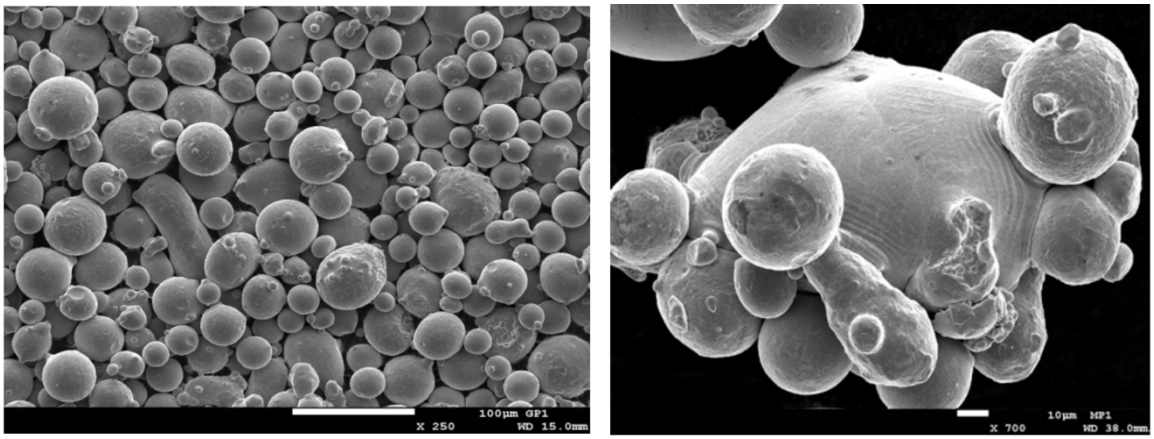

Figure 2-4. SEM images of recycled stainless steel powder (left). Some large agglomerate particles are also present in recycled powder (right). [29]

To account for the shape, Parteli and Poschel incorporated a model for creating more complex powder particles by combining spheres. The total force was the sum of the forces on all spheres that make up the composite particle and the moment of inertia was computed by removing the contribution of the overlapped volume. Haeri et al. [30] also decided to look at non-spherical shapes and focused on rod-shaped particles with different aspect ratios to simulate milled PEK/PEEK. They discovered that larger particle aspect ratios or faster spreader translational velocity resulted in worse surface roughness and less density, which would mean poor mechanical performance. For rollers, the max volume fraction was at an aspect ratio of 1.5, and improves with a lower roller velocity, but too slow of a velocity would be impractical for production. They investigated both roller and blade as a coater and found that a roller outperforms a blade in terms of surface roughness due to the contact dynamics at play and how the roller provides a large contact area. Also, mixing different distributions to control bed quality did not seem to work due to minimal particle segregation at each layer.

Most of these research papers lack experimental results to validate predictions from simulations. Haeri et al. preformed experiments to observe particle alignment, but no experiment has been found so far that observes powder density or surface roughness in-situ. Also, one factor that has not been observed is how dosage rate of supply powder might affect the powder bed. When powder is spread over, not all the powder makes it to the build plate since powder tends to spill over to the sides. The goal of this thesis project is to provide experimental data for the powder spreading process and to see if the results match a DEM simulation that mimics the use of the powder spreader.

3. EXPERIMENT SETUP

LLNL designed a machine to mimic the powder spreading of the PBF process. This device allowed for the study of powder behavior during the deposition process without the space and power requirements of a complete machine with a laser. The machine distributed a layer of powder over a plate at a specified thickness, with a desired powder dosage rate and blade velocity.

The powder spreading machine was significantly smaller than a full-sized machine, which made the machine portable. The mechanisms of the powder spreading machine for raising the build plate and supply area and for moving the coating blade were very similar to the actual inner workings of a full-sized machine, and with the same resolution of movement. Any kind of testing setup could be used with the machine since there were no walls surrounding the build area, unlike with full-sized machines. Not having walls also allowed for easy visibility and access to the powder bed.

3.1 Replica Design

The powder spreader consisted of two 90 mm x 90 mm plates that were bolted onto spacers. One plate of the powder spreader was the build plate, and the other formed the base of the supply well. A felt ring between each build plate and spacer prevented powder from falling through. The elevators sat on top of the vertical stages from Newmark Systems Inc. that incremented the height of the build plates to the desired layer thickness. The resolution of each vertical stage was 31.946 steps per micron, as specified by the manufacturer. The two assemblies sat in a center insert that was held up by a 3D printed

plastic housing. Plastic shims were placed underneath the build plates for leveling. On top of the housing were two belt drives that were placed on each side of the build plate and was adjusted for distance and speed. The belt drives had a resolution of 277.75 steps per millimeter. An aluminum plate bridged the belt drives and held the coating blade. The blade was made from rubber and was slightly longer than the width of the build plate. The blade tapered down with the bottom edge being the narrowest. The blade was set at around 500 microns from the top of the build plate by running a plastic shim across the span of the blade. The vertical stages and belt drives were connected to a motor controller that used a program called Galiltools. Sample code used to run the stages and drives can be seen in Appendix A. A diagram of the set up can be seen in Fig. 3-4.

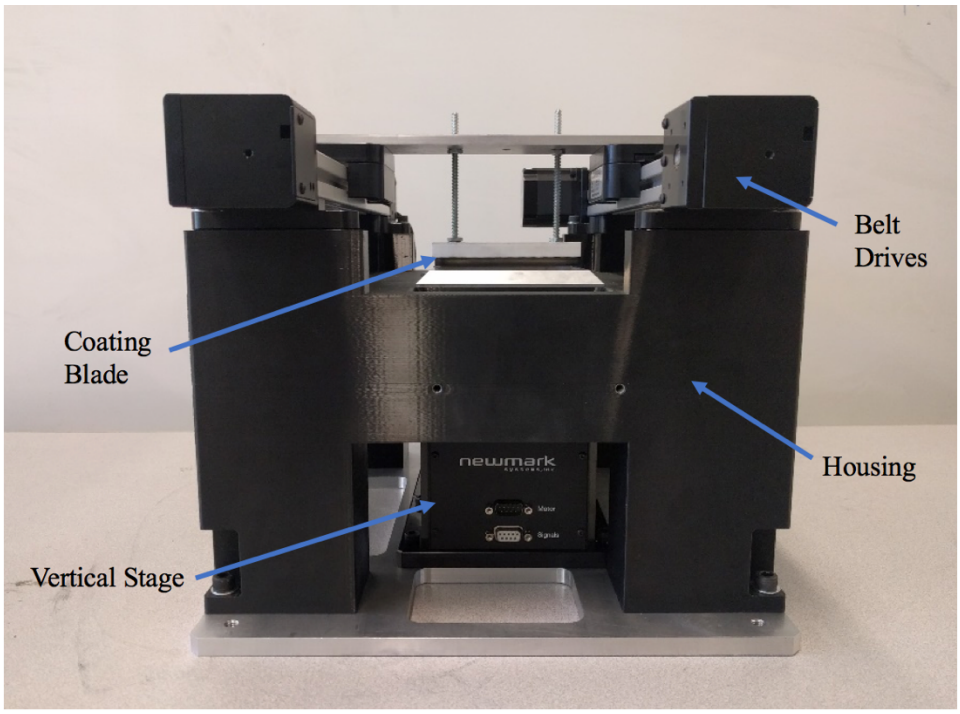

Figure 3-1. Assembled powder spreader used to conduct testing.

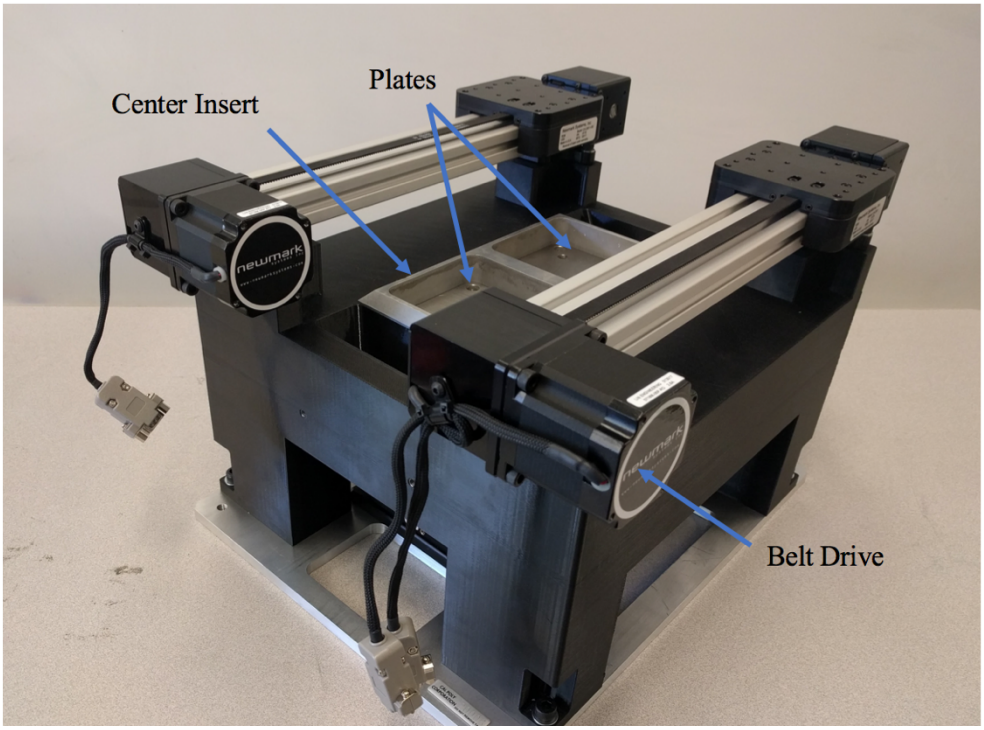

Figure 3-2. Powder spreader top view showing the center insert that holds the plates that form the base of the build and supply sections.

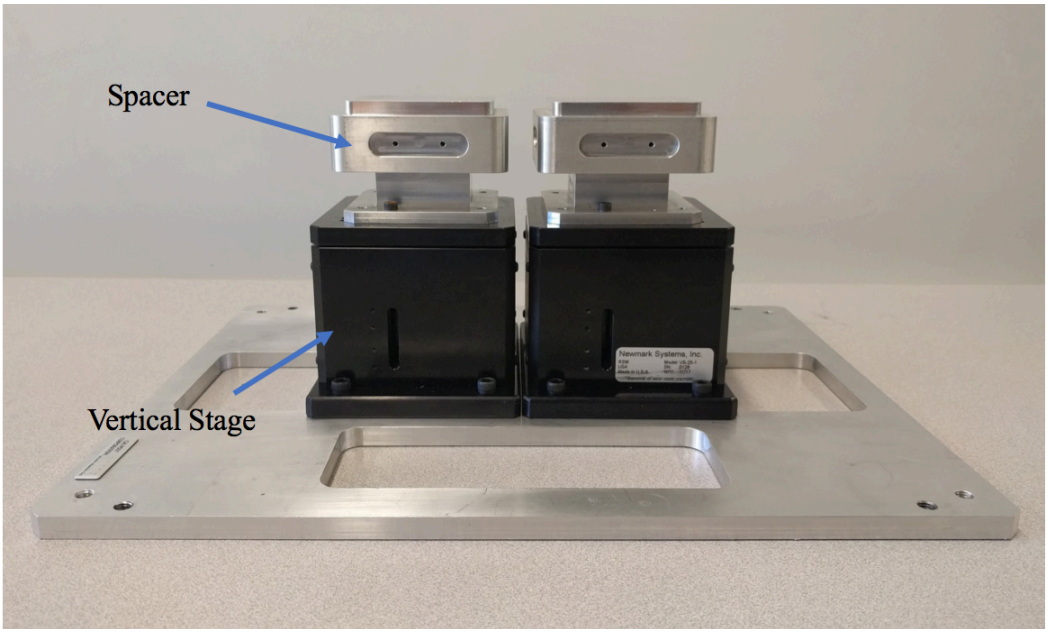

Figure 3-3. Internal components of the powder spreader. Below the build plates are spacers on vertical stages adjust the build plates to the proper height.

3.2 Camera Setup

For imaging, a Mikrotron 1362 camera was attached to a frame such that the lens faced downward for taking photos of the build plate. This camera took images in grayscale and only captured a small area of the build plate. The frame that supports the camera was bolted to an X-Y stage to allow the camera to move to different areas of the build plate, which is seen in Fig. 3-4. A Nikon Macro DX lens was used with the height of the camera adjusted to match the minimal focal distance of 40mm. The macro camera lens that was used was unable to capture individual powder particles themselves, but was able to identify clusters of them, which still provided qualitative insight about the surface quality of the bed. Operating the camera required a National Instruments PCI-e card and a LabVIEW VI was created to save images from the camera. The LabVIEW VI was designed to keep the footage rolling while screenshots were taken. Further details of the installation and usage of the camera can be found in the Appendix A.

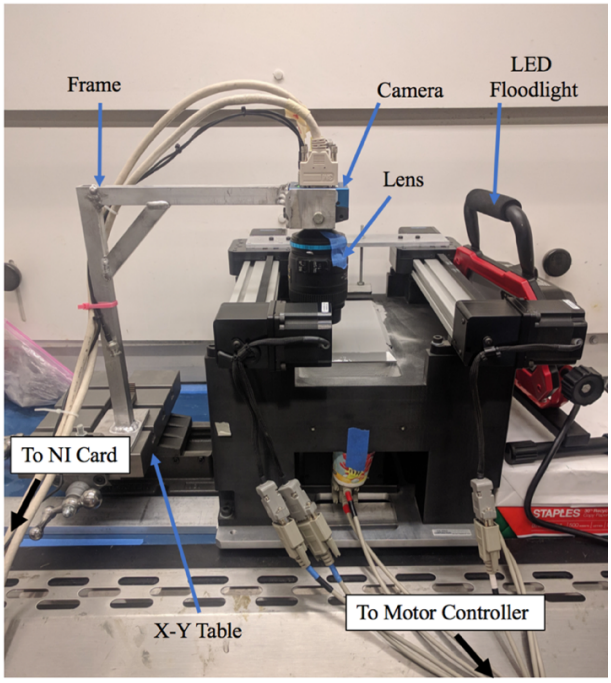

Figure 3-4. Setup of experiment to take images of the powder bed surface.

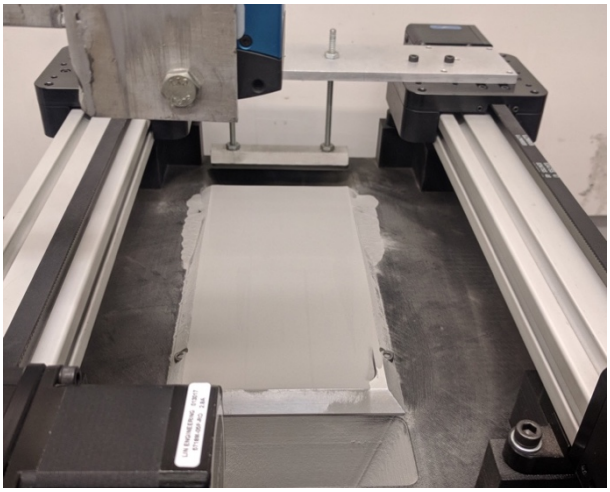

Figure 3-5. Powder spread across the build plate.

3.3 Lighting

Proper lighting for this experiment was crucial given the fine grain size and smooth texture of the powder. Because the images were in grayscale, high contrast was needed in order for the powder texture to stand out. To determine the proper lighting, images were taken with the light placed at various locations around the build plate.

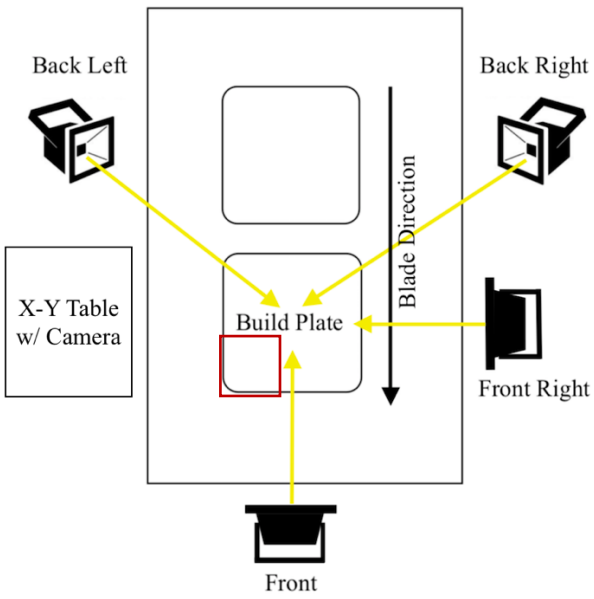

Figure 3-6. Top view of powder spreader with locations of the LED light tested for best lighting angle on the build plate. The red square indicates the location of Fig. 3-7.

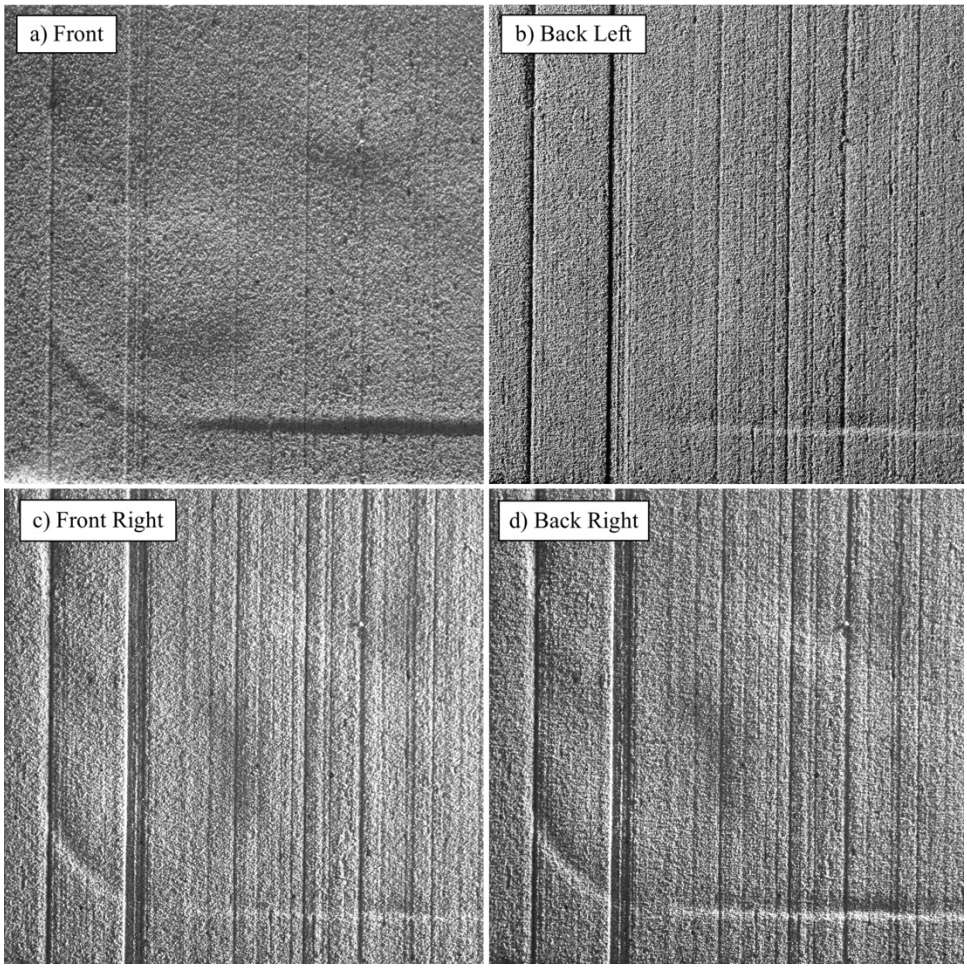

Figure 3-7. Images of a section of the powder bed with the light at various locations shown in Fig. 3-6. The front and back left showed little contrast and detail compared to the images taken from the right.

Though not shown above, lighting from overhead was also tested. This location did not yield good results as the image was too dark and little could be identified, since the light was blocked by the camera. Figure 3-7b, which was lit from the back left, was missing details found in the images that were lit on the right (Fig. 3-7c and d), though it had the best contrast of the four. The best option was to light the powder bed from the side opposite the camera on the right, since the details of the powder bed were more apparent from this angle. Fig. 3-7d showed more contrast than the front right as the front right image appeared a bit more washed out, although they both show the same details. Consequently, the front right was the better location for the light since the aperture could be lowered for better

image sharpness and higher contrast. To maintain consistent lighting, the light would have to move with the camera. As the camera traveled further away, the images became washed out by the harshness of the light. To compensate, the light was kept roughly 8" away from the camera. Images with the light ± ½" did not show any significant difference. In an ideal setup, the lighting would be through the lens to provide consistent, ample lighting, similar to a microscope.

An LED floodlight made by Snap-on provided an adequate amount of light needed to illuminate the powder bed. The camera worked best with the lens at the smallest aperture such that the majority of the image was in focus, however, the floodlight could not produce enough light for a lower aperture. As a result, the f-stop that worked best was about f/4, although the peripheral regions of the images were still not well focused. To compensate, photos were cropped in to the focused region during image processing.

3.4 Safety and Personal Protection Equipment

This thesis pertains specifically to 316L SS powder, which requires certain handling procedures. A safety operation procedure (SOP) was written for tests using this powder, and can be seen in Appendix B. Potential hazards, health effects, first aid procedures, and waste disposal are outlined in the document, which was approved by Environmental Health and Safety (EH&S) at Cal Poly. All handling of the powder and experiments were done under a fume hood. Gloves, safety glasses, and a lab coat were worn as personal protection equipment (PPE) by persons in the room when powder was used in order to prevent skin contact with fine particles. Respirators were used when not operating under the fume hood.

3.5 Test Plan

The goal of this study was to observe the characteristics of the powder bed, specifically the surface roughness of each layer, and the particle size distribution. To understand the behavior of powder during spreading, two parameters were analyzed with respect to their influence on particle deposition on the build plate: scan speed and dose rate.

3.5.1 Photoanalysis

This first test performed was photoanalysis of the build plate for surface roughness. The contrast between the hills and the valleys indicated the surface quality on the plate. The build plate was lowered by 30μm, which was the specified layer thickness for all runs. The supply well was then lifted by a specified dose rate times the layer thickness (e.g. 3x dose rate for a 30μm layer height means a 90μm lift). The blade was swept from the supply well to the build plate, pushing the powder over to coat at a specified speed. This was continued until the build plate became completely covered. The camera was moved around using the X-Y table to take photos from 9 regions of the build plate. Nine photos were taken for each layer for each of the 4 layers. This test was done for 2x, 3x, and 4x dosage, at speeds of 100 mm/s and 200 mm/s to test for differences in particle distribution.

Table 3-1. Experimental conditions tested for each run using the powder spreading machine and the corresponding number of runs.

Dose Rate [-]	Speed [mm/s]	Runs [-]
2	100	2
2	200	1
3	100	2
3	200	1
4	100	2
4	200	1

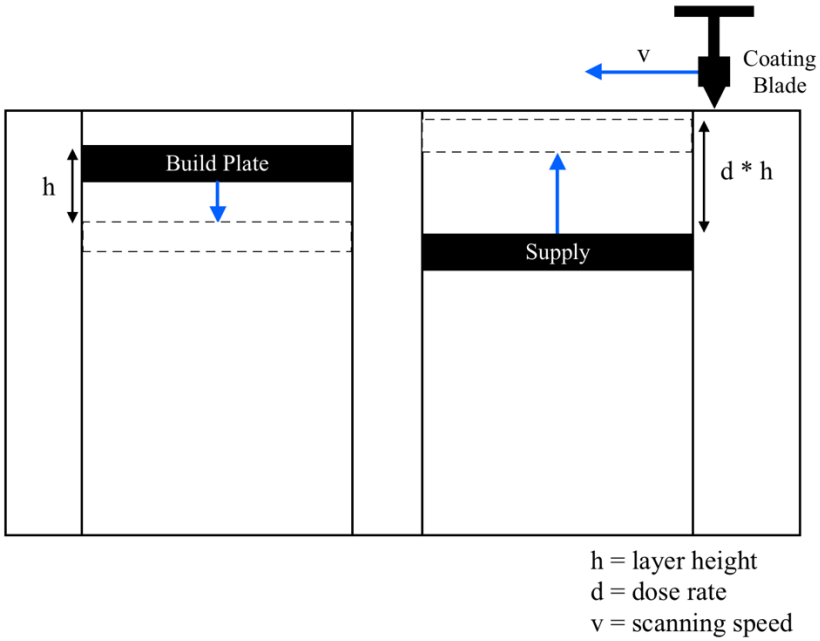

Figure 3-8. The build plate lowers incrementally at a desired layer height and the supply of powder is lifted by a multiple of the layer height. The scan speed is the speed of the coating blade.

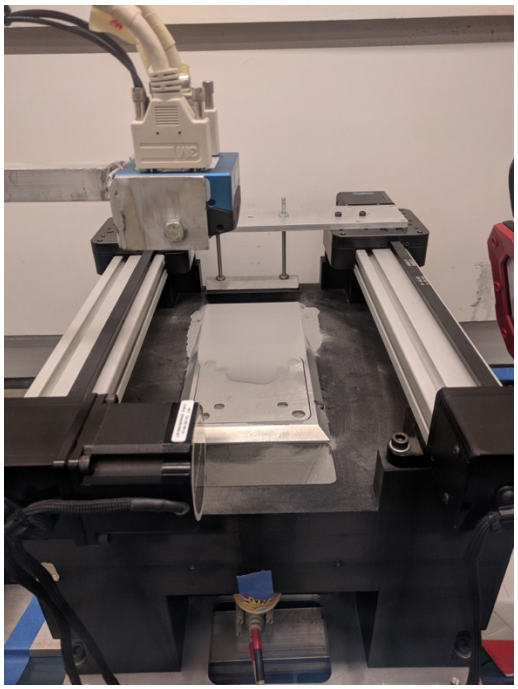

Figure 3-9. During the initial spreading process, the powder does not reach to the end of the build plate. The powder is built up until the plate is covered. Then layers are applied and imaged.

3.5.2 Sampling

This test consisted of sampling the build plate for regional particle size distribution. The build plate was built up with powder using a layer height of 30 microns at the speeds and dose rates specified in Table 3-1. A frame was placed over the build plate, and the build plate was lifted above the center insert. The inner grid was placed on top to separate the build plate into 9 regions for sampling.

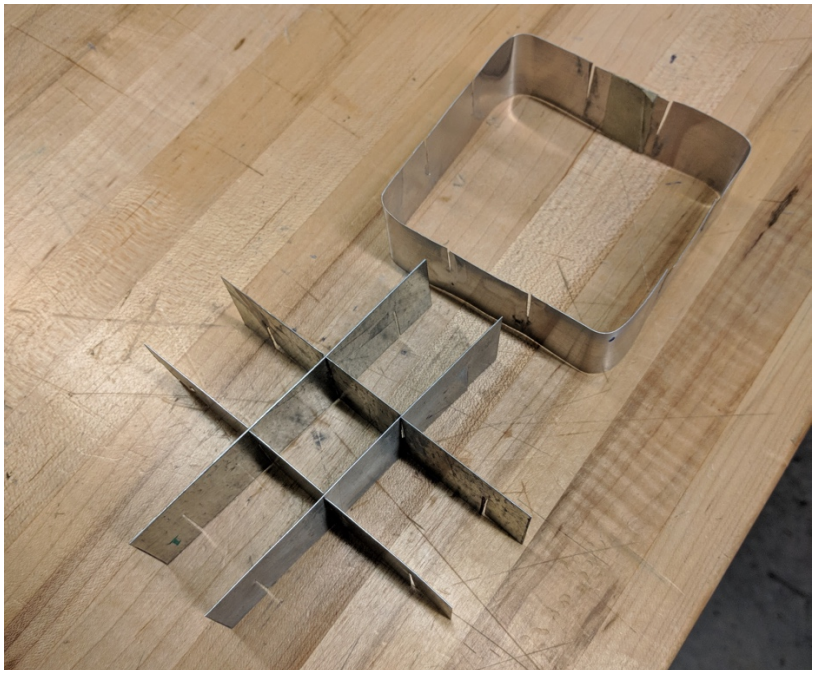

Figure 3-10. Components of the grid used to separate regions of powder. Consists of a frame that is placed around the build plate, and an inner grid that is placed after.

Figure 3-11. Sampling grid is placed onto the build plate.

Placing the grid will slightly disturb the powder, but mostly on the edge of the build plate. This process should not significantly affect the distribution in each region since the sheet metal was thin and most of the powder remained at the center of each region. The powder was then scooped out from each well and placed in a plastic tube. These samples were sent to Lawrence Livermore National Laboratory for particle size analysis.

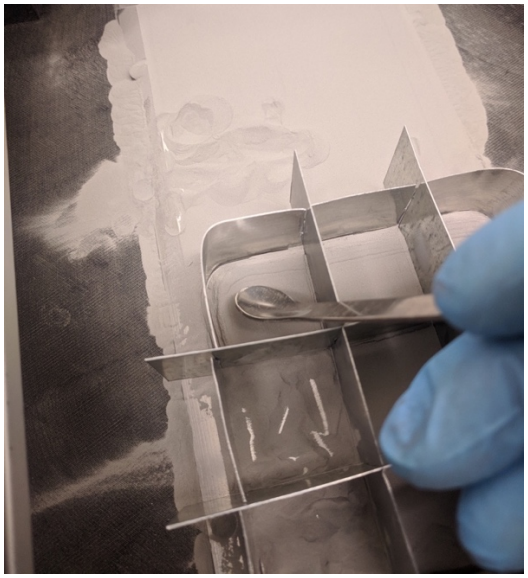

Figure 3-12. Powder is scooped for sampling in each of the nine regions.

4. IMAGE ANALYSIS AND EXPERIMENTAL RESULTS

The experiment described in 3.5.1 provided images for dose rates of 2, 3, or 4 times the layer height, each at 100 mm/s and 200 mm/s. For every run there were 4 layers, and 9 regional images for every layer. In total, there were 324 images to analyze. Each photo taken was roughly 1.4 cm by 1.4 cm. Individual particles could not be identified with the camera that was used, but aggregates or clusters of powder particles were easily visible. In order to analyze all of these images, a MATLAB code was devised to process the images in batches to save time. Image processing was necessary to correct contrast, color, format, scale, and sharpness. Each image was initially cropped down to the focused region, which made processing a lot faster due to the smaller file. The image was sharpened and then processed using the histogram contrast adjustments in MATLAB, but ultimately top and bottom hat filters were applied to adjust the contrast instead. Due to possible discontinuities in lighting across the image, local thresholding was used to binarize the image, but with further divisions, the local thresholding proved to be ineffective, and so global thresholding was used. The image was then morphologically closed by removing partial white areas around the border. To analyze the image, edge detection, boundary tracing, and area counting were methods approached for detecting aggregates.

Image processing is fairly subjective, with no right or wrong way or criteria. The process steps usually go in the order of image acquisition, preprocessing, enhancement, segmentation, and recognition, but can vary depending on the image being analyzed. There are many different methods and filters that can be used, but ultimately the operator determines what is best for the image and the extent of which the image should be manipulated. After the images had been processed, areas were delineated and separated to

extract characteristics and measurements. In this case, a method of determining how to quantify the surface quality or roughness was also needed for comparison of the regions on the powder bed. The brightness to darkness ratio proved to be a popular choice for evaluating the surface roughness of binary images, but looking at pixel area showed more promise in properly identifying the relative quality of surfaces.

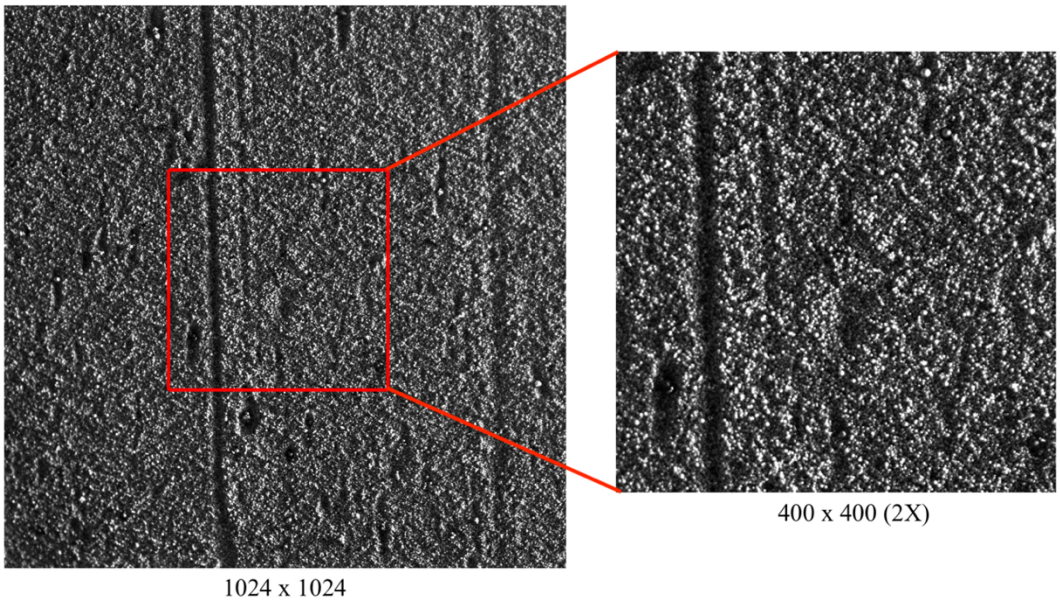

Figure 4-1. Image taken from a region of the powder bed. The image was cropped and scaled to the focused region of the image and then sharpened for analysis. A smaller image was used for efficiency.

4.1 Options for Image Processing

For image analysis, OpenCV, MATLAB, and ImageJ were all good options for processing images from the experiment. OpenCV with Python catered best to real-time imaging applications, which was not required for the experiment, and also had the steepest learning curve of the three choices. MATLAB and ImageJ were more efficient options that also had great image processing libraries. These programs would require less time to learn the tools needed for analysis.

ImageJ is an image processing program developed by the National Institutes of Health (NIH) that uses a GUI and provided a variety of Java plugins for customization. This program is commonly used to analyze microscope images and fulfills basic image processing needs. Though the program is easy to use, the majority of the functions cannot be edited. Filters and other changes applied could possibly over-edit images since the image processing tools lack detailed adjustments. ImageJ also appeared limited with basic built-in functions.

MATLAB contained similar functions to those of ImageJ with more control to the extent at which a process was applied. Because the lighting used was inconsistent across the powder bed, localized editing was necessary to look into, which would not be as easy in ImageJ. With MATLAB, each step could be monitored and evaluated for changes to the original. The documentation provided for the Image Processing Toolbox was ample, which would prove to be very useful. For more intense image processing, all three of these programs can be paired to work together, but for this analysis it is not necessary.

For building the MATLAB code for image processing, contrast enhancement and segmentation with edge detection and thresholding were explored to tune the image to the desired effect. A general outline of approach for the code can be seen in Fig.4-2.

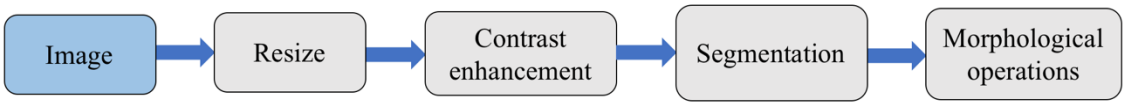

Figure 4-2. General outline for the MATLAB code for image processing.

4.2 Image Enhancement and Filtering

Nearly every function applicable to this project in the Image Processing Toolbox in MATLAB was tried and tested. Many of the functions were unsuccessful at transforming the image or made very little difference in preparing the image for segmentation. The following processes were the main ones that were focused on for improving the image.

The first step was to enhance the image for better contrast. In MATLAB, the contrast adjustment options were *imadjust, histeq, adapthisteq* [31]. Due to inadequate lighting, image values can be concentrated in a narrow range, which can make details indistinguishable. When the range is stretched to be wider through contrast stretching, features are accentuated, since the difference between adjacent pixel values become greater. The *imadjust* function mapped original values to new values such that 1% of the pixels were saturated at the highest and lowest intensities and the rest were linearly scaled to fill the range. The saturation limits could also have been modified so that a greater percentage was intensified. Comparing Fig 4-3 and Fig.4-4, *imadjust* did not show significant changes to the original image except for more saturation on the lower end of values, most likely due to the fact that the image filled out the grayscale range fairly well. The other method of contrast enhancement was *histeq*, or histogram equalization, which transforms image values so that the histogram is roughly flat and uniform. As seen in Fig. 4-5, histogram equalization seemed to reduce contrast, likely due to the fact that more pixels were on the higher intensity grayscale range. A similar function, *adapthisteq*, performs histogram equalization on local regions instead of global. The result of Fig. 4-6 was very similar to the *histeq* image, just with a more even histogram. The images that will see drastic change from these methods are those that have poor contrast, or whose grayscale

values are far from either limit. The experimental images were barely influenced by histogram contrast enhancements due to occupying the full grayscale range.

Fig. 4-3 to Fig. 4-6 show a trench that appears in quite a number of regions. When looking at the blade after the layer was spread, the trenches in the powder resulted from nicks on the blade or powder that adhered onto the blade. Also, large pits in the powder would occur if a clump of powder got dragged around on the powder bed.

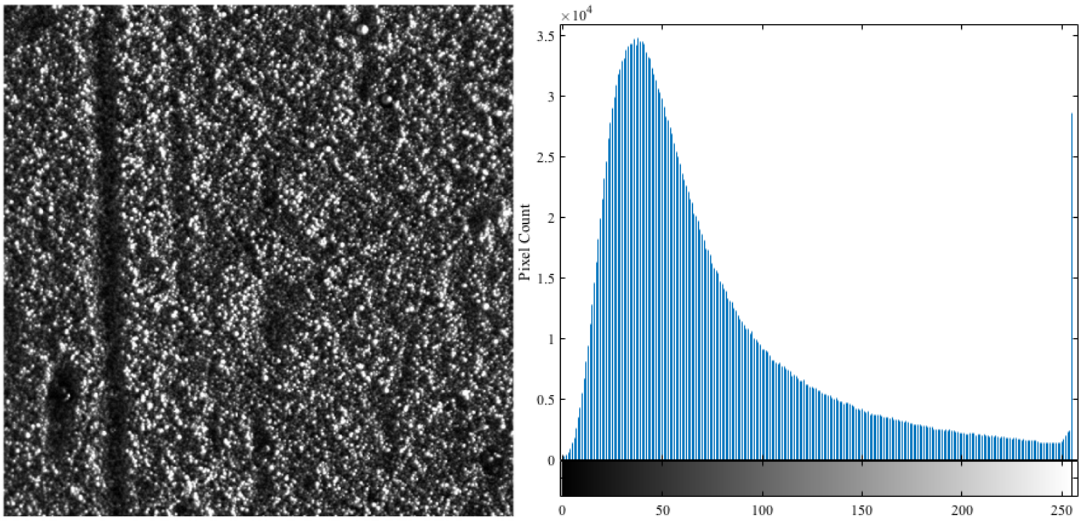

(a) (b)

Figure 4-3. (a) Original Image. (b) Corresponding grayscale histogram of the original image.

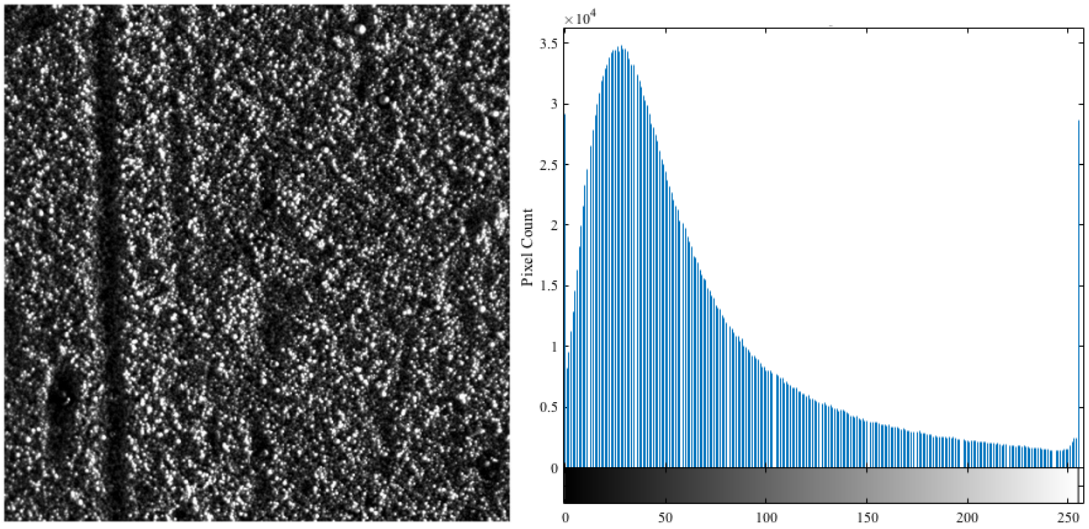

(a) (b)

Figure 4-4. (a) Image with contrast stretching applied using the *imadjust* function in MATLAB. (b) Corresponding *imadjust* histogram. The function showed little change compared to the original image.

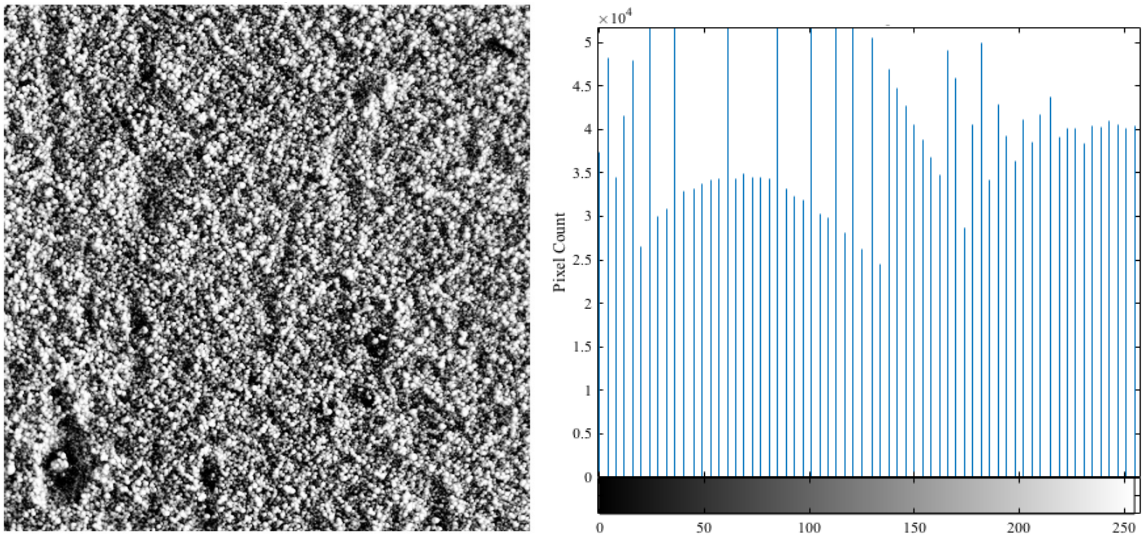

(a) (b)

Figure 4-5. (a) Image with histogram equalization applied using the *histeq* function in MATLAB. (b) Corresponding *histeq* histogram. The image is brighter with less detail when compared to the original.

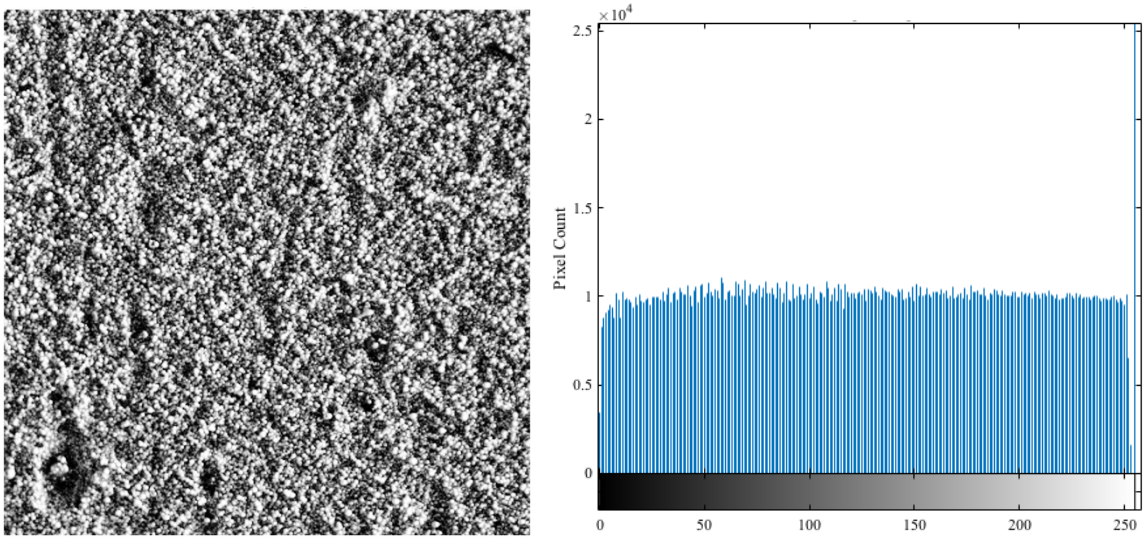

(a) (b)

Figure 4-6. (a) Contrast limited histogram equalization applied using the *adapthisteq* function in MATLAB. (b) Corresponding *adapthisteq* histogram. Similar to Fig. 4-5, the image produced lacks detail compared to the original.

Another method of contrast enhancement is filtering. By applying filters to an image, certain features can be removed or emphasized based on the resulting value of a pixel after an algorithm has been applied to the pixel's neighborhood. Filters work by applying a 2D filter matrix, or a kernel, to an 2D image. The sum of the products between the matrix and the image is calculated and that value is assigned to the center pixel that

aligns with the center of the matrix. Depending on the use of the filter, the filtered pixel value in comparison to the neighboring pixel determines the color.

Filters can be used to sharpen or blur an image, reduce noise, and in this case, improve contrast. The top-hat filter was used to accentuate the brighter areas by returning an image that contained objects of a certain size or smaller. The bottom hat was used to accentuate the dark objects as well. In order to achieve the final image in Fig. 4-8, the top-hat filtered image was added to the original, and the bottom-hat image was subtracted to emphasize each end of the intensities. This was the chosen method for contrast enhancement since it created clear separation between the background shadows and the aggregates, producing a stronger outline around each cluster.

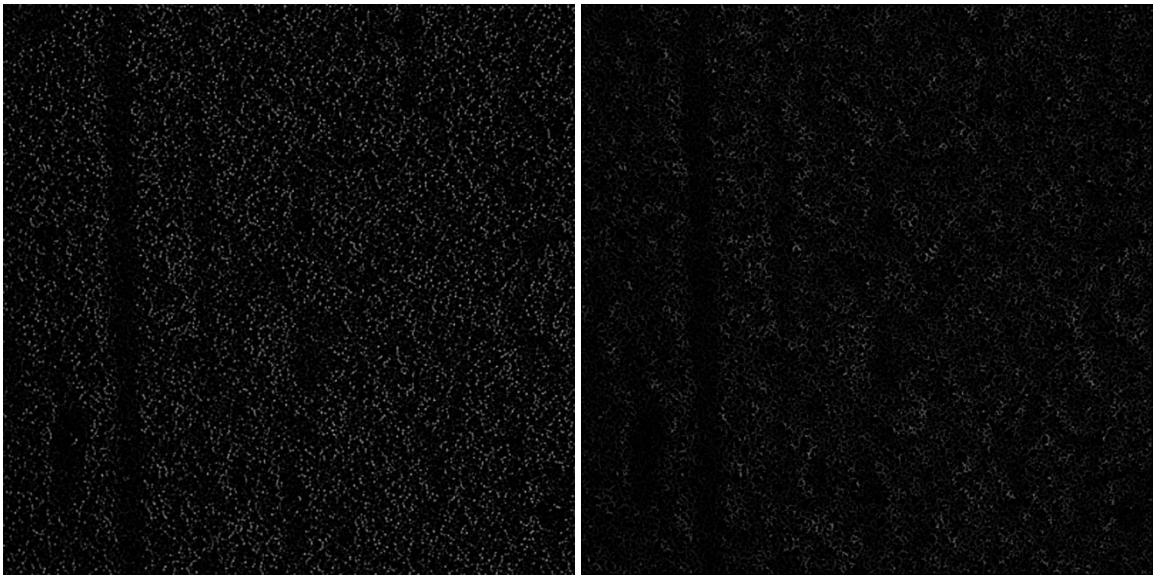

(a) (b)

Figure 4-7. Filtered original image using: (a) top hat filter with a structuring element of 5. (b) bottom hat filter with structuring element of 5.

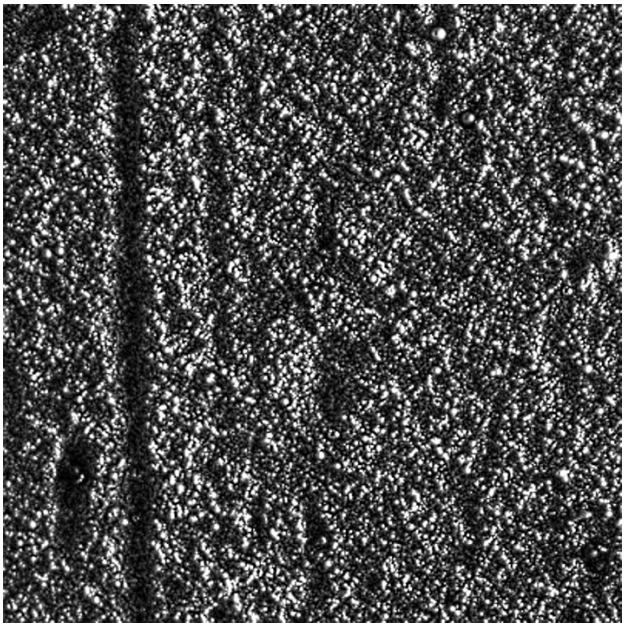

Figure 4-8. Original image with the top hat filter results added and the bottom hat filter results removed. Clusters are better defined with this method.

4.3 Image Segmentation

After an image has been enhanced, the next step is to try to isolate the objects in the image so that the objects can be counted and measured. Segmentation involves simplifying the image from grayscale to binary, which will subdivide the image into regions that correlate to an object or a feature. Typically, in a binary image, the foreground object desired is white and the background is black. The three methods of segmentation explored were edge detection, local thresholding, and global thresholding. Each of these three methods use different techniques to isolate the objects of the image.

4.3.1 Edge Detection

Initially, edge detection was a method considered for identifying and segregating the aggregate features of the powder. Aggregates were looked at instead of each particle because the camera could not capture to the necessary resolution for individual particles. Edge detecting works by finding where the image brightness changes drastically from

neighboring objects. In order to find these edges, a derivative detects locations of large shifts in intensity. Two common algorithms used to detect edges are the Canny method and the Sobel Method [32]. Both methods determine the gradients of the image and defines an edge where the gradient is a maximum, but the approach of each method is different.

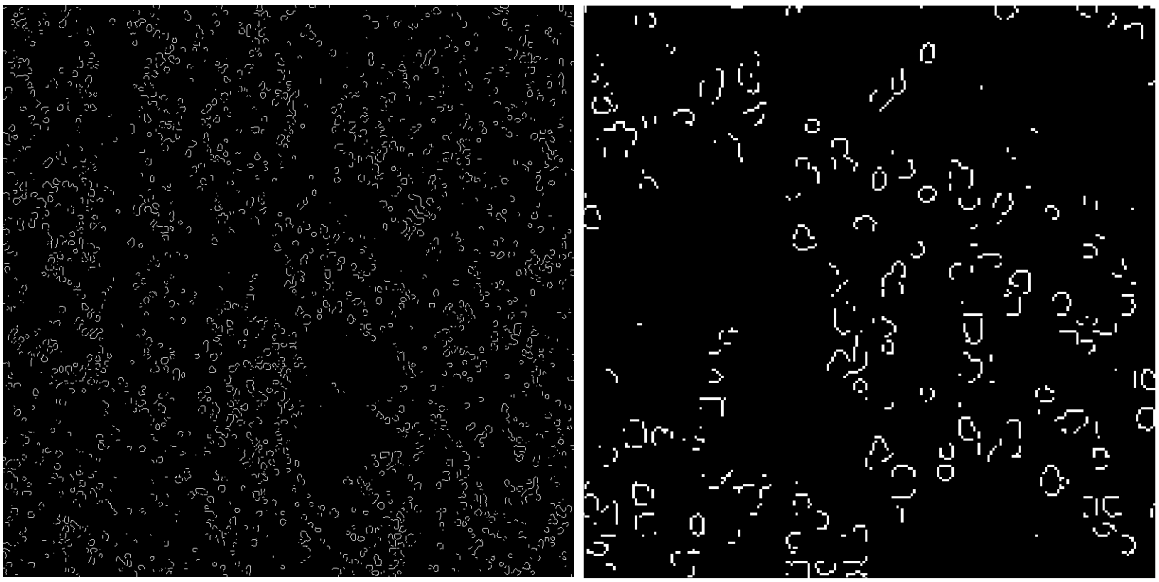

(a) (b)

Figure 4-9. (a) Sobel filter used for edge detection on the original image. (b) Close up, the edges are not closed regions.

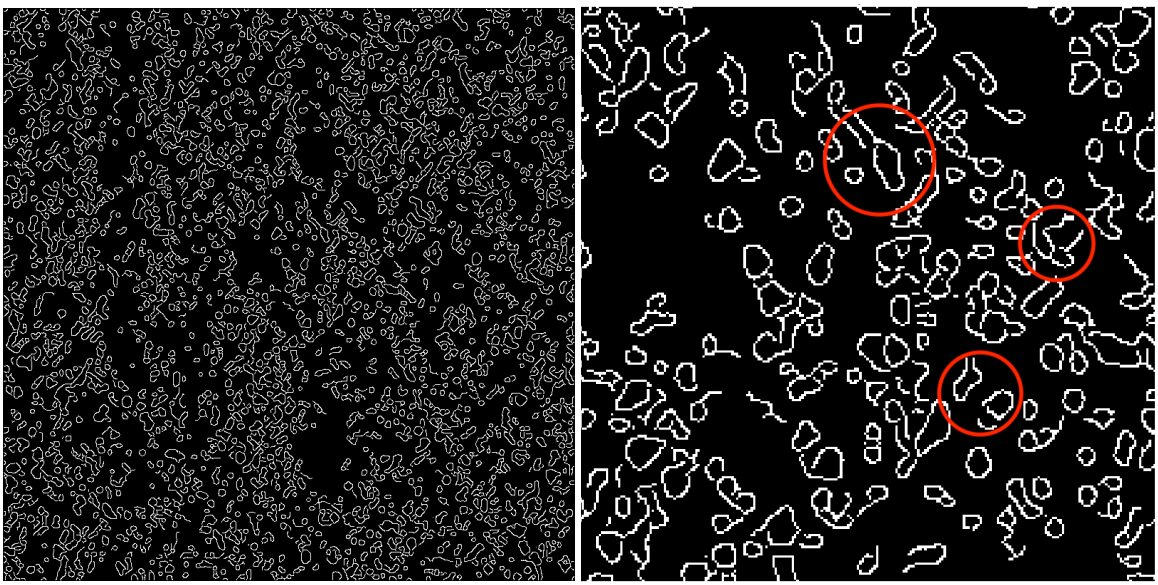

(a) (b)

Figure 4-10. (a) Canny filter used for edge detection on the original image. (b) Close up view; the edges using the canny filter are not closed either.

The issue with using edge detection was that the edges were not closed regions, and so individual clusters could not be identified, making the analysis process in the future difficult. Edge linking functions created by P. Kovesi [33] were also tested, but the algorithms could not close the object edges, so this idea was discarded.

4.3.2 Thresholding

The simplest and easiest method of segmentation is thresholding. Thresholding creates light and dark regions by replacing pixels below a specified threshold intensity value with a 0, creating a white foreground. All pixels above the threshold value are replaced with a 1, creating a black background. Determining the threshold is the difficult because objects can be lost or poorly interpreted if the wrong threshold value is chosen. Since image processing is subjective, the only way to determine a good threshold is by visual assessment.

Usually, a single global threshold value is found by averaging intensities, and then the pixels are adjusted according to that value. In this particular case, since in the experiment the LED light was on the side and not above the powder spreader, the powder bed was possibly illuminated unevenly, and so a global threshold value might create more white pixels on one side than the other. In order to adjust for local intensities, an algorithm similar to the one used by Gontard et al. [34] was implemented to divide the image into subdivisions and to threshold each subdivision locally. The MATLAB code in Appendix C produced the following results in Fig. 4-11 with varying subdivisions. To determine the optimal threshold to divide the classes of pixels, the function *graythresh* was used, which uses Otsu's Method to minimize the "within-class variance" of foreground and background pixels, which is the sum of the two variances multiplied by their weight [35].

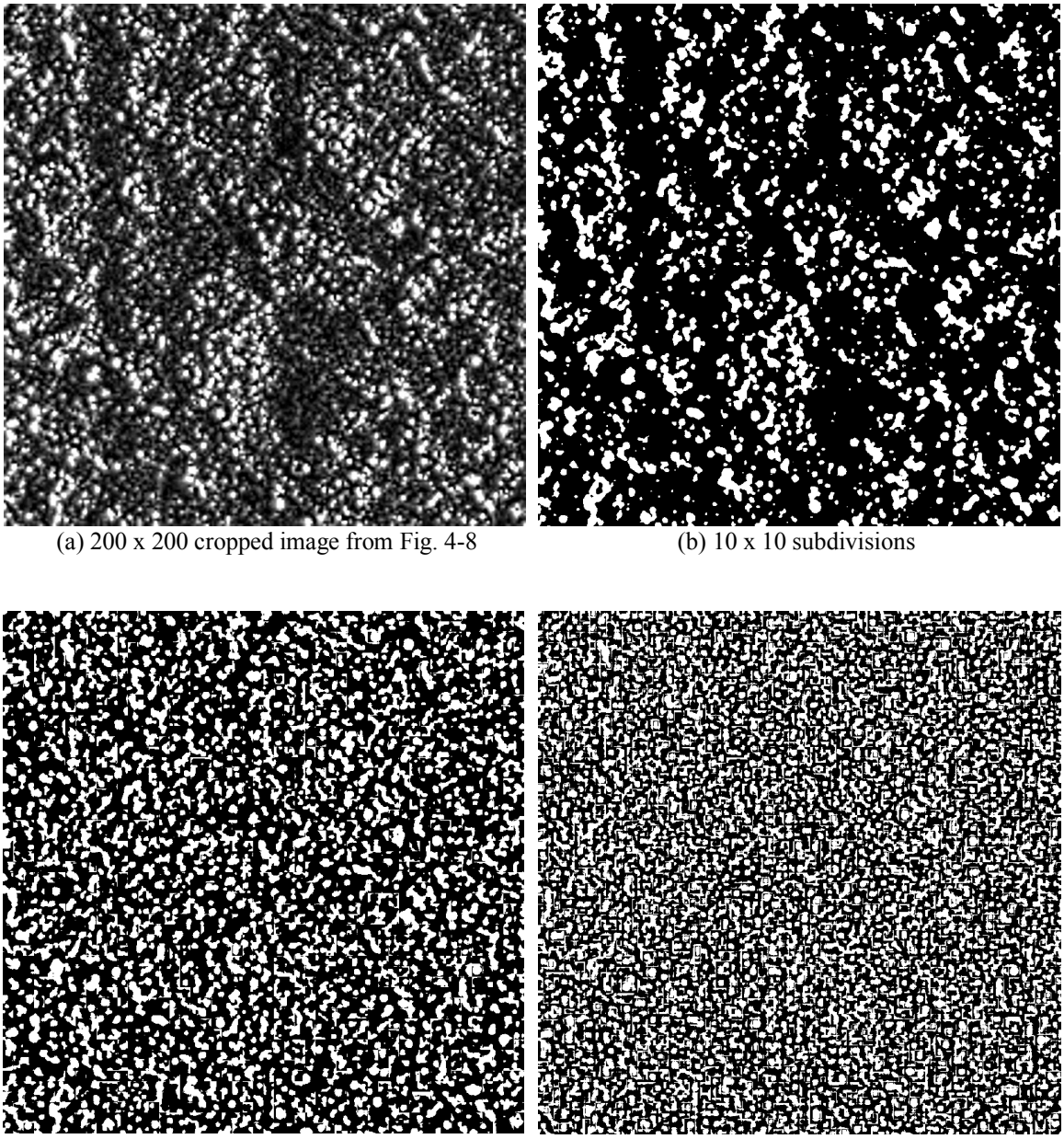

(a) 200 x 200 cropped image from Fig. 4-8 (b) 10 x 10 subdivisions

(c) 50 x 50 subdivisions (d) 100 x 100 subdivisions

Figure 4-11. Image with local thresholding applied at each of the m x m subdivisions.

Based on the results of Gontard et al. [36], with gradually increasing subdivisions, more particles should be detected correctly, but Fig. 4-11 did not reflect that. Past a certain division number, the edges of the subdivisions were identified as objects below the threshold, oversaturating the image with objects that were not present in the original image. Instead, global thresholding was revisited, and the result in Fig. 4-12 appeared similar to

the result of localized thresholding of Fig. 4-11b. After global thresholding, the *bwareaopen* function was used to remove small objects. A morphological close was performed to smooth out objects in the image, and then a fill was performed to close up small background spots that may be surrounded by foreground pixels.

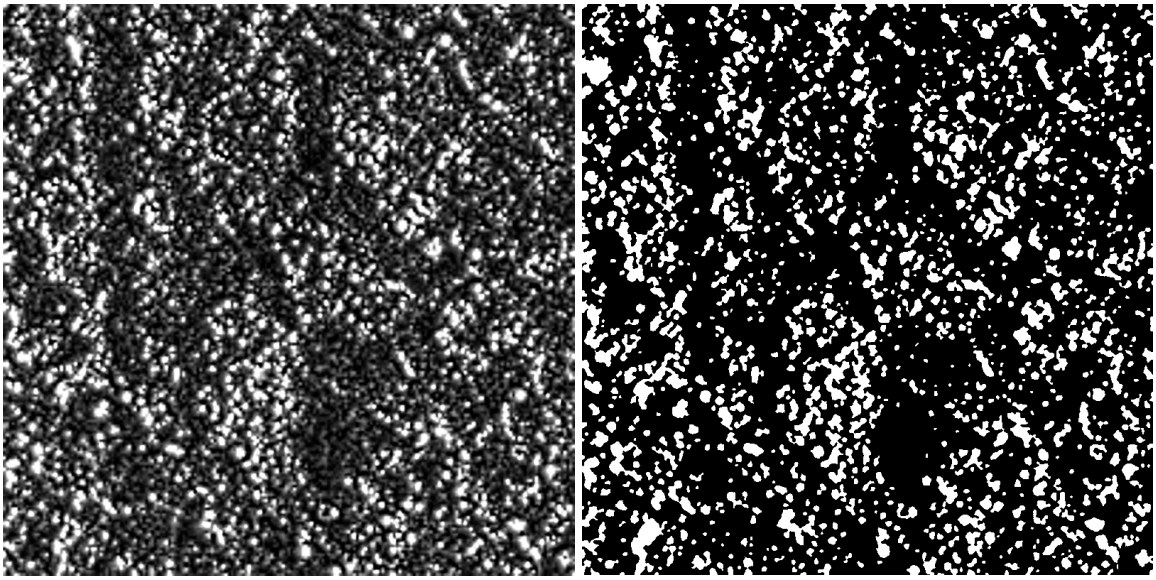

(a) (b)

Figure 4-12. (a) 200 x 200 cropped original image. (b) Final image after global thresholding, removing small objects, smoothing out objects, and filling in holes.

4.4 Image Analysis

After the images were processed according to Fig. 4-13, the next step was to figure out how to quantify characteristics of the region from the image. Since density and particle distribution could not be easily identified using these images, the best characteristic to extract from these images was surface quality or surface roughness. The images taken from the experiment did not have a value for depth or height of the powder which makes defining surface roughness difficult, but a few researchers have looked into relating binary images to surface roughness [6, 36, 37]. As mentioned in Section 2.2, Kayahan et al. [18] used binary speckle imaging to determine the surface roughness of a metal surface. While the optics and imaging instruments used in this experiment were different than in [18], the

same principles for analysis were tried. After they converted their images to binary, they counted the number of bright pixels (B) and dark pixels (D) and defined a dimensionless ratio B/D for each image. From their results, lower B/D ratios corresponded with a coarser surface roughness. This method was looked at for defining the surface quality of the powder bed.

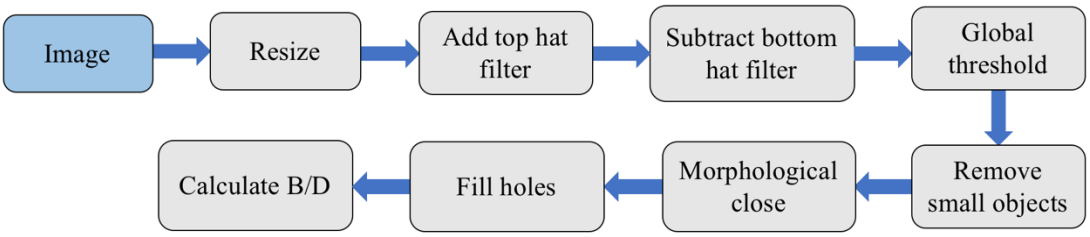

Figure 4-13. Finalized method for image processing.

4.4.1 Sandpaper Comparison

For comparison, samples of sandpaper at different grits were placed on the build plate and captured. Sandpaper has irregular and faceted abrasive grains glued to a backing, which made them a good reference to spherical particles on the surface of the powder bed. Grit value is defined to be the mesh size used to sort the grains rather than the grain size. A grit value of 100 means that the majority of the grains were able to be filtered through a mesh with 100 divisions per inch, and so the particles are not guaranteed to be a consistent size. Below are the grit values of the aluminum oxide sandpaper tested as well as the corresponding B/D ratio calculated from the processed images. All of the sandpaper used were from the same manufacturer. The B/D values in Table 4-1 and Fig. 4-15 were sampled from 4 areas of each image and then averaged.

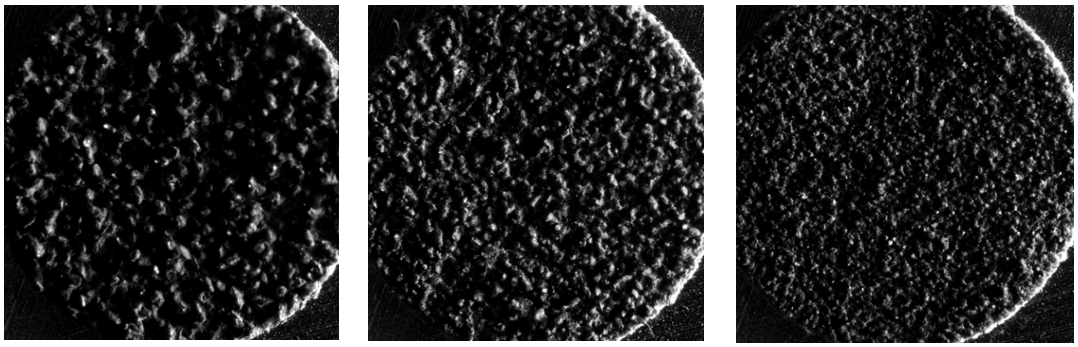

(a) 50 Grit (b) 80 Grit (c) 100 Grit

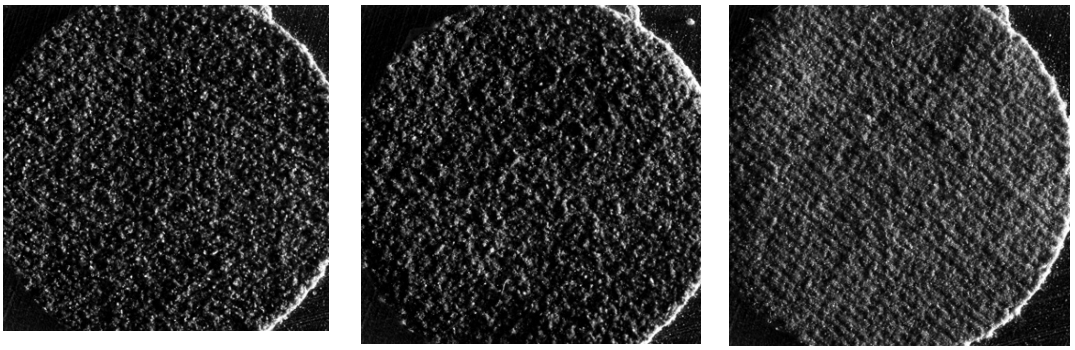

(d) 150 Grit (e) 180 Grit (f) 320 Grit

Figure 4-14. Grayscale images of some of the sandpaper samples used for the experiment. The samples were all from the same manufacturer but were not all the same shade of gray.

Table 4-1. Average B/D values of sandpaper samples tested at 4 different locations.

Grit	Average B/D	Std. Dev.
50	0.131	0.004
60	0.187	0.008
80	0.179	0.004
100	0.137	0.004
120	0.220	0.005
150	0.166	0.003
180	0.188	0.008
240	0.176	0.003
320	0.257	0.008

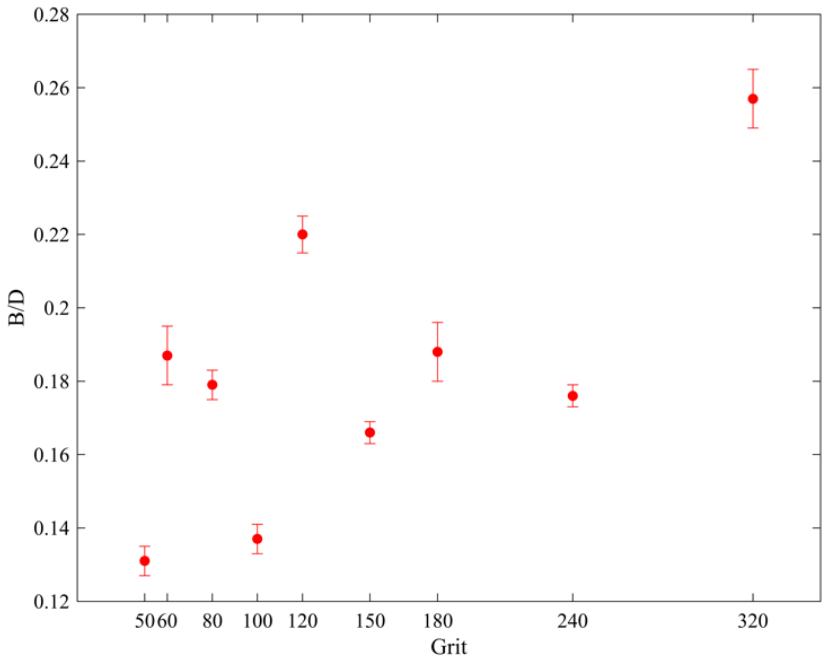

Figure 4-15. Average B/D values for various grit values of sandpaper with standard deviation.

In Fig. 4-15, a trend towards higher B/D ratios at higher grit values was expected, especially if the results made in [18] were still valid for this experiment. Generally, when looking at the graph as a whole, the values do trend upwards, but not consistently. While there were some discrepancies, the 320 grit value did exhibit the greatest B/D ratio, and the roughest grit had the lowest B/D ratio. The 120 grit sandpaper displayed an unusually high B/D ratio compared to the neighboring values, and the 100 grit B/D value was unexpectedly low. Despite the inconsistencies with the average B/D values across the sandpaper samples, the standard deviation for each grit value appeared relatively small, which would indicate that each B/D is consistent for a particular surface roughness. It is also important to note the scale of the values. The range of B/D values from 50 to 320 grit are 0.131 to 0.257, which is quite a small range for such significant differences in grain size of the sandpaper.

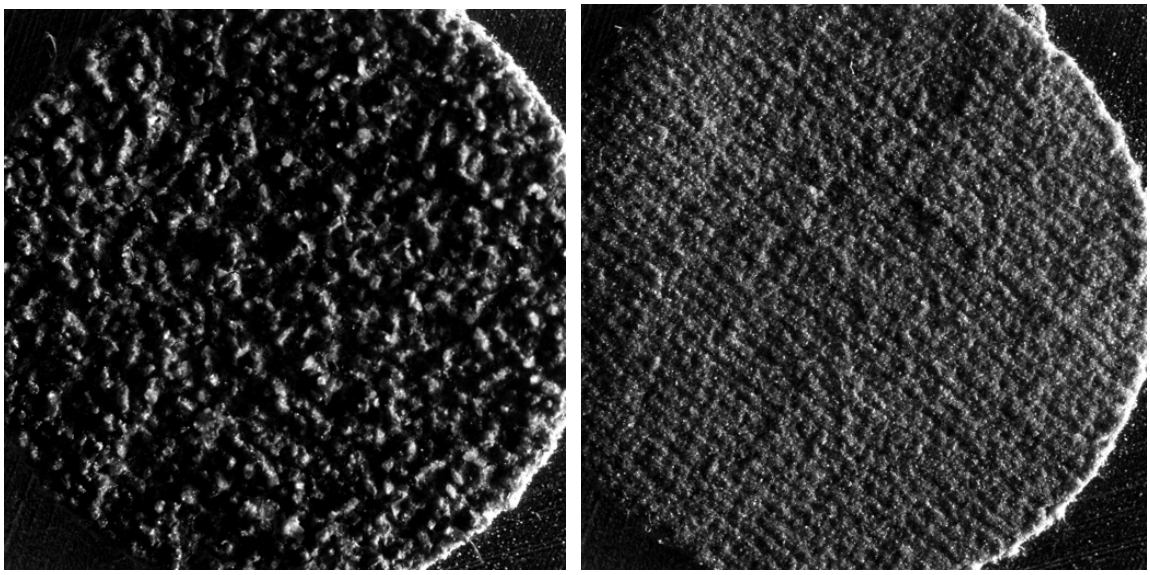

Figure 4-16. 80 and 320 grit sandpaper. The 320 grit sandpaper was significantly lighter in color which was reflected in the grayscale image.

Each sandpaper sample was a different shade of gray, which might have contributed to why the results were not as expected, since light could have reflected more or less than the others. For example, looking at Fig. 4-16, the 320 grit is much lighter in color than the 80 grit, and the grains look very different as well. The grains used on the sandpaper were also visibly faceted for the coarser grits, which reflected light on one side of the grain if highlighted by the floodlight. Looking at the 320 grit sandpaper, the adhesive might contribute to the particles being less apparent as well.

Doing this experiment with the sandpaper also exposed a flaw in using B/D as a method of analysis. What the B/D ratio did not indicate, in relation to surface roughness, was the size of the abrasive grains. As seen in Fig. 4-17a and b, the images clearly show that the 60 grit appears rougher than the 100 grit since the grains are significantly larger in size. The objects in the binary image for the 60 grit are larger than those in the 100 grit as well. This B/D value does not account for size of objects, just the total white and black

areas, and so that important characteristic of size that does play a huge factor in surface roughness was lost.

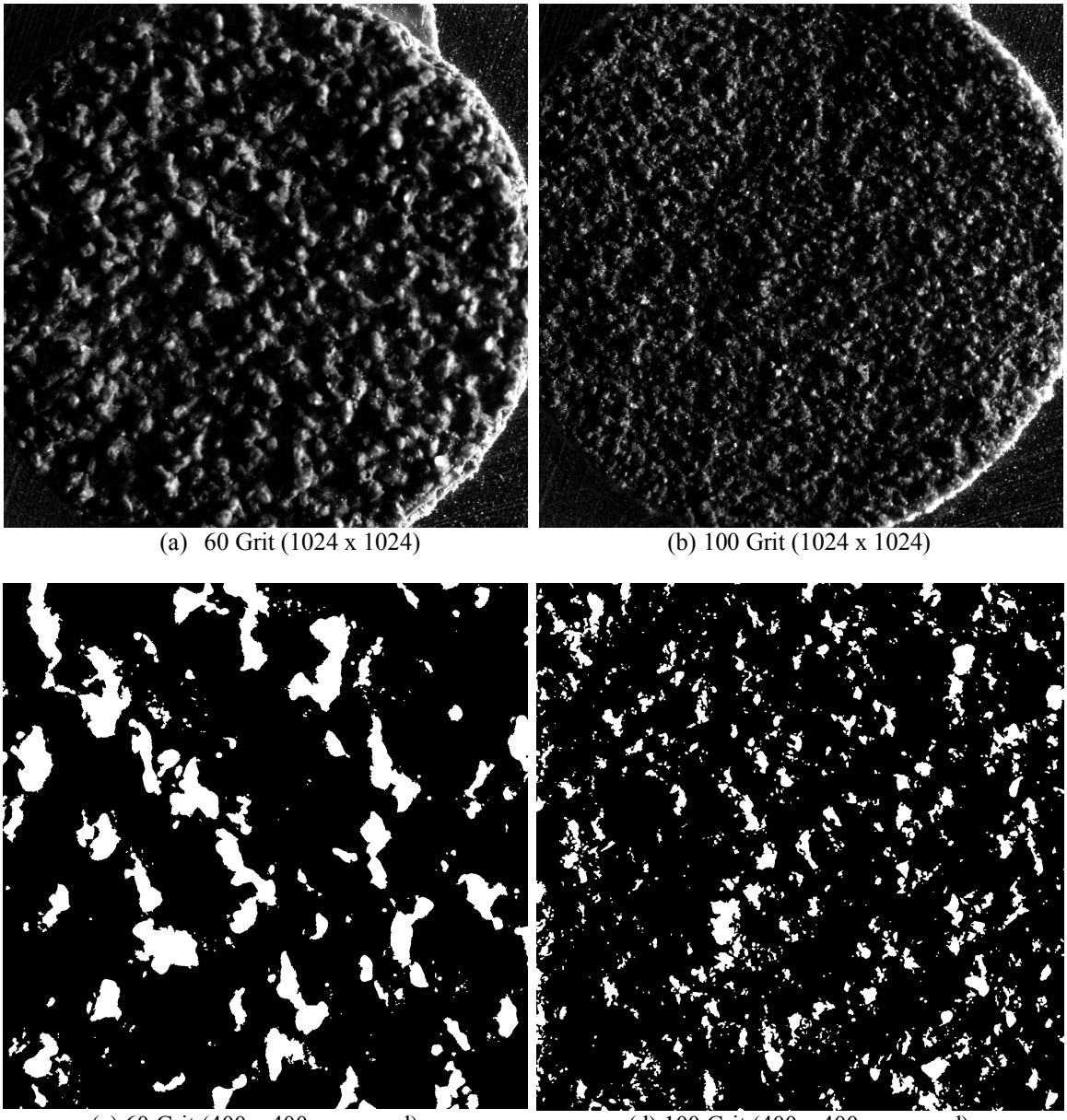

(a) 60 Grit (1024 x 1024) (b) 100 Grit (1024 x 1024)

(c) 60 Grit (400 x 400 processed) (d) 100 Grit (400 x 400 processed)

Figure 4-17. Sandpaper images used for reference at 60 and 100 grit with corresponding processed binary images.

Since using the B/D ratio did not fully demonstrate the surface quality of the various sandpaper samples, pixel area means and standard deviations were looked at. Pixel area is the pixel count of a closed white object surrounded by background pixels. Objects in

coarser grit images (Fig 4-17c) have a higher pixel count due to the larger size, whereas finer grit images (Fig. 4-17d) have objects that are a lot smaller. This would cause the pixel area average and standard deviation of the coarser grits to be much higher. The standard deviation of the pixel areas in an image would provide a good idea of the spread of the data, indicating how rough or uneven the powder surface was qualitatively. Only the upper half of the standard deviation was plotted in Fig. 4-18, since that would indicate the presence large outliers.

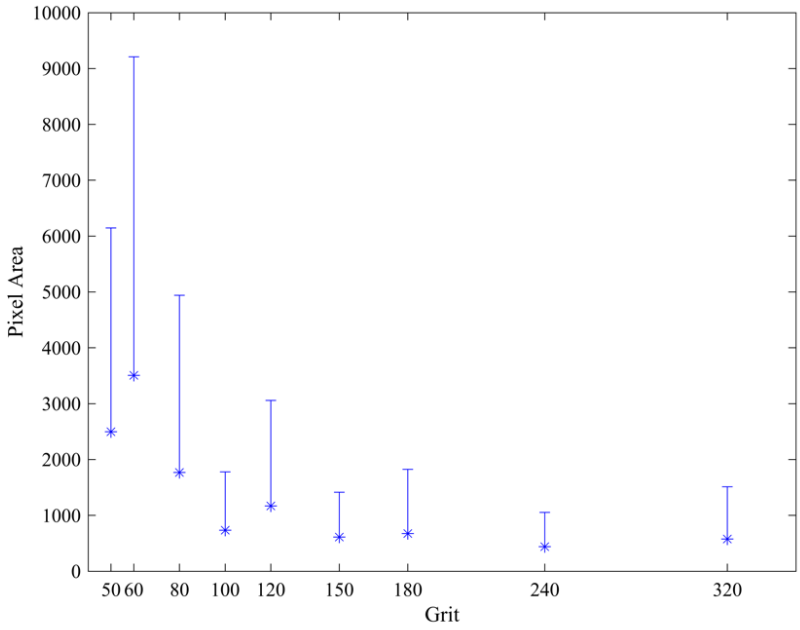

Figure 4-18. Pixel area averages and standard deviation to demonstrate spread for various grit values.

While finding B/D ratio still showed promise and was explored for analyzing the experimental data, finding the mean of the pixel areas as well as the standard deviations followed an expected trend closer than using B/D. In Fig. 4-18, the coarser grits showed a higher pixel area average as well as a larger spread, and the finer grits had a lower average and a smaller variance, which would indicate a smoother surface. In Fig. 4-15, the B/D value of 60 grit was higher compared to 100 grit, but when using pixel area, 100 grit had a

smaller pixel area mean and standard deviation, which was more in line with expectations. Though the 120 grit pixel area mean was higher than the 100 grit, it was not larger in mean or standard deviation compared to the 80 grit, which was not the case when using the B/D values. This method does rely on personal analysis to judge relative surface quality rather than assigning a number to indicate the surface roughness as with the B/D method. If there was a region with a high pixel area mean, it could have a similar surface roughness as a region with a smaller pixel area mean but with a much larger standard deviation. This method, like the B/D method, did not show every grit with the expected values according to the trend, but using the pixel area provided better insight about the size of the objects in each image.

The sandpaper samples were also tested under a profilometer to get an idea of what surface roughness value a B/D value would possibly correspond to in order to give a relative quantitative answer. If more time were available, more profilometer runs would have been taken for each grit value and then averaged to get an idea of the range of surface roughness values applicable. Values from Table 4-2 showed predicted results with finer grits demonstrating a smaller surface roughness value.

Table 4-2. Sandpaper surface roughness values measured using an AMBiOS XP-1 profilometer.

Grit Value [-]	Ra [μm]	RMS [μm]	Range [μm]
100	39.7	47.3	185
150	26.1	32.9	165
180	20.9	26.4	160
320	11.1	13.8	77

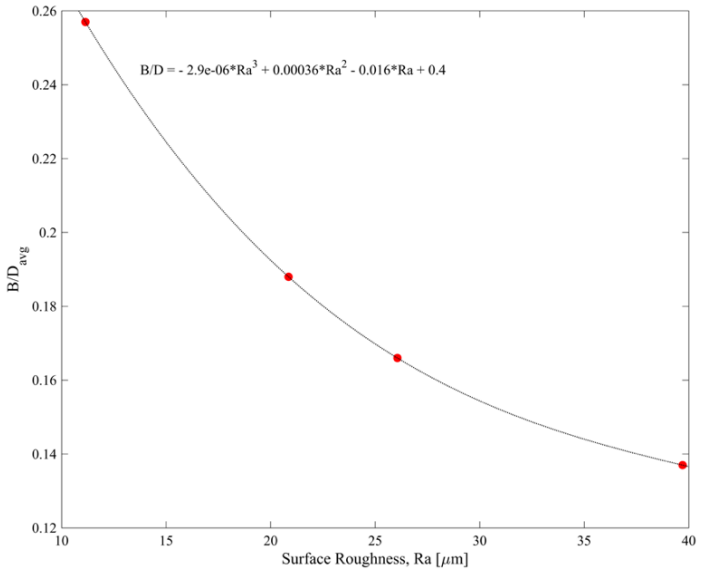

Figure 4-19. B/D ratios from Fig. 4-15 plotted against corresponding profilometer Ra calculations.

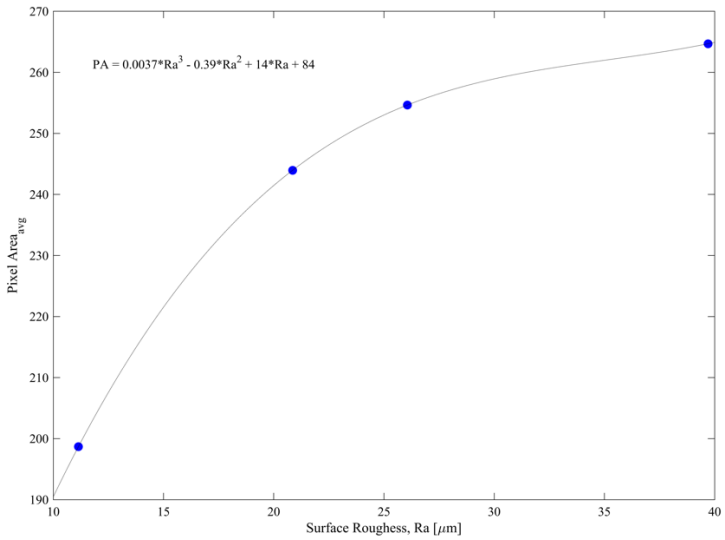

Figure 4-20. Pixel area mean from Fig. 4-18 plotted against corresponding profilometer Ra calculations.

From the profilometer data in Fig. 4-19, the B/D and surface roughness varies inversely. The curve profile was generated as a polynomial based on the results from [18,37] and while there was a clear trend when plotting B/D ratios against the profilometer data, more data points were needed to confidently confirm the fit, especially when looking at Fig. 4-15. Also, after discovering that a higher B/D ratio does not necessarily indicate

that a surface was smoother, the profilometer data proved to not be useful as a reference for this analysis. When plotting the Ra values against the corresponding pixel area means in Fig. 4-20, the surface roughness increased with increasing pixel area mean. Again, more points are needed to verify the curve fit, but since higher pixel area mean does correlate to a rougher grit or a rougher surface, there is potential to use this data in the future.

Out of curiosity, powder was also adhered to double-sided adhesive so that the sample could be imaged and also tested with the profilometer. This gave another idea of how the image processing results might correlate to the surface roughness data from a profilometer. The cavities in Fig. 4-21 were characteristic of the tape and were not formed by the powder. The sample was put through the image processing method from Section 4.3 and the results are noted in Table 4-3. After the sample was tested with the profilometer, it was checked under a microscope to see if any trenches had been created from the stylus dragging on the surface and none were seen.

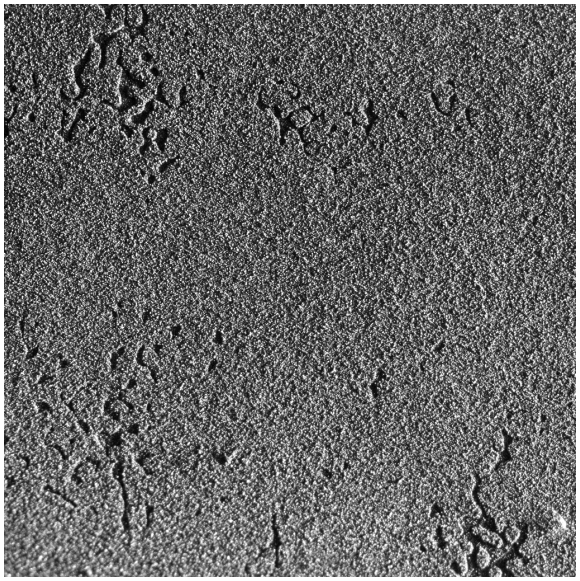

Figure 4-21. Powder adhered onto double sided tape that was used with a profilometer.

Table 4-3. Image processing measures taken from Fig. 4-20.

Measure	Value
B/D	0.47
Pixel Area Mean	128
Pixel Area SD	183

Table 4-4. Profilometer results from testing Fig. 4-20 with several passes.

Run [-]	Ra [μm]	RMS [μm]	Range [μm]
1	6.2	7.6	42.4
2	5.9	8.0	32.4
3	7.8	9.4	40.9
4	10.3	12.8	61.9
5	10.4	12.9	48.2
6	4.9	7.3	41.6
Average	7.6	9.7	44.6

Though this was only one sample, the values from the profilometer provided an idea of how even the powder surface of Fig. 4-20 was in relation to the pixel area mean and standard deviation calculated, which was a good reference point for the powder bed images. The high B/D value from Table 4-3 also indicated that the region was smooth as well. Based on the data from Table 4-4, an image of powder with a pixel area mean of roughly 130 can range from 5-10 microns in surface roughness.

4.4.2 Experimental Results

The conditions for each run of this experiment are listed in Table 3-1. Each run consisted of 4 layers and 9 regions, so in total there are 36 images for every run. For each image in the set, the B/D ratio was calculated. The four B/D ratios for each region were then averaged. In Fig. 4-22, the B/D mean and standard deviation of each region are plotted for the second run of a dose rate of 2 and a speed of 100 mm/s as an example. Plots for all runs can be seen in Appendix D.

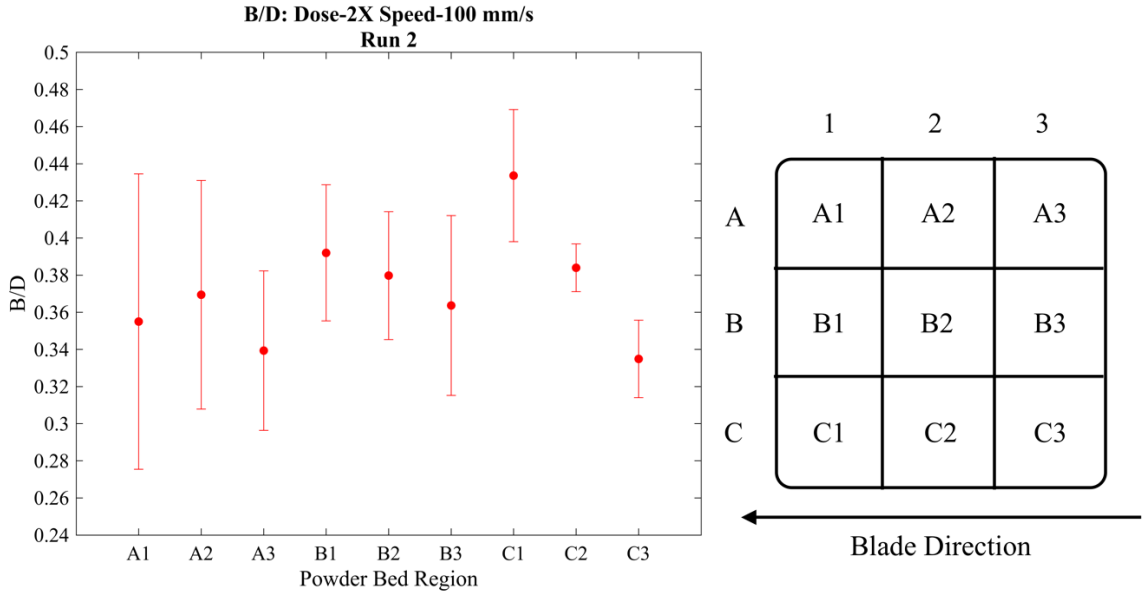

Figure 4-22. B/D mean and standard deviation for each region of the powder bed for a dose rate of 2 at a speed of 100 mm/s. Regions defined in diagram on the right.

All the B/D plots of each run showed no obvious pattern across regions when the graphs were compared. In all the runs, the regions that were the roughest were not always the case. Standard deviation was also not consistent regionally when comparing different plots. The worst max standard deviation was around 0.08, which was roughly 20% of the corresponding mean. For the majority of the regions, the standard deviation was smaller (0.01 – 0.05), and so the mean represented the spread of the data well enough for further analysis. The B/D values for the powder were much higher than the values for the sandpaper, indicating that the powder surface roughness was likely smoother and more even than the 320 grit sandpaper, in which Ra equaled roughly 16 microns from the profilometer data.

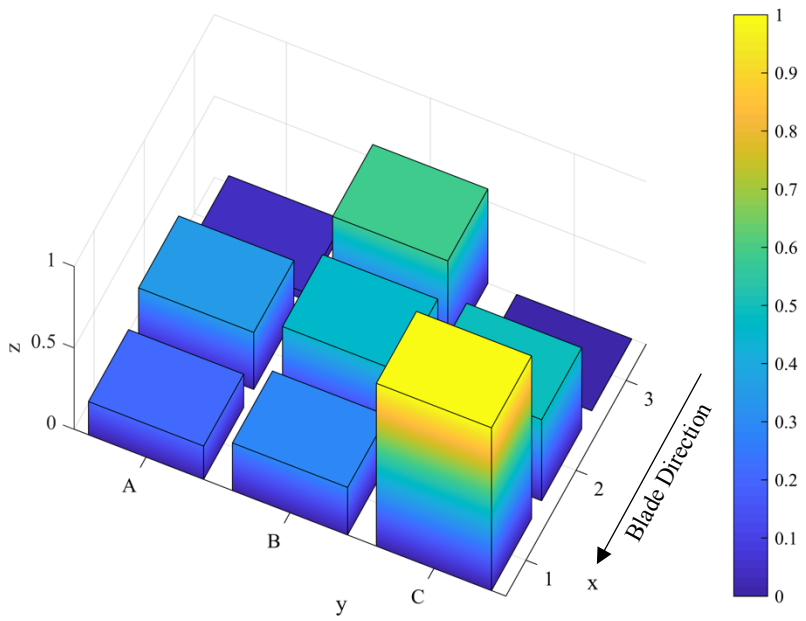

Figure 4-23. Normalized B/D values demonstrating roughness of each region for a dose of 2X at 100 mm/s, run 2 of 2.

For each run, the average B/D ratio was used to create the visual in Fig. 4-23, which allowed for quick determination of the smoothest region in the powder bed. Since there was not a fully determined method to convert B/D to roughness values, the values for the bar plot have been normalized. 3D bar plots were also created for the other runs and can be seen in Appendix D. This method revealed that the lowest B/D values for this particular run was column A on the y-axis, and C3. Symmetry would be expected between columns A and C, which might indicate there was a difference in blade heights on each end.

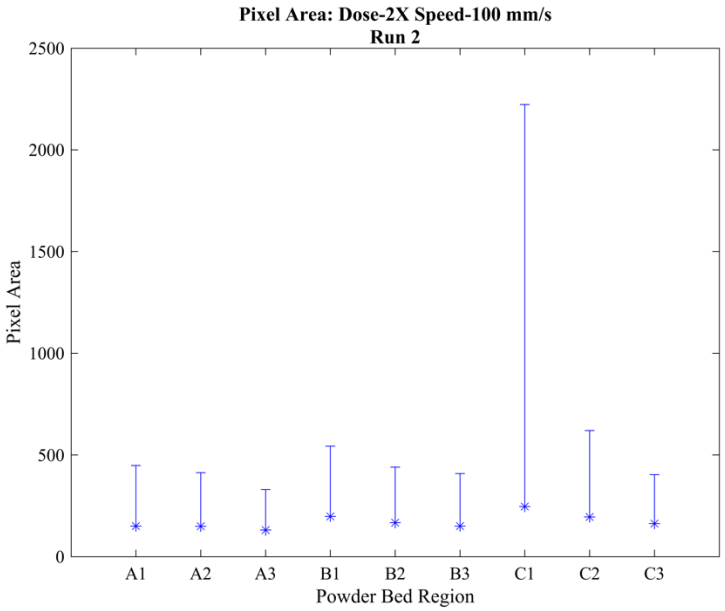

Figure 4-24. Object pixel area mean and standard deviation for a dose rate of 2 and a speed of 100 mm/s.

Since the results of the B/D test for the sandpaper were not completely reliable, for each run the pixel area mean and standard deviation was calculated for each region. Pixel area mean and standard deviation for a dose rate of 2x and a speed of 100 mm/s is shown in Fig. 4-24 as an example, and the graphs for the other runs can be seen in Appendix D. When the B/D ratio and pixel area results were compared, the means followed the same shape across the regions. Also, the greater pixel area means have a greater standard deviation, even though the difference between the means were subtle when considering the range of values. If a high B/D ratio equals a lower surface roughness was assumed, Fig. 4-22 shows that region C1 should be the smoothest, but the corresponding pixel area plot in Fig. 4-24 shows that the region has a large spread of values, which indicates the opposite. This means that a higher B/D ratio was a result of bigger patches of white pixels, similar to the effect of the lower grits of sandpaper. Since the B/D means and pixel area means tend to follow the same pattern, that means that a higher B/D ratio was influenced by larger patches of white.

Correlating the B/D value to a specific surface finish quantity was not possible, but quality can still be evaluated if additional information about the pixel areas were provided. The combination of these two graphs could determine the relative quality of the surface. Because the pixel area spread was quite large compared to the pixel area mean, the mean was not a great representative of the distribution, but still gave good insight into how the data leaned. Compared to the majority of the standard deviations, region C1 appeared quite abnormal for this particular run, and referring back to the original image helped to understand why. In region C1, the powder was not fully spread across the region, which caused a large white area where there was a step in the powder. Using pixel area values was able to detect whether one region had better surface quality than another.

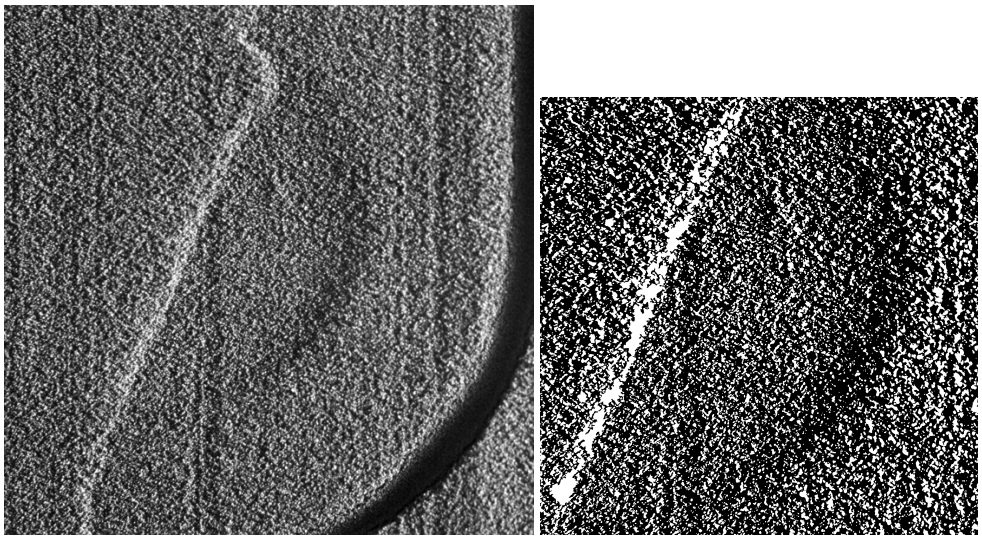

Figure 4-25. Image of region C1 from one of the layers at a dose of 2x and speed of 100 mm/s. The powder did not fully spread across, creating the brighter ridge that would be identified as a large white spot when binarized.

4.4.2.1 Repeated Runs

Each dose rate of 2x, 3x, and 4x was tested twice at 100 mm/s for comparison. The pixel area mean and standard deviation of each region for each run are plotted on the following graphs.

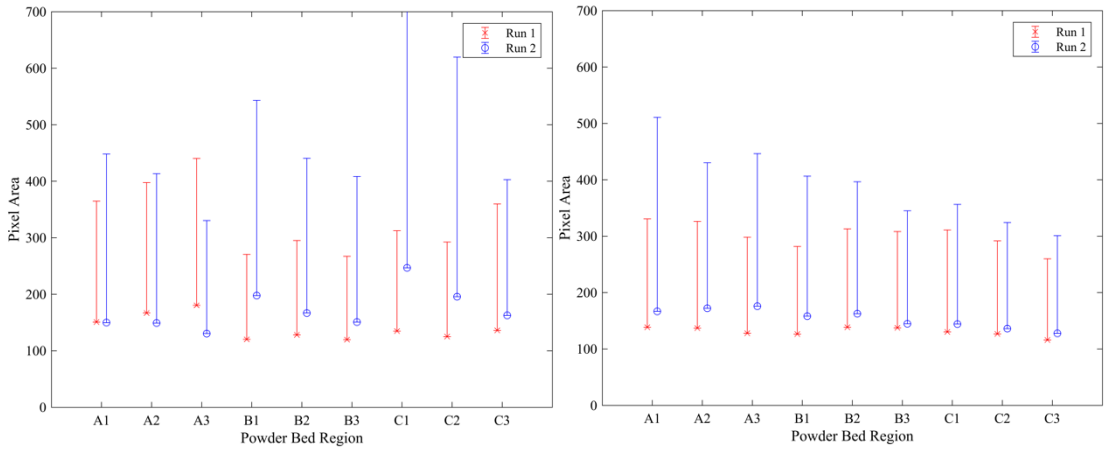

(a) Dose: 2X, Speed: 100 mm/s

(b) Dose: 3X, Speed: 100 mm/s

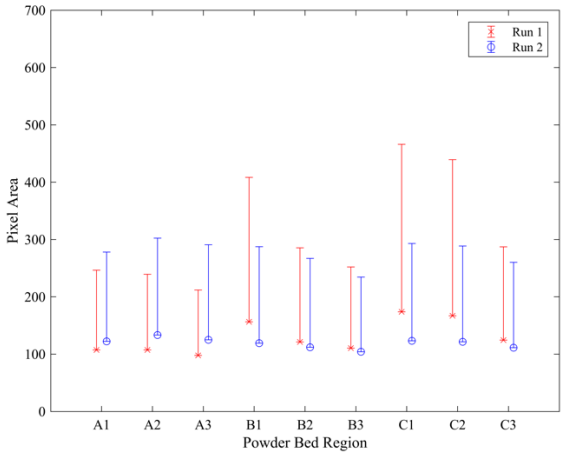

(c) Dose: 4X, Speed: 100 mm/s

Figure 4-26. Comparing B/D values in repeated runs. While dose varied, speed was kept at 100 mm/s.

When comparing the two runs for each dose rate at 100 mm/s, the pixel area values from the first run did not match the second nor did they show similar regional patterns. Looking at Fig. 4-26a, regions B1-3 and C1-3 varied drastically between the two runs, with the second run having a much greater spread. The range of pixel area means and standard deviations for the 4x dose rate were smaller than that of 2x and 3x. The difference between the pixel area means and standard deviations for the repeated runs at 3x and 4x dose rates were much smaller than the two runs at a dose rate of 2x, meaning the 3x and 4x dosage were more consistent in repeatability than the 2x. Fig. 4-26c also has the some of the smaller standard deviation values, indicating that the 4x dose rate powder bed surface was

smoother. Large standard deviations, such as those seen in Fig. 4-26a, should raise questions about the quality of the powder surface and should prompt another look at the images for any irregularities. Fig. 4-26a also showed that a 2x dosage rate was most likely to produce the surface defects as seen in Fig. 4-25 due to the high standard deviations.

4.4.2.2 Speed Comparison

The average B/D value and the mean pixel area and standard deviation for each region were plotted at 100 mm/s and 200 mm/s to see the effect of speed on surface quality.

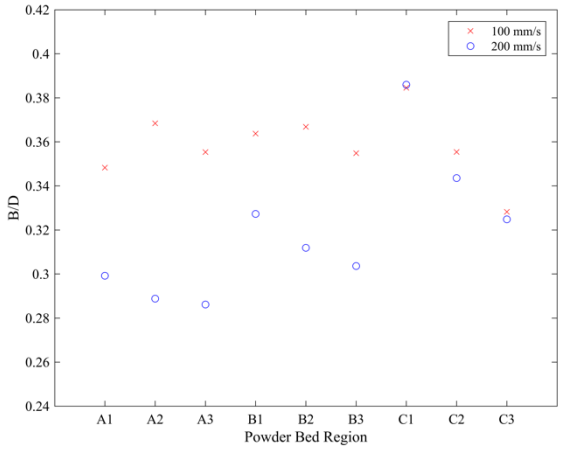

(a) B/D, Dose: 2X

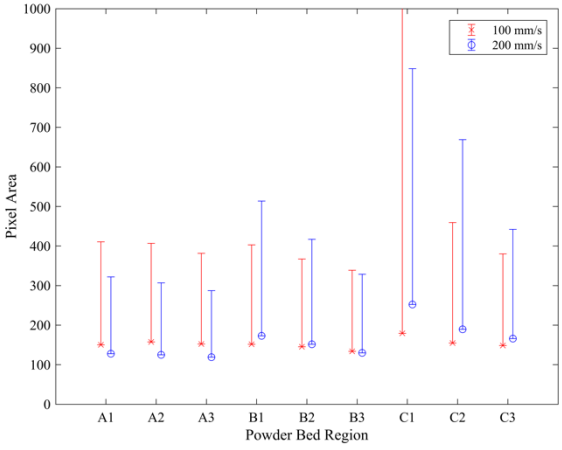

(b) Pixel Area, Dose: 2X

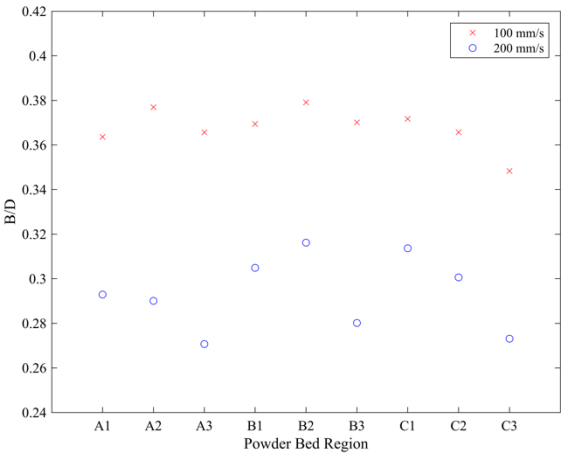

(c) B/D, Dose: 3X

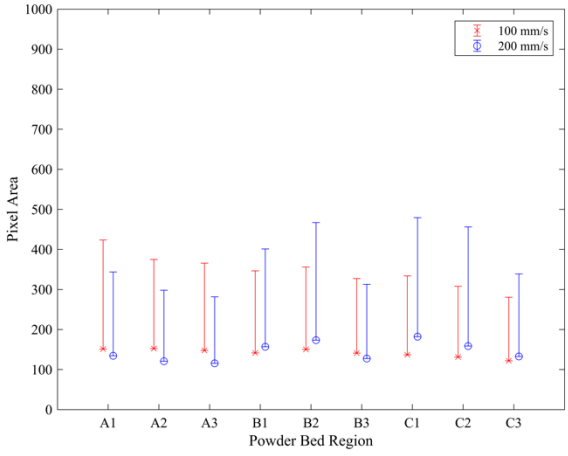

(d) Pixel Area, Dose: 3X

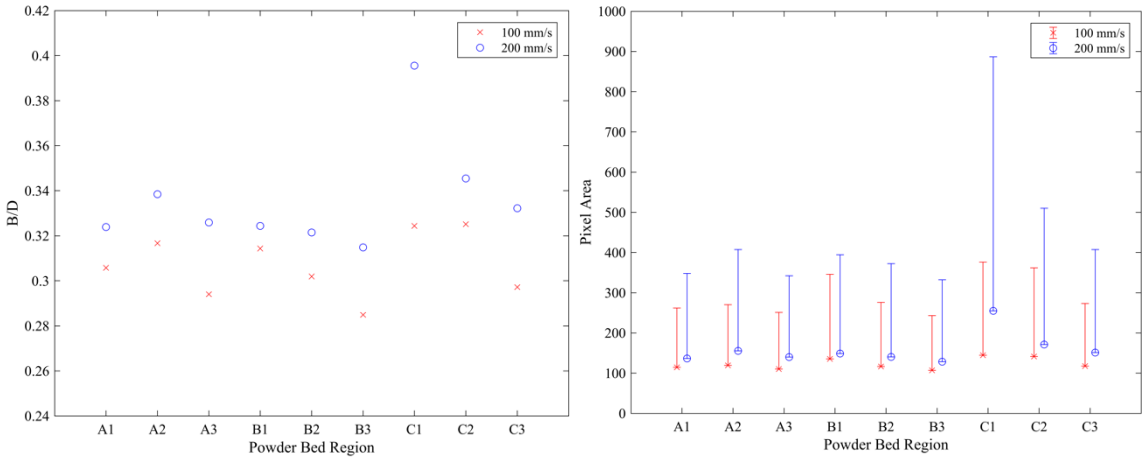

(e) B/D, Dose: 4X

(f) Pixel Area, Dose: 4X

Figure 4-27. Average B/D values and pixel area mean and std. dev. comparing 100 mm/s and 200 mm/s at each dose rate.

The B/D graphs in Fig. 4-27 for the 2x and 3x dose both indicate that 100 mm/s would produce higher values but says otherwise for a dose of 4x. Again, B/D does not indicate the origins of the brightness, unlike looking at pixel area. Ignoring region C1 in Fig 4-27b since the cause has been identified for the spike, for the majority of the regions in each dose rate, the 200 mm/s pixel area means and standard deviations are higher than those at 100 mm/s. Large spikes in standard deviations can be seen for 200 mm/s in regions C1 and C2 for each dose rate. Regions A1-3, B3, and C3 generally tend to have smaller mean and standard deviations, meaning the area is most likely smoother. These values are on the top row of the powder bed when looking at the diagram in Fig. 4-22, which brings into consideration that lighting could have influenced the results despite trying to adjust the distance for each picture, or that the blade was not quite level. A trend of descending pixel area standard deviation and mean from C1 to C3 for each dose rate and from B1 to B3 for a dose rate of 2x and 4x indicated that the regions at the beginning of the spread are more even than at the end.

4.4.2.3 Dosage Comparison

The data from Fig. 4-27 were also rearranged to observe how dose rate affected the surface quality of the powder bed at each speed.

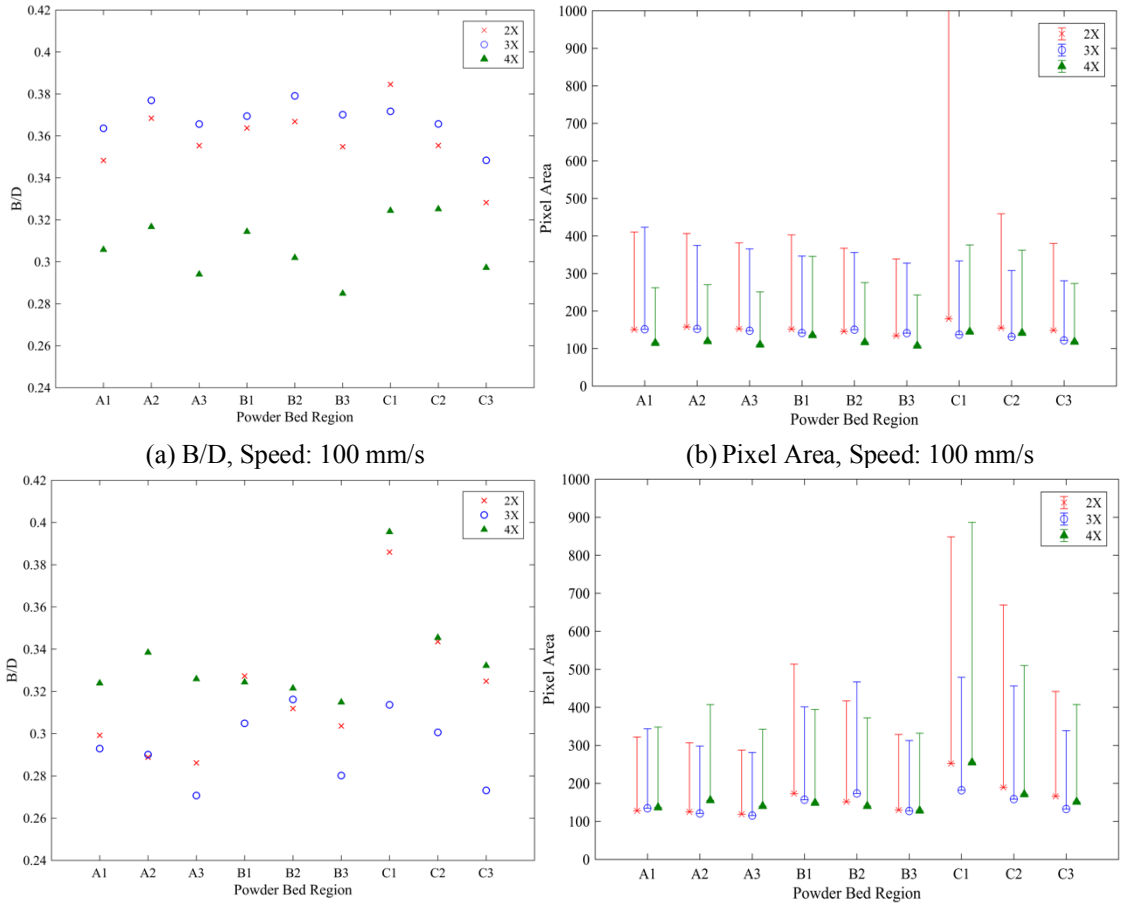

(a) B/D, Speed: 100 mm/s

(b) Pixel Area, Speed: 100 mm/s

(c) B/D, Speed: 200 mm/s

(d) Pixel Area, Speed: 200 mm/s

Figure 4-28. Average B/D values and Pixel Area mean and std. dev. comparing 2x, 3x, and 4x dose rate at different speeds.

Similar to the results from Fig. 4-27, using average B/D values does reveal information about the origins of the brightness as much as the pixel area graphs. When comparing the B/D graph with the corresponding pixel area graph, regions with a high B/D had a higher pixel area standard deviation, indicating that using B/D would not be a confident measure of the quality of the surface. Looking at the pixel area mean and standard deviation graph for 100 mm/s (Fig. 4-28b), the 4x dose rate had less spread than the 2x or

3x dose rate. For the 200 mm/s, except for C1 to C3, the majority of the regions have similar means and standard deviations for when comparing dose rates. Whereas the surface roughness at a dose rate of 4x and 100 mm/s showed consistency across all regions, the same cannot be said for the 200 mm/s. The 2x and 4x dose rate results at 200 mm/s reach similar high amplitudes in pixel area standard deviation, whereas a dose rate of 3x showed smaller standard deviation values.

4.5 Sampling

While imaging captured larger aggregates, sampling allowed for particles to be individually be looked at. For a few of the runs, the powder was build up and then divided into 9 regions. The powder from each of the 9 regions were sampled, and the resulting interquartile range with upper and lower limits of the particle distribution are shown in Fig. 4-29. Since there were 9 samples for each run, testing for particle size distribution turned out to be a time intensive process, and so, due to the time constraints of this project, only 3 runs were tested. A run with a dose of 2x and was run at speed of 100 mm/s was tested along with 2 runs with a dose of 3x at 100 mm/s. For each sample, roughly 100,000 – 300,000 particles were tested using the Malvern Morphologi G3. Summary of the data can be seen in Appendix F.

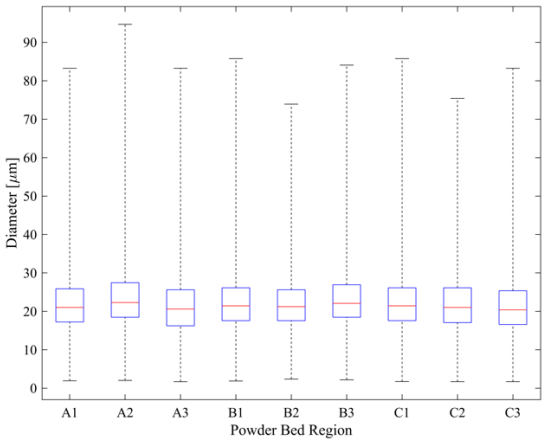

(a) Dose 2X, Speed: 100

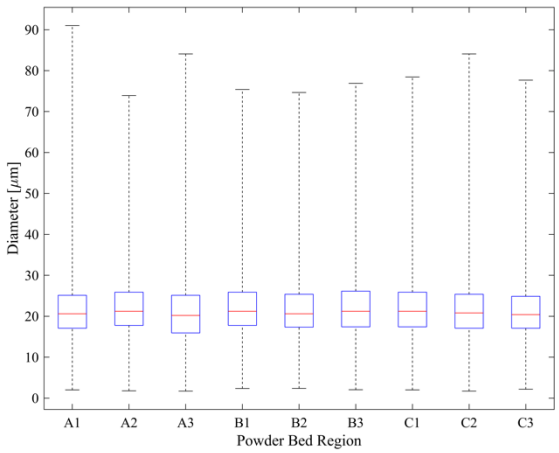

(b) Dose: 3X, Speed: 100 mm/s Run 1

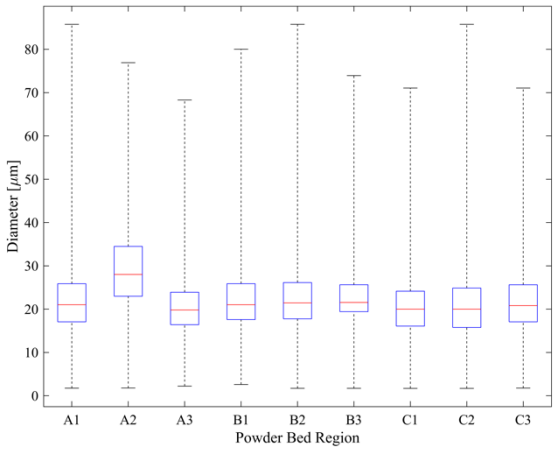

(c) Dose: 3X, Speed: 100 mm/s Run 2

Figure 4-29. Box plots of particle size distribution with upper and lower limits for each region of each run.

Oddly enough, the results from Fig. 4-29a and Fig. 4-29b look quite similar just looking at the interquartile ranges even though they have different doses. This would indicate that the distribution does not vary with dose rate. Overall, each region distribution looked roughly the same for all graphs. When both runs at the 3x dose rate and 100 mm/s (Fig. 4-29b and c) were compared, and the first run had more consistency between regions. This meant that each run did not have repeatable particle size distributions. Also, the upper limits for all of the regions were varied since very few particles were larger than 60 microns in diameter.

4.6 Discussion

Comparing the results of repeated runs, dose rate, and speed provided insight into the roughness quality across the build plate and the influence of input parameters. When looking at the pixel area means and standard deviations for repeated runs for each dose rate, the results did not show a consistent or repeatable pattern between runs. With region C1 of Fig. 4-26a eliminated, a dose of 2x still had the most inconsistent surface roughness between repeated runs. The next step would be to see how much of a difference in the pixel area mean and standard deviation of repeated runs would produce a difference in the final part, as the difference as is might only marginally affect the quality of the part itself.

From looking at each dose rate and the speeds at each dose rate (Fig. 4-27), 200 mm/s showed worse surface quality for the majority of the regions at each dose rate based on pixel area mean and standard deviation. Occasionally, in regions A1-3, the 200 mm/s showed smaller pixel area mean and standard deviation values than at 100 mm/s, but most of the regions consistently showed worse surface roughness at 200 mm/s. A pattern of descending pixel area mean was seen in the B and C regions, indicating that the powder bed surface becomes rougher towards the end of the spreading process. In general, regions A1-3 and C3 appeared to have smoother and more even surface quality than the rest of the powder bed, which could be attributed to possible tilt in the coating blade. Lighting could have also contributed to this pattern since the powder bed was lit from the right, causing uneven illumination of the powder bed despite the efforts to distance the light equally from the camera with each section.

When comparing the dose rates at each speed (Fig. 4-28), a similar pattern of regions A1-3 and C3 appearing to be the smoothest was also seen. The run with a dose rate of 4x

at 100 mm/s had the most consistent surface quality across powder bed regions compared to the other runs. For 200 mm/s, each of the dosages did not show that any one was outstandingly better than the other, though a dose rate of 3x had the smallest range of pixel area standard deviations. Again, how much of a difference between regions and runs is truly effective can only be evaluated by running print tests that show how the differences impact the final part.

Even though this method of qualifying surface roughness has shown to be not perfect, plotting pixel area mean and standard deviation has the capability of detecting abnormalities on the power bed that would trigger a reevaluation of the powder quality or a re-spreading of powder before continuing. Using the B/D graph does not cause enough concern when an abnormality arises in the form of a high B/D value, which would cause an operator to continue without noticing the abnormality. Being able to discover ridges or pit holes in the surface quality would be important to a machinist when printing, since a poor layer can potentially ruin a part.

5. DISCRETE ELEMENT SIMULATION

A discrete element model simulating the powder spreading was created using LIGGGHTS, a discrete element particle simulation software, to compare to the experimental results and to better understand the physics of powder behavior [41]. This model helped with understanding whether or not powder has an inherent patterned behavior that was not observed in the experiment. Another goal for designing a powder bed forming simulation was to potentially incorporate experimental observations to improve the behavior of the model.

5.1 Discrete Element Method Basics

The Discrete Element Method (DEM) was first developed by developed by Cundall and Strack [23] to study rock and other granular materials at a microscopic level. Realistic modeling of particle deformation is very complex, especially with millions of particles, and so, with DEM, the interaction force is related to the overlap of the particles for simplification. At every timestep, the position, velocity, and contact forces are updated by solving Newton's equations of motion for translational and rotational degrees of freedom:

$$m_i \frac{d^2}{dt} x_i = \sum_c f_i^c + m_i g \tag{5-1}$$

$$I_i \frac{d}{dt} \omega_i = \sum_c t_i^c \tag{5-2}$$

where in the translational equation m is the mass of particle i, x is the position, f_i^c is each force on the particle due to neighboring particles or walls. In the rotational equation, I is the moment of inertia, ω is the angular velocity and t_i^c is each torque caused by tangential force or other moments such as those from rolling or collision.

5.1.1 Contact Model with Cohesion

The contact forces that contribute to the equations of motion are calculated using force-displacement contact algorithms, such as the Hertz – Mindlin model that was used in LIGGGHTS [23,40-43].

The contact force when two particles collide is the sum of the normal and tangential forces:

$$F = F_N + F_T \tag{5-3}$$

The normal force is equal to

$$F_N = k_n \delta_n - \gamma_n v_n \tag{5-4}$$

where k_n is the Hertz normal stiffness, δ_n is the overlap distance, γ_n is the damping constant, and v_n is the normal relative velocity between the two particles. The normal force equation resembles a spring-dashpot model.

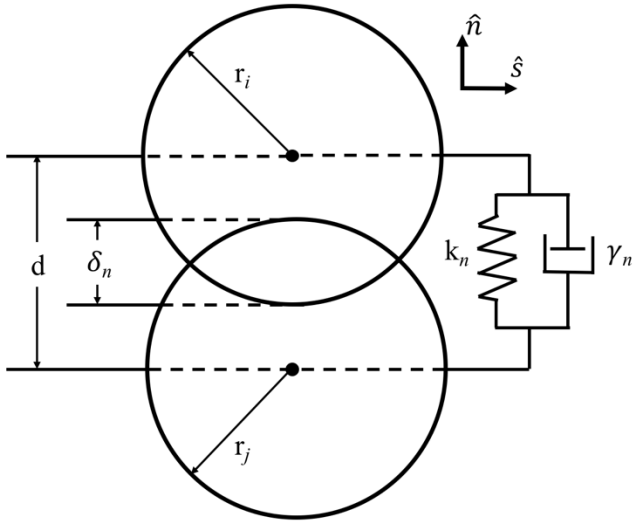

Figure 5-1. Spring-dashpot model for normal contact force.

The normal stiffness and damping constant can be solved using:

$$k_n = \frac{4}{3} E^* a \tag{5-5}$$

$$\gamma_n = -\beta \sqrt{5 k_n m^*} \tag{5-6}$$

Where E^*, r^*, and m^* is the effective Young's modulus, radius, and mass respectively, a is the radius of the contact area, and β is the damping ratio derived from e, the coefficient of restitution. These variables can be solved using the following equations:

$$\frac{1}{E^*} = \frac{(1 + {\nu_1}^2)}{E_1} + \frac{(1 + {\nu_2}^2)}{E_2} \tag{5-7}$$

$$\frac{1}{r^*} = \frac{1}{r_1} + \frac{1}{r_2} \tag{5-8}$$

$$\frac{1}{m^*} = \frac{1}{m_1} + \frac{1}{m_2} \tag{5-9}$$

$$\beta = \frac{\ln(e)}{\sqrt{\ln^2(e) + \pi^2}} \tag{5-10}$$

$$a = \sqrt{r^* \delta_n} \tag{5-11}$$

For the tangential contact force,

$$F_T = k_t \delta_t - \gamma_t v_t \tag{5-12}$$

where k_t is the tangential Hertz stiffness, δ_t is the tangential overlap, γ_t is the tangential damping constant, and v_t is the relative tangential velocity.

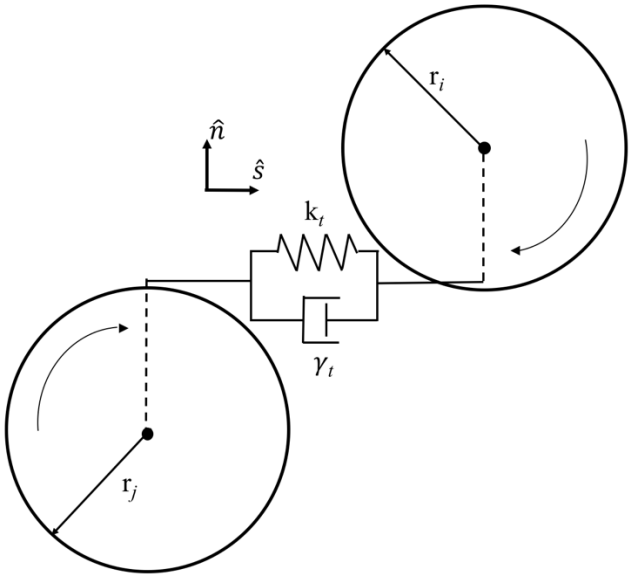

Figure 5-2. Spring-dashpot model for tangential contact force.

In similar fashion to the normal force,

$$k_t = 8G^* a \tag{5-13}$$

$$\gamma_t = -2\sqrt{\frac{5}{6}}\beta\sqrt{k_t m^*} \tag{5-14}$$

with the effective shear modulus G^* equal to

$$\frac{1}{G^*} = \frac{2(2-v_1)(1+v_1)}{E_1} + \frac{2(2-v_2)(1+v_2)}{E_2} \tag{5-15}$$

To incorporate cohesion, LIGGGHTS has the option to use the simplified Johnson-Kendall-Roberts (SJKR) model. This model adds an addition normal force to maintain contact between two particles.

$$F_{coh} = k_{CED} A \tag{5-16}$$

The cohesive force consists of k_{CED}, the cohesion energy density (CED) and A, which is the contact area when in contact.

$$A = \frac{\pi}{4}\frac{(d - r_1 - r_2)(d + r_1 - r_2)(d - r_1 + r_2)(d + r_1 + r_2)}{d^2} \tag{5-17}$$

where d is the distance between the two centers.

Typically, van der Waals forces are defined using surface energy (mJ/m^2), which does not have the same units as cohesion energy density (J/m^3). Currently there is no way to correlate the two, and so estimates must be made by checking with the results of the simulation and adjusting the parameter based on the desired behavior.

5.1.2 Integration with Velocity Verlet

To get the positions and velocities at each timestep for every particle, the forces need to be integrated and the most popular method in DEM is the velocity Verlet integration scheme [44].

The basis for the method are the Taylor series expansions for position, velocity, and acceleration at one timestep forward:

$$\vec{x}(t + \Delta t) = \vec{x}(t) + \vec{v}(t)\Delta t + \frac{1}{2}\vec{a}(t)\Delta t^2 + O(\Delta t^3) \tag{5-18}$$

$$\vec{v}(t + \Delta t) = \vec{v}(t) + \vec{a}(t)\Delta t + \frac{1}{2}\vec{\dot{a}}(t)\Delta t^2 + O(\Delta t^3) \tag{5-19}$$

$$\vec{a}(t + \Delta t) = \vec{a}(t) + \vec{\dot{a}}(t)\Delta t + +O(\Delta t^2) \tag{5-20}$$

For the velocity Verlet scheme, the first task is to calculate the velocity at half the timestep from Eq. 5-19.

$$\vec{v}\left(t + \frac{1}{2}\Delta t\right) = \vec{v}(t) + \frac{1}{2}\vec{a}(t)\Delta t \tag{5-21}$$

From the velocity, the position at the full timestep can then be calculated by substituting Eq. 5-21 into Eq. 5-18:

$$\vec{x}(t+\Delta t) = \vec{x}(t) + \vec{v}\left(t+\frac{1}{2}\Delta t\right)\Delta t \tag{5-22}$$

The acceleration $\vec{a}(t+\Delta t)$ can be derived from summing the contact forces at the full timestep and then evaluating Eq. 5-1.

Then the velocity at this full timestep can be calculated. In order to solve for the velocity, Eq. 5-20 needs to be rearranged to solve for $\vec{a}(t)$ and multiplied by $\frac{\Delta t}{2}$ so that the order and the left-hand term matches the term in the velocity equation.

$$\tfrac{1}{2}\vec{a}(t)\Delta t^2 = \tfrac{\Delta t}{2}(\vec{a}(t+\Delta t) - \vec{a}(t)) + O(\Delta t^3) \tag{5-23}$$

Plugging in Eq. 5-23 into Eq. 5-19, the velocity equation used for the full timestep is

$$\vec{v}(t+\Delta t) = \vec{v}(t) + \frac{\Delta t}{2}(\vec{a}(t+\Delta t) + \vec{a}(t)) \tag{5-24}$$

5.2 LIGGGHTS

LIGGGHTS is an open source software for simulating granular materials using the discrete element method and is distributed by DCS Computing GmbH [41]. LIGGGHTS stands for LAMMPS Improved for General Granular and Granular Heat Transfer Simulations. LAMMPS is a molecular dynamics simulation code developed at Sandia National Laboratories, and LIGGGHTS was built off of LAMMPS for improved granular modeling. The program added features such as contact force formulation, optional cohesion and rolling friction, the import of CAD geometries, and more particle insertion choices that made this software the best choice for this project. LIGGGHTS can be run on a single processor desktop but was designed to run in parallel.

The code for LIGGGHTS is written in C++ and executes a text input file that defines the characteristics of the simulation. LIGGGHTS also has a Python interface,

which made learning how to use the software much easier. For use with Python, the software had to be built as a dynamic shared library, which allowed the program to be run through Python in any directory as long as the paths were defined for the Python wrapper and the LIGGGHTS library in a .bashrc or .bash_profile file.

5.2.1 LIGGGHTS Visualization

For the simulation, a retaining box to hold powder in, a powder bed base, and a blade were modeled in SolidWorks, a solid model computer aided design program. The models needed to be assembled and then saved separately by hiding other models for LIGGGHTS to properly arrange each model in the simulation with the same coordinate system. LIGGGHTS requires CAD files in STL format, but the mesh created when exporting from SolidWorks was not fine enough for the simulation, and so the models were saved as STEP files. The geometries were then meshed in Gmsh where the STL was split into finer triangles and smoothed out [45]. When LIGGGHTS loaded the STL files, the dimensions were set to the units specified in the input file, and so each geometry needed to be scaled accordingly.

LIGGGHTS does not have a GUI and cannot post-process the output files, so Paraview was used to visualize the results [46]. Paraview is an open source data analysis and visualization platform that can load large data sets and display resulting particle velocities, forces, temperatures, and distributions from the simulation. The LIGGGHTS code produces a dump text file at specified timestep increments that require modification before the file can be read by Paraview. The dump files need to be converted to VTK format using LPP, a python program created in conjunction to LIGGGHTS to read dump files. The vtk.py file used in LPP had to be modified to round extremely small numbers ($\sim 10^{30}$)

to zero so that Paraview did not encounter errors. Paraview also takes accompanying dump STL files that can help visualize the geometries at each timestep. After the files had been converted, they could be opened as a group in Paraview for visualization. Another program that was used was OVITO [47], which proved to be much faster in interpreting the dump files and graphically more efficient than Paraview. OVITO does not support STL files and so Paraview was used to visualize the geometries.

5.2.2 Input File

A LIGGGHTS input file defines the properties of the simulation which includes simulation bounds, material properties, particle size, how the particles are inserted into the simulation, geometries, and particle interaction physics. There is no particular order to how properties are defined, but certain commands can be prompted at specified stages of the simulation. There are generally 7 parts to an input file: the initialization, particle definition, particle insertion, geometries, physics, integration, and execution.

In the initialization step, the simulation domain was established. Here, the units were defined, as well as the particle style, which for this simulation was granular. The boundary style for the simulation box defined how particles behave when they reach the bounds of the box. The bounding box itself must accommodate all of the initial particles generated. The boundary style could have been set to *'m*,' which expands the bounds of the simulation box to accommodate particles that try to go past the box size, but trying to keep the data of all the particles that fall off increased computation time and space. Instead, the boundary style was set to *'f,'* or fixed, which allowed particles to disappear when they passed the boundary. This tended to cause dangerous builds when running the program, but the dangerous builds were zero when using the *'m'* boundary style, and so this was not

a concern. '*newton'* was turned off, meaning newton's third law does not apply, saving computation time, making it a popular choice in DEM simulations.

For the simulation setup, particle properties and geometry details were defined. A list of properties used for the simulation can be seen in Table 5-1. The common values used in this simulation such as density, coefficient of friction, Young's modulus, and Poisson's ratio were those typically found for stainless steel and aluminum. In DEM simulations, realistic values for the Young's modulus of steel and aluminum do not work well, since stiffer particles result in high interparticle forces that make the simulation unstable. Also, a high Young's modulus reduces the timestep drastically, which is inefficient. Lommen et al. [38] investigated the effects of particles stiffness on bulk material behavior in hopes of speeding up DEM simulations. From their angle of repose test, shear moduli between 10^7 and 10^{11} Pa showed little difference in the angle of repose and bulk density. The Young's modulus for stainless steel and aluminum is roughly 200 GPa and 69 GPa respectively, but for this simulation 2.5 x 10^7 Pa was used the particles and 0.7 x 10^7 Pa was used for the walls in order to increase the allowable timestep.

The coefficient of restitution and the coefficient of friction were also defined for atom type pairs: particle to particle, and particle to wall. In order for cohesion to be added to the model, cohesive energy density had to be defined, which is a unique variable specific to LIGGGHTS. Typically, surface energy is defined for cohesive forces. For cohesive energy density, values were difficult to find, and so estimates that worked well in the simulation were used. The value was estimated by checking the stability of the simulation and observing how the particles behaved, and so experimenting with varying cohesive energy density values in the future could help improve the simulation.

Table 5-1. Particle and wall material properties for the simulation.

Property	Symbol	Atom Type or Pair	Value	Units
Young's Modulus	E	P W	2×10^7 0.69×10^7	Pa
Poisson's Ratio	ν	P W	0.28 0.35	-
Coefficient of Restitution	COR	P/P P/W W/W	0.6 0.5 0.5	-
Coefficient of Friction	μ	P/P P/W W/W	0.6 0.8 0.8	-
Density	ρ	P	8000	kg/m^3
Cohesive Energy Density	E_{coh}	P/P P/W W/W	50000 50000 50000	J/m^3

P – Particle, Stainless Steel
W – Wall, Aluminum

Based on the particle size distribution results from Section 3.5.2, the distribution of the particles was shown to be not Gaussian. In order to roughly replicate the distribution, the data from a single run of the distribution test were grouped into nine bins and the sum of the percent of particles were calculated for each bin. Each bin was then assigned a particle diameter ten times the largest diameter in the bin for the simulation. The diameter size was scaled larger for efficiency sake, as it would require less particles, and would increase the allowable timestep, while still being able to provide some insight into how the powder might behave. The effects of scaling particles were not observed for this thesis, but could be an area for future work.

Table 5-2. Particle size and distribution used for the simulation.

Diameter Range [μm]	Percent [%]	Simulation Diameter [μm]
1-10	5.6550	100
11-20	36.1300	200
21-30	45.0000	300
31-40	11.0000	400
41-50	2.0000	500
51-60	0.2000	600
61-70	0.0100	700
71-80	0.0045	800
81-90	0.0005	900

For particle insertion, the *insert/stream* method proved to work the best for this simulation. The particles could be inserted after every few timesteps or just once. The particles were filled into a defined region and the fill was limited to a volume fraction of 0.6 (on a scale of 0 to 1) since a higher value could cause particles to have high overlap. Due to the volume fraction, the packing region was taller than the intended height in order to produce more than enough particles. Also, allowing more space for particle generation allowed for the full distribution of particles to be inserted, since the smallest and largest particles tended to not get generated when the height was too short. The particles were dropped into the simulation, allowed time to settle, and then the particles above a certain height from the base were deleted.

Each CAD geometry was imported with the proper material type and scaled according to the defined units. They were defined as granular walls, allowing particles to interact with the walls when they were close. This simulation used Hertzian contact mechanics for interactions between particles. A matching pair style was chosen which set the equations that would impose a force between two neighboring particles. For this model,

cohesion was added to the pair style using the simplified JKR model (SJKR). Walls were not added to the sides of the simulation to keep the particles in the center since, realistically, the majority of powder falls off on the sides during the spreading process.

The position, velocity, and angular velocities of each particle were updated using the velocity Verlet time integration scheme with constant NVE (N = number, V = volume, and E = energy). To determine the appropriate timestep, the Rayleigh time was calculated first.

$$dt_{rayleigh} = \frac{\pi r_{sphere}}{0.1631(\nu + 0.8766)}\sqrt{\frac{\rho}{G}} \tag{5-25}$$

Where r_{sphere} is the radius of the smallest particle, ρ is the density, and G is the shear modulus defined by:

$$G = \frac{E}{2(1+\nu)} \tag{5-26}$$

Where E is the Young's modulus. To ensure stability, the timestep is typically set to 20% of Rayleigh time or preferably even less.

$$dt = 0.2 * dt_{rayleigh} \tag{5-27}$$

For the simulation the 0.1 μs was used as the timestep, which was significantly less than 20% of the Rayleigh time.

The command *run* starts the execution of the simulation, but before that, information desired in the output dump files must be specified as well as how often to create a dump file. A single dump file can be created for efficiency, or a dump file can be created at every timestep as well. The number of timesteps to run are specified and using

upto allowed for a pause to modify properties. In this simulation, the retaining wall was removed, and the blade was motioned to move linearly at 100 mm/s or 200 mm/s until it reached the end of the base, which was roughly 5,000,000 timesteps. Due to the long run times of the simulations, only dose rates of 2 and 4 were simulated at 100 mm/s and 200 mm/s. The input file can be found in Appendix F.

5.2.3 Geometry

The simulation consisted of a base with a square depression acting as a build well. The build area was 20mm x 20mm. The particles were generated within the retaining box, which also helped the particles keep their shape as they settled. After the particles settled, the particles above a desired height are removed from the simulation. Since the build area depth or layer height was 0.5mm, if the dose rate was 2x, the particles above 1mm were eliminated. The retaining box was unfixed as soon as the blade began to move, so the blade was able to spread through the retaining box. The blade had to spread a distance of 50 mm. The gap between the blade was chosen to be 0.5 mm, since the total gap including the build depth would be 1 mm and would allow for the largest particles to fall under the blade if given the chance.

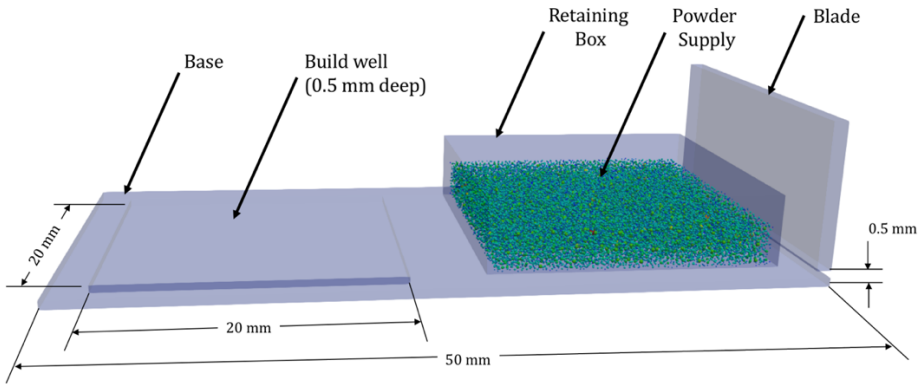

Figure 5-3. Simulation CAD geometries and dimensions.

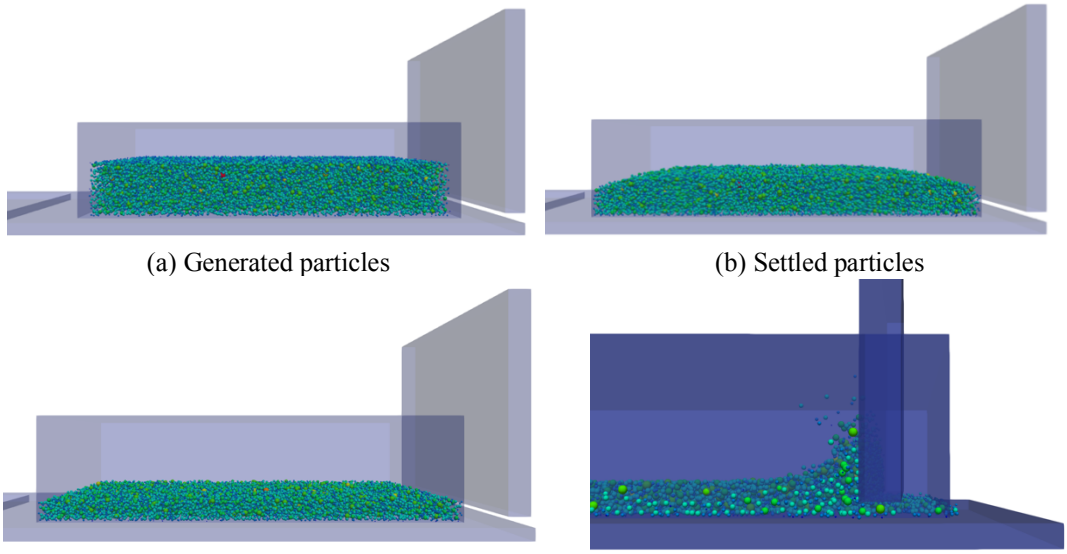

(a) Generated particles (b) Settled particles

(c) After deletion (d) Spreading

Figure 5-4. Particle insertion and spreading from simulation.

5.3 Results

From the simulated results, surface roughness was difficult to obtain for each region of the build area since neither of the post-processors could do this calculation. Paraview and OVITO were able calculate PSD for the entire group of particles or selected areas, which meant that each region would need to be individually isolated and selected.

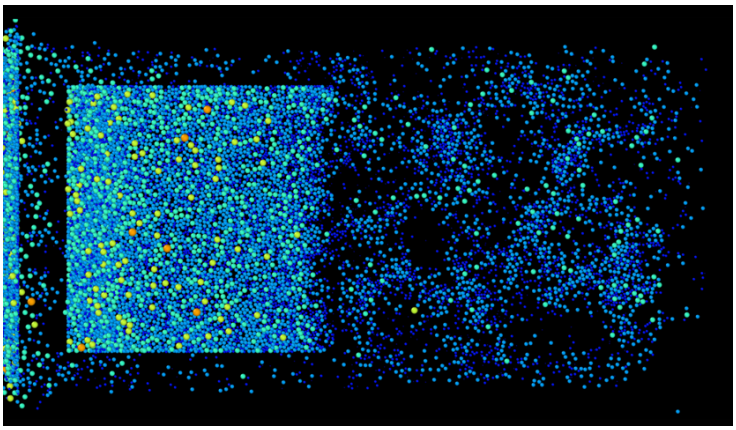

Figure 5-5. Simulation result for a dose of 2x and speed pf 100 mm/s. Color spectrum ranges from red = 450μm to blue = 50μm.

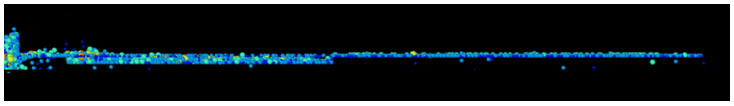

Figure 5-6. Side view to Fig. 5-5.

The particles were color coded according to size in OVITO, with the color spectrum spanning from with blue equaling 50μm red to equaling a radius of 450μm. Just by looking at the color coding, a pattern of particle placement can be immediately detected. The majority of the smaller dark blue particles were left behind during the spreading process, and as the blade began sweeping over the build area, the smaller particles settled. The start of the build area was also not as well packed as the end. The medium and larger particles started to lay down about a fifth of the way into the spread. The end of the build plate shows a decent number of green particles in the area, which would imply a rougher surface and that the PSD leaned towards larger particles.

5.3.1 Surface Roughness from Profile

Trying to compare the surfaces generated from the simulation with the experimental results proved to be difficult. The image processing method used to assess surface roughness in Section 4.3 did not work since the simulation images lacked the shadow and contrast needed for segmentation. Instead, the method described in Section 2.2 for measuring the RMS value of a surface profile was used. Three slivers of each of the simulated powder beds were taken and projected onto the y-plane in OVITO. The image was saved and put through the Canny edge detector in MATLAB to trace the surface profile. From the binary profile image, pixel height values of the profile were recorded, as seen in Fig. 5-7. As a reference, the bottom of the simulation box to the floor of the build well was 0.5mm, which helped scale the pixel heights into a millimeter value.

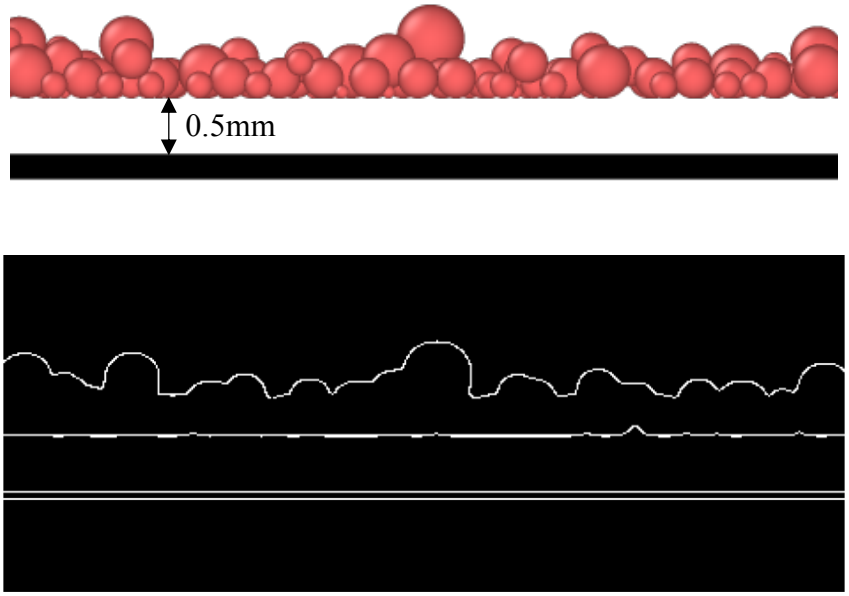

Figure 5-7. Example of a simulation image used for surface profile and the corresponding edge detected image. The distance from the base of the build well to the simulation base was 0.5 mm, which was used as a reference for height.

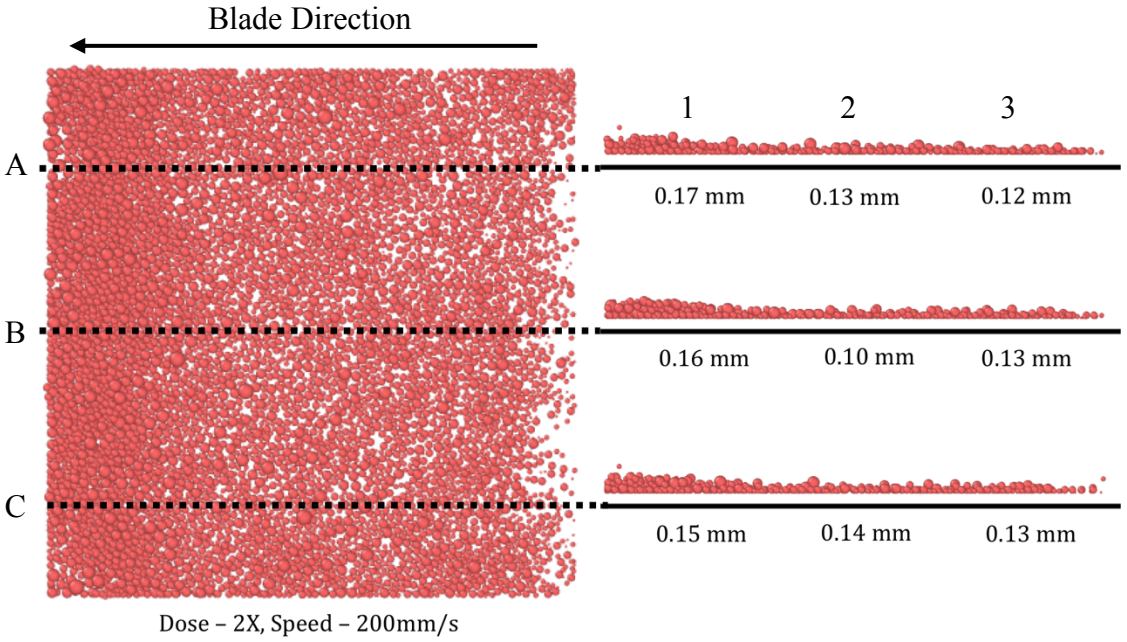

Figure 5-8. Profiles taken from the powder bed and corresponding RMS values at 3 regions along each profile for a total of 9 values. (Dose – 2X, Speed – 200mm/s)

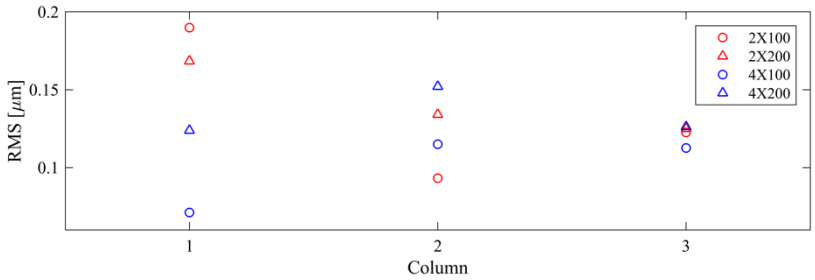

(a) Row A

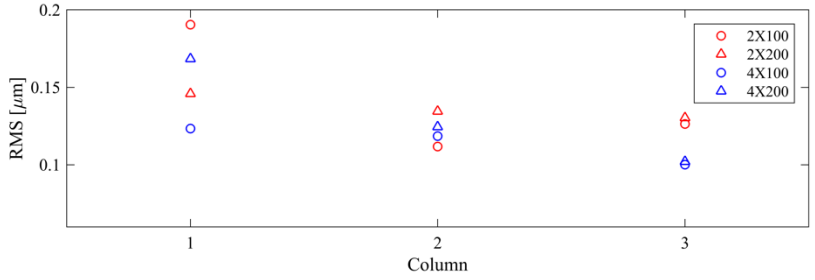

(b) Row B

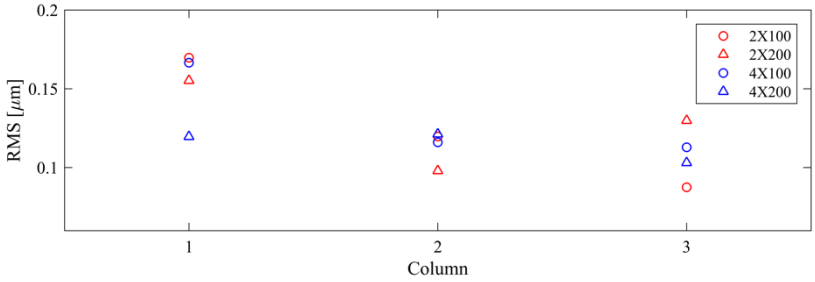

(c) Row C

Figure 5-9. RMS values for each region in each row of Fig. 5-8 for all simulation runs (2X100 means dose – 2x, speed – 100mm/s)

Fig. 5-8 showed a larger pileup of powder particles at the end of the sweep in column 1 and very few particles at the other end of the powder bed. This could have been a result of the particles being pushed too fast and not having enough the time to fully settle at the beginning of the build area. The pileup was expected to have a higher RMS value since the pileup created a sloped surface, and that was well represented in Fig. 5-9. Column 1 had higher RMS values compared to columns 2 and 3 for every row except for the run with a dose rate of 4 and a speed of 100 mm/s in row A. This was reasonable since the dose rate provided more powder particles and the slower rate allowed more time for powder to settle than at 200 mm/s. Columns 2 and 3 had a small range of RMS values across all runs

which possibly could be attributed to having less particles. Differences in dose rate or coating speed do not appear to influence the surface roughness in a predictable fashion except that for every row, column 1 shows a higher RMS value for a dose rate of 2x and 100 mm/s when compared to a dose rate of 2x and 200 mm/s.

5.3.2 PSD Analysis

Particle size distribution simulation results were obtained for a dose rate of 2x and 4x and coating speeds of 100 mm/s and 200 mm/s. To get isolate individual regions to evaluate for PSD, the simulation was processed in OVITO. Planes were applied to slice the powder bed until the region desired was visible. Then using manual selection, the area visible was selected. The histogram data was saved and compiled together for comparison. Looking at the resulting powder bed, the green regions of Fig. 5-10 which mark the beginning of the spread were not always fully covered in powder, and so total particle count tended to be less.

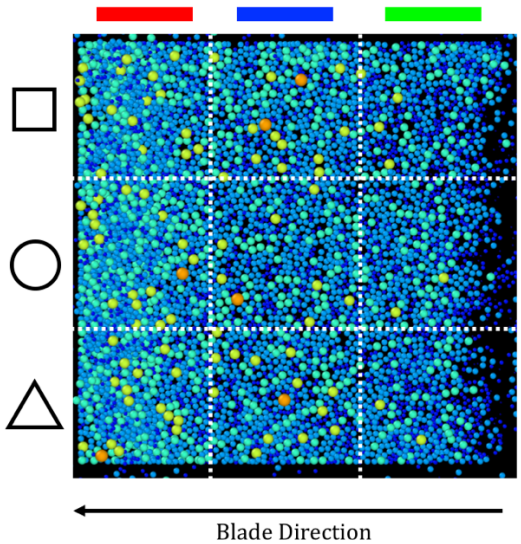

Figure 5-10. Build area divided into regions with columns corresponding to colors and rows corresponding to shapes for reference of Fig. 5-11. See Fig. 4-22 for region label diagram. (Dose – 2X, Speed – 200mm/s)

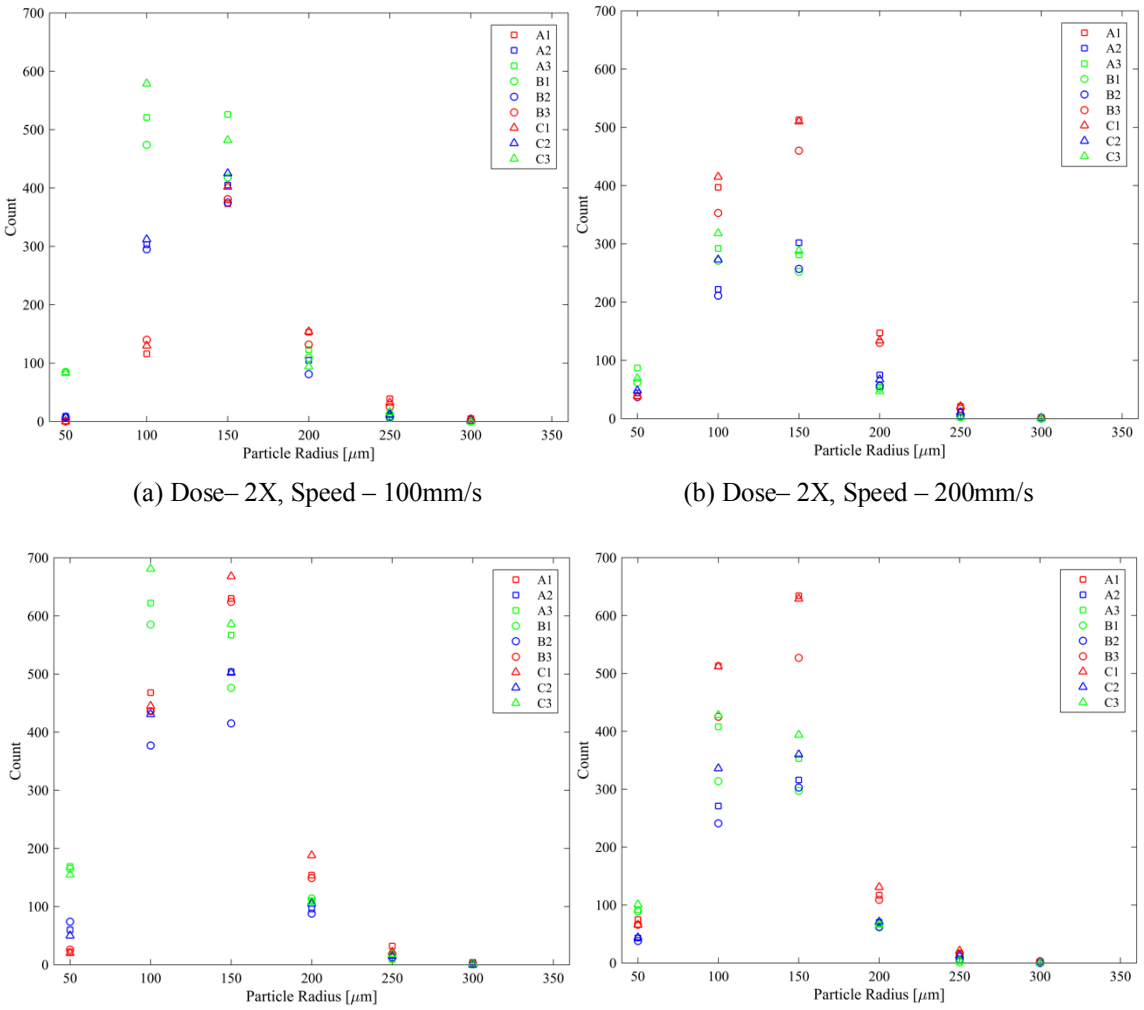

(a) Dose– 2X, Speed – 100mm/s

(b) Dose– 2X, Speed – 200mm/s

(c) Dose– 4X, Speed – 100mm/s

(d) Dose– 4X, Speed – 200mm/s

Figure 5-11. Histogram count for each simulation run with regions defined in Fig. 5-10 for reference.

The green regions from Fig. 5-10 contain the three areas at beginning of the spread, and in Fig. 5-11, those regions show the greatest number of 50μm radii particles for every run. The green regions also have little to no particles with a radius of 250 or 300μm. Looking at Fig. 5-11b through d, the regions in the red column tend to have the largest count of particles over a radius of 150μm. Comparing the rows (shapes) across the build plate did not show any visible consistent trends that were notable.

When comparing dose rates, the 4x simulation results have higher counts of 100 and 150μm radii particles in each region. The dose rate of 4x at a speed of 100 mm/s had

the most 50 and 100 μm radii particles deposited in the green regions, as well the highest total count of finer particles (50 to 150μm) on the entire build area. Other than that, all runs had the same distribution of 200-300μm particles across the build plate. When comparing speeds, runs at 100mm/s had higher total particle counts than at 200 mm/s. Also, with slower speeds, the green regions significantly increased in counts of 50-150μm particles compared to 200 mm/s, whereas 200mm/s increases the number of 100 and 150μm particles in the red regions at the end of the spread. The majority of the particles tended to lie in the red regions at the end of the powder bed except for at a dose rate of 2x and a speed of 100 mm/s which had the highest count of particles in the green regions.

5.4 Discussion

A discrete element simulation was created to further observe the spreading process, and the results did show patterns of surface roughness and particle size distribution in areas of the powder bed. The dose rates simulated were 2x and 4x, along with coating speeds of 100 mm/s and 200 mm/s. From the particle size distribution results from Fig. 5-11, slowing the coating speed and increasing the dose rate increased the number of particles in the build area, especially the finer particles. The green regions, or column 1 of Fig. 4-22 consistently had the highest number of 50μm radii particles and consisted of mainly of particles under 150μm. Increasing dose rate increased the particle count in each region and increasing speed increased the number of particles in the red regions or column 2 of the build area. Slowing down the speed to 100 mm/s, finer particles increased in the green regions at the beginning of the spread. The particle count for 200μm radii particles or larger in each region varied very little despite the change in dose rate and speed.

RMS surface roughness values were also calculated for 9 regions across the build area for each of the 4 runs. From Fig. 5-8, different RMS values were expected across the build area since the profiles showed a pileup of powder at the end of the spread, and very few particles at the beginning. With even slower coating speeds, the particles might have had more time to settle at the beginning of the spread, possibly resulting in a denser area with more particles. Column 1 in Fig. 5-9 showed higher RMS values, which was attributed to the particle pileup in that region. Other regions showed lower RMS values that could be attributed to the number of finer particles noted in Fig. 5-11. In terms of the influence of dose rate and coating speed on surface roughness, there was no visible pattern seen in Fig. 5-11.

The simulation results did match the results seen from the experiment, and a reason could be the simulation details. This simulation used larger particles, which might not perform the spreading process exactly the same if not scaled since the bulk properties were not adjusted. The size of the build area for the simulation was about the size of one region of the actual powder bed, and so the distribution seen in the simulation could have well been within one image taken for the experiment. If this was the case, the distribution seen in the simulation would be lost in the image when analyzed. The areas of higher surface roughness predicted by the image processing method were not the same areas seen from the simulation. This simulation also only spread one layer of particles on top of a flat base without any initial underlying particles. In the experiment, layers of powder were built up, and so the images of powder easily could have contained powder particles from previous layers. Adding consecutive layers of powder to the simulation could change the surface roughness and particle size distribution predicted.

6. CONCLUSION AND RECOMMENDATIONS

The focus of this thesis was to determine how surface roughness and particle size distribution varied across the powder bed used in metal additive manufacturing, and to understand how these characteristics are affected by changes in dose rate and coating speed. Looking at surface roughness and particle size distribution of a powder bed could give insight into how to assess the powder bed to prevent defects in a final part as well as regions that might produce better quality parts. This project was proposed by Lawrence Livermore National Laboratory, and to support this project they designed a powder spreading machine that replicated the powder spreading process without the bulk of a laser. The powder spreader was used to build up layers of powder, and a camera was set up to take images of the build area in 9 different regions. Using image processing in MATLAB, the aggregates in the powder bed of each image were segregated. The brightness to darkness ratio and the pixel area mean and standard deviation were calculated, which were measures used to assess the roughness of the powder surface. Powder samples were also collected from each of the nine regions to be counted for particle size distribution. In addition to the experiment, a discrete element simulation replicating the spreading process was created in LIGGGHTS to observe the intricacies of particle spreading and to compare with the experimental results.

6.1 Conclusion

From analyzing the results from the experiment, repeated runs showed to be not consistent in Fig. 4-26, with ranges in pixel area mean and standard deviation differing from run to run. Despite this, the 3x and 4x dose rates showed smaller differences in pixel area mean and standard deviation for their repeated runs compared to a 2x dose rate.

When comparing speeds at each dose rate in Fig. 4-27, for the majority of the regions, the pixel area means and standard deviations at 200 mm/s were higher than the values at 100 mm/s, indicating that the surface had much larger objects present and had worse surface quality. Regions A1-3 and C3 tended to have smaller pixel area means and standard deviations than the rest of the powder bed, which brought into question of how level the blade truly was for the experiment as well as whether lighting was a factor. A pattern of increasing pixel area mean and standard deviation from the beginning of the spread to the end for regions B and C show that the powder bed surface increases in surface roughness in the direction of the spreading. In Fig. 4-28, the effect of dose rate was much more apparent with 100 mm/s. The run with a dose rate of 4x showed the most consistent results of smooth surfaces across the build plate.

When the results from the experiment were compared to the results from the simulation, they did not completely agree. In the experiment, the regions with the smoothest surface quality were typically A1-3 and C3 whereas in the simulation C1-3 and B1-3 showed the lowest surface RMS values. Other than that, the simulation also showed increasing roughness in the direction of spreading. At the particle level, the experiment showed little difference in the distribution between regions and between dose rates, but in the simulation, the distribution of finer particles was higher at the beginning of the spread, and the end of the spread had higher particle counts as well. Decreasing the speed and increasing the dose rate increased the number of finer particles present on the build area.

6.2 Recommendations

Due to the time constraints of this project, the set up for the experiment was limited by the resources that were readily available. Better instrumentation could have been

implemented, but was either unavailable, or incompatible due to the size of the powder spreader. A microscope objective lens that has the resolution to view individual particles would have been optimal for photoanalysis of the powder bed surface but would also require much more time to evaluate the entire powder bed surface. A light source that provides light through the lens of the camera would also contribute more even and brighter illumination of the powder bed.

The trial with the sandpaper showed some inconsistencies with the B/D values and pixel area values. As an attempt to mitigate these inconsistencies, the sandpaper should all be the same shade of gray. Another idea would be to sputter the sandpaper samples with gold to prevent any light reflections from the facets on the abrasive grains. Ideally, a sample of something similar to sandpaper made from spheres would work best as a reference.

In terms of the simulation, a lot more could be explored to fully develop the simulation. If ample computational time and power are available, the simulation should be done with a more refined distribution (more bins) using the true, unscaled particle sizes. An angle of repose test should be done with the powder and similarly implemented in a simulation to figure out the proper cohesion energy density value to simulate the true behavior of the powder. Also, more layers should be spread in the simulation to further mimic the experimentation.

REFERENCES

[1] D. Bourell et al., “Materials for additive manufacturing,” *CIRP Annals – Manufacturing Technology,* vol. 66, no. 2, pp. 659-681, 2017.

[2] K.V. Wong, and A. Hernandez, “A Review of Additive Manufacturing,” *ISRN Mechanical Engineering*, vol. 2012, pp. 1–10, 2012.

[3] S. H. Huang, P. Liu, A. Mokasdar, and L. Hou, "Additive Manufacturing and Its Societal Impact: A Literature Review," *The International Journal of Advanced Manufacturing Technology,* vol. 67, pp. 1191 – 203, 2012.

[4] E. Klar, and P.K. Samal, *Powder Metallurgy Stainless Steels: Processing, Microstructures, and Properties*. Materials Park, OH: ASM International, 2007.

[5] R.M. German, *Powder Metallurgy Science*, Second edition, Metal Powders Industries Federation, Princeton, NJ, 1994.

[6] K. Gokuldoss, S. Kolla, and J. Eckert, “Additive manufacturing processes: selective laser melting, electron beam melting and binder jetting – selection guidelines,” *Materials,* vol. 10, no. 6, pp. 672, 2017.

[7] W. E. Frazier, “Metal additive manufacturing: A review,” *Journal of Materials Engineering and Performance,* vol. 23, pp. 1917 – 1928, 2014.

[8] S. Wright, *Powder Bed Fusion Process*. [Image] Accessed 9 Mar. 2018. Available: http://pencerw.com/feed/2015/3/15/3d-printing-titanium-and-the-bin-of-broken-dreams

[9] M. Attaran, “The rise of 3-D printing: the advantages of additive manufacturing over traditional manufacturing,” *Business Horizons,* vol. 60, no. 5, 2017.

[10] S. K. Everton et al., “Review of in-situ process monitoring and in-situ metrology for metal additive manufacturing,” *Materials and Design,* vol. 95, pp. 431-445, 2016.

[11] W. King et al., “Overview of modelling and simulation of metal powder bed fusion process at Lawrence Livermore National Laboratory,” *Materials Science and Technology,* vol. 31, no. 8, pp. 957-968, 2015.

[12] A. E. Patterson, S. L. Messimer, and P.A. Farrington, “Overhanging features and the SLM/DMLS residual stresses problem: review and future research need,” *Technologies,* vol. 5, no. 2, pp. 15, 2017.

[13] J. Slotwinski and A. Cooke, “Properties of metal powder for metal additive manufacturing: A review of the state of the art of metal powder property testing,” *NIST IR 7873,* 2012.

[14] Slotwinski et al., “Characterization of metal powders used for additive manufacturing,” *Journal of Research of the National Institute of Standard and Technology,* vol. 119, pp. 460-493, 2014.

[15] A.B. Spierings, M. Voegtlin, T. Bauer, and K. Wegener, "Powder flowability characterization methodology, for powder-bed-based metal additive manufacturing,” *Progress in Additive Manufacturing,* vol. 1, pp. 9-20, 2016.

[16] ASTM D7481-09, “Standard test methods for determining loose and tapped bulk densities of powders using a graduated cylinder,” *ASTM International,* 2009.

[17] G. Jacob, A. Donmez, J, Slotwinski, and S. Moylan, “Measurement of powder bed density in power bed fusion additive manufacturing processes,” *Meas. Sci. Technol.,* vol. 27, 2016.

[18] E. Katahan, H. Oktem, F. Hacizade, H. Nasibov, and O. Gundogdu, “Measurement of surface roughness of metals using binary speckle image analysis,” *Tribology International,* vol. 43, pp. 307 – 311, 2010.

[19] Y. Fuh, K.C. Hsu, and J.R. Fan, “Roughness measurement of metals using a modified binary speckle image and adaptive optics,” *Optics and Lasers in Eng.,* vol 50, pp. 312 – 316, 2012.

[20] A.M. Hamed, H. El-Ghandoor, F. El-Diasty, and M. Saudy, “Analysis of speckled images assess surface roughness,” *Optic & Laser Tech.,* vol. 34, pp. 243 – 253, 2004.

[21] G.Y. Tian, R.S. Lu, and D. Gledhill, “Surface measurement using active vision and light scattering,” *Optics and Lasers in Eng.,* vol. 45, pp. 131 – 139, 2007.

[22] K. Zeng, D. Pal, and B. Stucker, “A review of thermal analysis methods in Laser Sintering and Selective Laser Melting,” 23rd Annual International Solid Freeform Fabrication Symposium – An Additive Manufacturing Conference, pp. 796 – 814, 2012.

[23] P.A. Cundall and O.D.L. Strack, “A discrete numerical model for granular assemblies,” *Geotechnique,* vol. 29, pp. 47 – 65, 1979.

[24] Z. Xiang, M. Yin, Z. Deng, X. Mei, and G. Yin, "Simulation of forming process of powder bed for additive manufacturing," *Journal of Manufacturing Science and Eng.,* vol. 138, 2016.

[25] R. Ganeriwala and T. I. Zohdi, A coupled discrete element-finite difference model of selective laser sintering," *Granular Matter,* vol. 18(21), 2016.

[26] J. Zhou, Y. Zhang, and J.K. Chen "Numerical simulation of random packing of spherical particles for powder based manufacturing," *Journal of Manufacturing Science and Engineering,* vol. 131, 2009.

[27] H.W. Mindt, M. Megahed, N.P. Lavery, M.A. Holmes, and S.G.R. Brown, "Powder bed layer characteristics: the overseen first-order process input," *Metall. And Mat. Trans. A*, vol. 47(8), pp. 3811 – 3822, 2016.

[28] E.J.R. Parteli and T. Poschel, "Particle-based simulation of powder application in additive manufacturing," *Powder Technology,* vol. 288, pp. 96 – 102, 2016.

[29] E.B. Herbold, O. Walton, M.A. Homel, "Simulation of powder layer deposition in additive manufacturing processes using the discrete element method," *Lawrence Livermore National Laboratory,* LLL-TR-678550, 2015.

[30] S. Haeri, Y. Wang, O. Ghita, and J. Sun, "Discrete element simulation and experimental study of powder spreading process in additive manufacturing," *Powder Technology,* vol. 306, pp. 45 – 54, 2016.

[31] The MathWorks, Inc. Natick, MA, USA. 2017. Image Processing Toolbox (r2017b). Available: https://www.mathworks.com/products/image.html

[32] "Edge detection methods for finding object boundaries in images," The MathWorks, Inc. Accessed Sept. 30, 2017. [Online] Available: https://www.mathworks.com/discovery/edge-detection.html

[33] P. Kovesi, "MATLAB and octave functions for computer vision and image processing," Peter Kovesi, Accessed Oct. 17, 2017. [Online]. Available: http://www.peterkovesi.com/matlabfns/index.html

[34] L.C. Gontard, D. Ozkaya, and R. E. Dunin-Borkowski, "A simple algorithm for measuring particle size distributions on an uneven background from TEM images," *Ultramicroscopy*, vol. 111, pp. 101-106, 2011.

[35] A. Greensted, "Otsu Thresholding," The Lab Book Pages, June 17, 2010. [Online]. Available: http://www.labbookpages.co.uk/software/imgProc/otsuThreshold.html

[36] Y. Fuh, K.C. Hsu, and J.R. Fan, “Roughness measurement of metals using a modified binary speckle image and adaptive optics,” *Optics and Lasers in Eng.,* vol. 50, pp. 312 – 316, 2012.

[37] J.B. Meireles et al., “Effect of metallic surface roughness on the speckle pattern formation at diffraction plane,” *Optics and Lasers in Eng.,* vol. 50, 1731 – 1734, 2012.

[38] S. Lommen, D. Schott, and G. Lodewijks, “DEM speedup: stiffness effects on behavior of bulk material,” *Particuology,* vol. 12, pp. 107-112, 2014.

[39] C. Kloss, C. Goniva, A. Hager, S. Amberger, and S. Pirker, “Models, algorithms and validation for opensource DEM and CFD-DEM,” *Progress in Computational Fluid Dynamics, An Int, J.,* vol. 12, no. 2/3, pp. 140 – 152, 2012.

[40] R.D. Mindlin, “Compliance of elastic bodies in contact”, *Trans. ASME J. Appl. Mech*., vol. 16, pp. 259-268, 1949.

[41] DCS Computing GmbH, JKU Linz, and Sandia Corporation, “gran model hertz documentation,” LIGGGHTS. Accessed Oct. 17, 2017. [Online]. Availaible: https://www.cfdem.com/media/DEM/docu/gran_model_hertz.html

[42] A. Di Renzo and F.D. Di Maio, “An improved integral non-linear model for contact particles in distinct element simulations,” *Chem. Eng. Sci.,* vol. 60, pp. 1303 – 1312, 2005.

[43] K.L. Johnson, *Contact Mechanics*. Cambridge, England: Cambridge University Press, 1987.

[44] N.S. Martys and R.D. Mountain, “Velocity Verlet algorithm for dissipative-particle-dynamics-based models of suspensions,” *Phys. Rev. E,* vol. 59, no. 3, 1999.

[45] C. Geuzaine and J.-F. Reamacle, “Gmsh: A three-dimensional finite element generator with build-in pre- and post-processing facilities,” *Int. J. Numer. Met. Eng.,* vol. 79, no. 11, pp. 1309 – 1331, 2009.

[46] J. Ahrens, B. Geveci, and C. Law,” Paraview – An end-user tool for large data Visualization,” *The Visualization Handbook*, Elsevier, 2005.

[47] A. Stukowski, “Visualization and analysis of atomistic simulation data with OVITO – the Open Visualization Tool,” *Modelling Simul. Mater. Sci. Eng.,* vol. 18, no. 1, 2010. Available: http://ovito.org/

APPENDIX A. GALILTOOLS, LABVIEW

A.1 LabVIEW VI for Capturing Images

SaveImages.vi
T:\VI\SaveImages.vi
Last modified on 5/28/2017 at 12:22 PM
Printed on 1/25/2018 at 10:59 AM

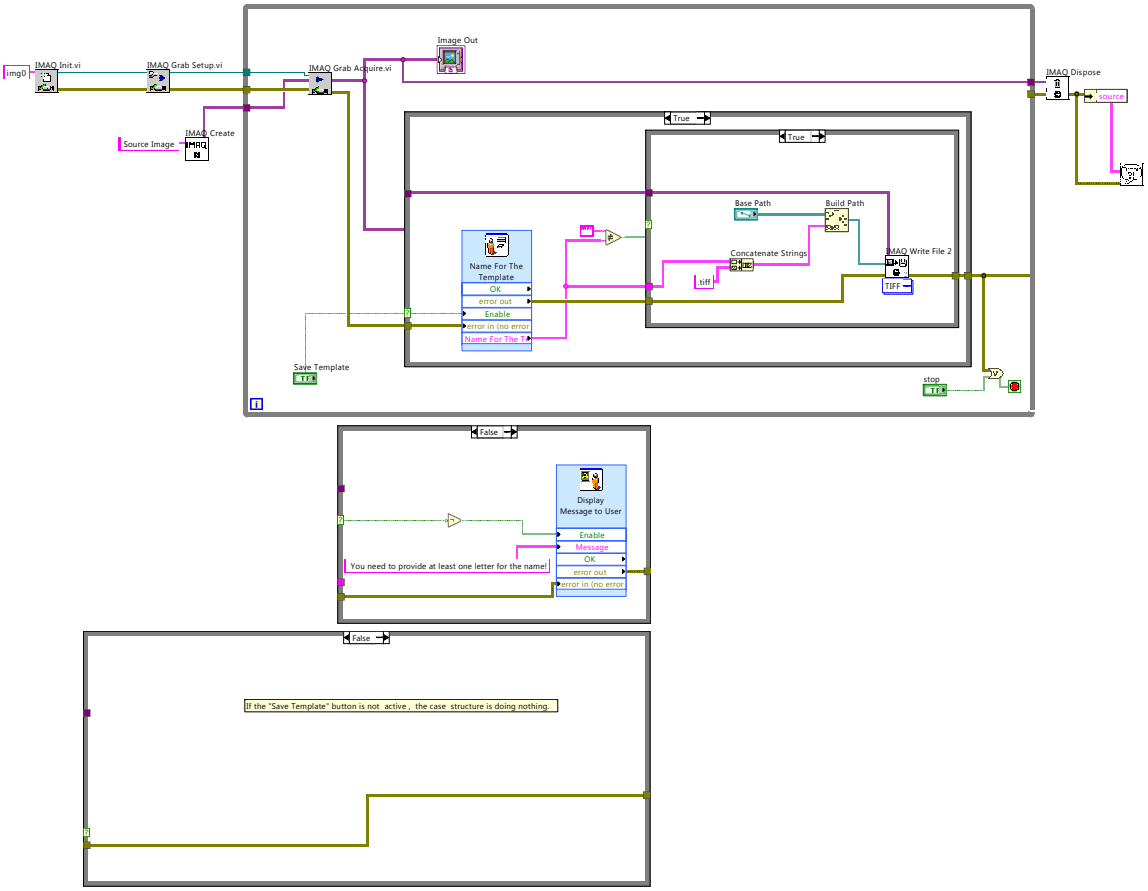

A.2 Galiltools code for Newmark Motor Controller

```
'A: Belt Drive
'B: Build Plate VS
'C: Supply Well VS

#ZERO;' set zero relative position of belt
DPA=0
EN


#SETUPVS; 'vertical stage zeros, will need to adjust B for level height
SPB= 200000
SPC= 200000
PRB= 700000
PRC= -700000
BG BC; AM BC;WT 500
PRB = -148000
PRC = 300000
BG BC; AM BC;
DPB = 0;
DPC = 0;
EN

#HOMEA; ' home belt
SPA= 2777; '100mm/sec
PRA= 70000
BG A; AM A;
EN


#MOVEVS;' moves build plate
PRB = -200000;'-944.88189
PRC = 200000;'944.88189*2
BG BC; AM BC;
EN

#REHOMEA; ' home belt
SPA= 27775; '100mm/sec
PRA= -70000
BG A; AM A;
EN

#BUILDUP
i=1;
#loop
  layerh = 30;
  drate = 3;
  SPB = 200000;
  SPC = 200000;
  PRB = -layerh*31.496063 ;' micron layer height
  PRC = drate*layerh*31.49063;' micron later height*dose rate
  BG BC; AM BC; WT 500;
  SPA= 27775; 'run belt drive over build plate 100mm/sec
  PRA= -70000
  BG A; AM A; WT 500;
```

APPENDIX B. SOP

Standard Operating Procedure for Laboratory Processes

Chemical Name or Process:
Spreading Stainless Steel Powder on Replica Build Plate

Purpose: The main objective of my testing is to observe the rheology of metal powder particles in a powder bed during the process of printing metal parts. To characterize the powder bed field, I will be mostly obtaining qualitative data using a camera to later analyze to determine particle distribution and density along the powder bed.

The iron based powder I will be using is the same powder as used by the RAM Senior Project group, AMA 316 L cl C. The powder is very fine and dense, requiring careful handling procedures due to particulates possibly being exposed in open air. The chemical makeup can be seen in the following table. The nominal particle size is ~40 microns but single particles can vary from 5 to 120 microns in diameter.

Table 1. Composition of Stainless Steel Powder

*** * * Section 3 - Composition / Information on Ingredients * * ***

EC #	Component	Percent	Symbols	Risks
231-111-4	Nickel 7440-02-0	3-14	Xn Carc.Cat.3	R:40-43
231-157-5	Chromium 7440-47-3	1-20	-	-
231-096-4	Iron 7439-89-6	40-95	-	-
231-107-2	Molybdenum 7439-98-7	1-4	-	-
231-159-6	Copper 7440-50-8	0-4	-	-
231-105-1	Manganese 7439-96-5	0-2	-	-

Potential Hazards/Toxicity:

Caution: 316 Stainless Steel Powder may cause sensitization by inhalation and skin contact. Limited evidence of carcinogenic effects.

Chromium: Industrial exposure to chromium may cause dermatitis, skin ulcers, perforation of the nasal septum, as well as cancer of the lungs, nasal cavity and paranasal sinuses.

Molybdenum: May cause irritation to the skin, eyes and respiratory tract.

Nickel: Xn Carc. Cat. 3 Risk: 40-43	This product is or contains a component that has been reported to be possibly carcinogenic based on its IARC, ACGIH, NTP, or EPA classification. Systemic effects from ingestion of nickel include capillary damage, kidney damage, myocardial weakness and central nervous system depression. Allergic skin sensitization reactions are the most frequent effect of exposure to nickel compounds. Contact with nickel compounds may also result in allergic sensitization reactions. Nickel is a possible human carcinogen.
Iron:	Chronic inhalation of iron has resulted in mottling of the lungs, a condition referred to as siderosis. This is considered benign pneumoconiosis and does not ordinarily cause significant physiologic impairment.
Copper:	Chronic copper poisoning is typified by hepatic cirrhosis, brain damage and demyelination, kidney defects, and copper deposition in the cornea as exemplified by humans with Wilson's disease. It has also been reported that copper poisoning has led to hemolytic anemia and accelerates arteriosclerosis. Exposure can cause: damage to the lungs, Stomach pains, vomiting, diarrhea, blood effects.
Manganese:	Prolonged exposure to high concentration of manganese-containing dusts and/or fumes may result in the development of a neurological disorder – Manganism. It is not expected that Manganism will develop if exposures are maintained below 0.2mg/m^3 (PEL). Symptoms of Manganism develop very gradually over a period of years and can include headache, irritability, insomnia, and muscle cramps. In severe cases severe muscle rigidity, and impairment of gait may develop. The symptoms are not always reversible upon cessation of exposure.

Carcinogenicity: No carcinogenicity data available for 316 Stainless Steel Powder. The carcinogenic effect of nickel has been well documented in occupationally exposed nickel refinery workers. Lung and nasal cancers were the predominant forms of cancer in the exposed workers. In experimental animal injections of nickel produced injection site tumors although some of these tumors metastasized. Upon inhalation of nickel, lymphosarcomas were observed in mice and aveolar carcinomas in guinea pigs.

Other Toxicological Information: Exposure to metal dusts and oxides may cause metal fume fever. Metal fume fever is temporary flu-like condition characterized by

chill, fever, muscle aches and pains, nausea and vomiting. Typically, they symptoms appear within a few hours after exposure and subside within 2-3 days with no permanent effects.

Asthma induced by occupational exposure to nickel and cobalt has been documented. The asthma can result from either primary irritation of from al allergic response. Contact dermatitis in workers exposed to nickel compounds is one of the most prevalent effect of nickel exposure.

Engineering Controls:

The test machine and metal powder will be operated under a fume hood in Building 192-135. Tests will be only conducted in this lab, and proper signage will be placed on the door to indicate that testing is in progress, and the room is closed to unauthorized personnel.

Personal Protective Equipment (PPE)

Hand Protection:
Nitrite gloves will be worn when working/ handling the powder. (MSDS)

Eye Protection:
Safety glass with side shields conforming to z87+. (MSDS)

Skin and Body Protection:
Lab personnel working with the chemicals need to wear full-length pants or its equivalent, closed-toe footwear with no skin being exposed, and a lab coat.

Hygiene Measures:
Wash hands after working with the hazardous substances and when leaving the lab/shop.

Respirators may be required under any of the following circumstances:

- As a last line of defense (i.e., after engineering and administrative controls have been exhausted).
- When Permissible Exposure Limit (PEL) will or may be exceeded, or the airborne concentration is unknown.
- Regulations require the use of a respirator.
- There is potential for harmful exposure due to an atmospheric contaminant (in the absence of PEL)
- As PPE in the event of a chemical spill clean-up process

Prior to obtaining a respirator, an exposure assessment of the process or procedure must be conducted. If respiratory protection is required, then lab personnel must obtain respiratory protection training, a medical evaluation, and a respirator fit test through EH&S. This is a regulatory requirement.

First Aid Procedures for Chemical Exposures

If inhaled:
Evacuate the victim to a safe area as soon as possible. Loosen tight clothing such as a collar, tie, belt or waistband. If breathing is difficult, seek medical attention. If the victim is not breathing,

perform mouth-to-mouth resuscitation. WARNING: It may be hazardous to the person providing aid to give mouth-to-mouth resuscitation when the inhaled material is toxic, infectious or corrosive. Seek immediate medical attention.

In case of skin contact:
In case of contact, immediately flush skin with plenty of water for at least 15 minutes while removing contaminated clothing and shoes. Cold water may be used. Wash clothing before reuse. Thoroughly clean shoes before reuse. Get medical attention, as necessary.

In case of eye contact:
Immediately flush eyes with plenty of water for at least 15 minutes. Check for and remove any contact lenses. Get medical attention.

If swallowed:
If the material is ingested, get immediate medical attention or advice. Do not induce vomiting.

Special Handling and Storage Requirements

Handling Procedure:
Do not breathe fumes or dust from this material. Keep this product from heat, sparks, or open flame. Use non-sparking tools when opening and closing container. Wet mop or HEPA vacuum is recommended to clean up any dusts that may be generated during handling and processing. Wash hands and face thoroughly before eating, drinking, or smoking.

Storage Procedure:
Keep the container tightly closed and in a cool, well ventilated place. Store away from incompatible materials. Do not handle or store near open flame, heat or other source of ignition. Good housekeeping and engineering practices should be employed to prevent the generation and accumulation of dusts.

Spill and Accident Procedure

Chemical Spill Dial 911 and 756-6661

Spill – Assess the extent of danger. Help contaminated or injured persons. Evacuate the spill area. Avoid breathing vapors. If safe, confine the spill to a small area using a spill kit or absorbent material. Keep others from entering contaminated area (e.g., use caution tape, barriers, etc.).

Small (<1 L) – If you have training, you may assist in the clean-up effort. Use appropriate personal protective equipment and clean-up material. Double bag spill waste in plastic bags, label and arrange hazardous waste pick-up.

Large (>1 L) – Evacuate spill area. Dial **911** and EH&S at 756-6661 for assistance. Remain available in a safe, nearby location for emergency personnel.

Chemical Spill on Body or Clothes – Remove clothing and rinse body thoroughly in emergency shower for at least 15 minutes. Seek medical attention. *Notify supervisor, advisor or P.I. immediately.*

Chemical Splash Into Eyes – Immediately rinse eyeball and inner surface of eyelid with water from the emergency eyewash station for a minimum of 15 minutes by forcibly holding the eye open. Seek medical attention. *Notify supervisor, advisor or P.I. immediately.*

Medical Emergency Dial 911 or 756-6661

Life Threatening Emergency, After Hours, Weekends And Holidays – Dial 911
Note: All serious injuries must be reported to Supervisor/PI within 8 hours. Note: Any and all loss of consciousness requires a 911 call

Non-Life Threatening Emergency –

- Students: Seek medical attention at the campus Health Center **M, T, Thu, Fr 8:00 am – 4:30 pm and W 9:00 am – 4:30 pm**
- Emergency Medical services in the community are available at any time at hospital emergency rooms and some emergency care facilities.

All injuries must be reported to PI/Supervisor immediately and follow campus injury reporting. Follow procedures for reporting of student, visitor injury on the EH&S website at: http://afd.calpoly.edu/riskmgmt/incidentreporting.asp

- Paid staff, students, faculty: seek initial medical attention for all non-life threatening injuries at:

  - MED STOP, 283 Madonna Road, Suite B (next to See's Candy in Madonna Plaza)
    (805) 549-8880 Hours: M-F 8a - 8p; Sat/Sun 8a - 4p
    After MED Stop Hours: Sierra Vista Hospital Emergency Room
    1010 Murray Avenue (805) 546-7651, Open 24 hours

All injuries must be reported to PI/Supervisor immediately and follow campus injury reporting for employee injuries (Workmen's Comp.). Follow procedures on the EH&S website at: http://afd.calpoly.edu/riskmgmt/incidentreporting.asp

Needle stick/puncture exposure (as applicable to chemical handling procedure) – Wash the affected area with antiseptic soap and warm water for 15 minutes. For mucous membrane exposure, flush the affected area for 15 minutes using an eyewash station. Seek medical attention. *Note: All needle stick/puncture exposures must be reported to supervisor, advisor or P.I. and EH&S office immediately.*

Decontamination/Waste Disposal Procedure

General hazardous waste disposal guidelines:

Label Waste

- Affix a hazardous waste tag on all waste containers as soon as the first drop of waste is added to the container. Generic waste labels can be found here: http://afd.calpoly.edu/ehs/docs/hazwaste_label_template.pdf

Store Waste

- Store hazardous waste in closed containers, in secondary containment and in a designated location
- Double-bag dry waste
- Waste must be under the control of the person generating & disposing of it

Dispose of Waste

- Dispose of regularly generated chemical waste as per guidelines on EH&S website at: http://afd.calpoly.edu/ehs/docs/csb_no6.pdf
- Prepare for transport for pick-up. Use secondary containment.

Call EH&S at 756-6661 for questions.

Empty Containers

- Dispose as hazardous waste if container once held extremely hazardous waste (irrespective of the container size) A list can be found at: http://afd.calpoly.edu/ehs/docs/extremely_hazardous_wastes.pdf
- All other containers are legally empty once a concerted effort is made to remove, pour out, scrape out, or otherwise completely empty the vessel. These may be disposed of as recycling or common trash as appropriate.

Safety Data Sheet (SDS) Location

Online SDS can be accessed at: http://siri.org/msds/index.php

See attached SDS.

Protocol/Procedure

Required Equipment

1. Powder Spreader
2. Powder Scale
3. Computer
4. Camera
5. Ruler
6. Funnel
7. Tray
8. Scale
9. Paint Brush

Standard Operating Procedure

Test Assembly Setup:

1. Place warning signage on entry/exit doors that indicate testing is in progress, and only authorized personnel are permitted in the room with proper PPE

2. Ensure that all non-essential personnel have been escorted from the vicinity.
3. Ensure that all essential personnel are equipped with proper PPE.
4. Place spreader in the fume hood.
5. Make all connections from the computer to the spreader.
6. Place powder in the supply container.
7. Set up camera for a particular video angle.
8. Start up the control system.

General Sweep Process:

1. Signal the supply stage to lift by 10 – 50 μm (depending on test)
2. Signal the coater blade to spread across.
3. Repeat until data collected by camera is sufficient.
4. Reposition camera.
5. Repeat process 1-3 for different camera angles.

Density and Distribution Test:

1. Apply the general sweep process after several layers.
2. Raise the build plate stage to the top of the center insert.
3. Use the ruler to separate out a portion of the powder on the build plate. Move all undesired powder to adjacent wells with the ruler.
4. Spread the portion of desired powder over the build plate.
5. Take photo of the build plate.
6. Repeat steps 1-6 for 5 other portions of the build plate.

Standard Cleanup Procedure

1. Power down all electronic systems except for the fume hood.
2. Ensure that all personnel in the room are wearing PPE.
3. Lift stages all the way up so the build plate sits a few millimeters above the center insert. (See Figure 1)
4. Carefully brush powder into the adjacent catch wells.
5. Take tray out, and using a funnel, carefully pour powder into the original powder container.
6. Place lid on large storage container and store in designated location.
7. Power down fume hood.

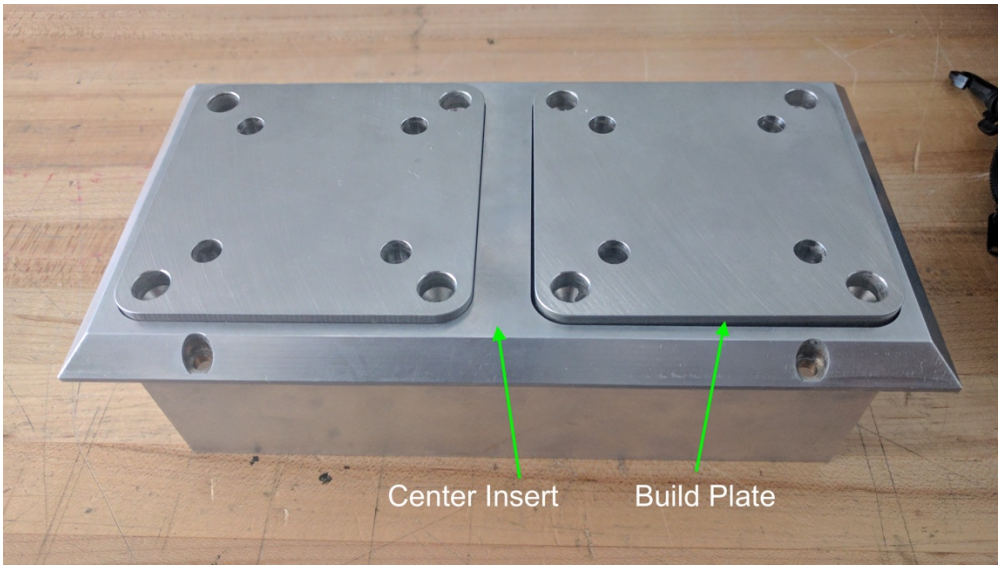

Figure 1. Built plate sitting above the center insert.

Spill Protocol Procedure

Standard Cal Poly EH & S spill procedure can be seen in Spill and Accident Procedure section located on page 4 above.

The following procedure is to be followed when a considerable amount of powder is unintentionally dropped from a height greater than three inches and powder becomes air born and/or is deposited onto the ground.

1. Assess that all members of team are uninjured and safe.
2. Notify supervisor, advisor or P.I., and EH & S to determine following protocol.
3. Wait for approximately 5 minutes until powder settles.
4. Clean up the bulk of the spilled material using a waste tray and a brush (preferably not used for cleaning the experimental apparatus) and deposit the waste powder into a hazardous waste container.
5. Use damp hazardous material rags to wipe down all possible powder contaminated areas, and dispose contaminated rags into a hazardous waste vessel.
6. All gloves should then be deposited into the hazardous waste vessel as well.

NOTE:

Any deviation from this SOP requires approval from PI.

Date: Click here to enter a date. **P.I. or Supervisor:**

Documentation of Training (signature of all users is required)

- The Principal Investigator must ensure that his/her laboratory personnel have attended appropriate laboratory safety training or refresher training within the last one year.

- Training must be administered by PI or Lab Manager to all personnel in lab prior to start of work with particularly hazardous substance or newly synthetic chemical listed in the SOP.

- Refresher training will need to be provided when there is a change to the work procedure, an accident occurs, or repeat non-compliance.

I have read and understand the content, requirements, and responsibilities of this SOP:

Name	Signature	Date

```
%=========================================================================
% IMAGE PROCESSING FOR 316L SS METAL POWDER SURFACE CHARACTERIZATION
%=========================================================================
clc
close all
clear all

%-------------------------------------------------------------------------
% PATH TO BATCH FILE OF INPUT IMAGES
%-------------------------------------------------------------------------
fileFolder = fullfile('~', 'Documents', 'MATLAB', 'Thesis', '2X100', 'Run 6');
dirOutput = dir(fullfile(fileFolder, '*.tiff'));
fileNames = {dirOutput.name}';

%-------------------------------------------------------------------------
% PROCESSING IMAGES
%-------------------------------------------------------------------------
% images will be taken individually from imput directory to be filtered and
% thresholded from a grayscale to a binary image. The binary image will be
% an indication of where the high and low spots are on the surface.

for i = 1:length(fileNames)
    % --------------TOP HAT AND BOTTOM HAT FILTERING----------------------
    % makes the peaks of the image brighter and the valleys darker to
    % increase the contrast in image for better thresholding.

    %OPEN IMAGE
    img0 = imread(fileNames{i});
    img0 = imresize(img0(200:800, 200:800),4);  % resize image to focused area
    img0 = imsharpen(img0);                     % sharpen image

    % FILTERING
    se = strel('disk',5);                       % looks for disks
    tophatfilt = imtophat(img0,se);             % top hat filtering
    bothatfilt = imbothat(img0,se);             % bottom hat filtering

    %  figure;                                  % side by side of filters
    %  imshowpair(tophatfilt,bothatfilt,'montage');
    %  title('tophatfilt and bothatfilt');

    % COMBINE FILTERS
    subtract = imsubtract(imadd(img0,tophatfilt),bothatfilt);
    % add top hat to enhance brightness and subtract darkest areas

    % WRITE TO SEPERATE FOLDER
    [pathstr,name,ext] = fileparts(fileNames{i});
    baseFileName = [name,'.png'];
    fullFileName = fullfile(fileFolder, 'Filtered', baseFileName);
    imwrite(subtract, fullFileName);
%
    % --------------LOCAL THRESHOLDING EXPERIMENT---------------------
    % The image is divided into N divisions specified at the command window.
    %  The image will be divided into N x N divisions, and each sub-division
    %  will be locally thresholded, and then re-stitched into a final
    %  binary image.

    %  % Select sub-image / form divisions for local thresholding
    %  [N,M] = size(subtract);

    %  div = input('Number of Divisions = ');
```

```
    %  x = fix(N/div); %x-size of each division
    %  y = fix(M/div); %y-size of each division
    %  img1 = [];
    %  for sx = 1:x:N-x % pixels in x
    %      for sy = 1:y:M-y % pixels in y
    %          sp = img0(sx:(sx+x-1), sy:(sy+y-1)); %individual image
    %
    %          % THRESHOLDING
    %          T = graythresh(sp); %Otsu method thresholding
    %          spT = im2bw(sp,T); %turning image to binary
    %         img1(sx:(sx+x-1), sy:(sy+y-1)) = spT; %stores values in region of
image
    %     end
    %  end
    % img2 = im2uint8(img1);
    % figure;
    % imshow(img2);
    % title('Local Thresholding at 50 Divisions');

    % ---------------------GLOBAL THRESHOLDING---------------------------
    % Function graythresh uses Otsu's Method to determine a thresholding
    % value from which to binarize the image
    level = graythresh(subtract);
    bw = imbinarize(subtract,level);

    % NOISE REMOVAL FROM BINARY
    % remove all object containing fewer than 10 pixels
    bw = bwareaopen(bw,10);

    %  figure;
    %  imshow(bw);
    %  title('bw');

    % MORPHOLOGICAL CLOSE FROM EROSION AND DILATION
    % smooths out white areas and fills in black areas near borders
    se2 = strel('disk',1);
    bw = imclose(bw,se2);

    % FLOOD FILL ON BACKGROUND PIXELS
    % fill any holes of black pixels surrounded by white, so that
    % regionprops can be used to estimate the area enclosed by each of the
    % boundaries
    bw = imfill(bw,'holes');

    % WRITE FINAL BINARY IMAGE TO FILE
    [pathstr,name,ext] = fileparts(fileNames{i});
    baseFileName = [name,'.png'];
    fullFileName = fullfile(fileFolder, 'Threshold', baseFileName);
    imwrite(bw, fullFileName);

    % ------------------------EDGE DETECTION ----------------------------

    % bw = edge(subtract,'Canny');

    % figure;
    % imshow(bw);
    % title ('image close and fill');

    % ------------------- BWBOUNDARIES FOR VISUALS ----------------------
    % BW = imbinarize(subtract);
    % [B,L] = bwboundaries(subtract,'noholes');
```

```
    % imshow(BW);
    % hold on
    % for k = 1:length(B)
    %     boundary = B{k};
    %     plot(boundary(:,2), boundary(:,1), 'g', 'LineWidth', 1)
    %     title('Boundary Tracing');
    %
    % end
    % hold on
    % ----------------------REGION ANALYSIS ----------------------------
    %Extract areas and centroid data for each object in the image
    stats = regionprops(bw,img0,'Area','Centroid');

    % overlay area data over image
    %figure;
    %imshow(bw);
%     numObj = numel(stats);
%     hold on
%     for k = 1:numObj
%         scale = 736.36/10000; %pixels per cm*cm/10000um
%         stats(k).trueArea = stats(k).Area*(1/scale)^2;
%         %plot(stats(k).Centroid(1), stats(k).Centroid(2), 'b*');
%         text(stats(k).Centroid(1), stats(k).Centroid(2),...
%             sprintf('%2.0f',stats(k).trueArea),...
%             'Color','r');
%     end
%     hold off

    % Finding bright to dark ratio
    pixelarea = [stats.Area];   % Area of the white pizels in the image
    B = sum(pixelarea(:));      % Sum of all white areas
    [x,y] = size(bw);           % Size of images
    E = x*y-B;                  % Dark pixels

    R{i,1} = name;              % label right column with image name
    R{i,2} = B/E;               % Ratio of bright to dark


%     formatSpec = 'Ratio of bright to dark for %s is %10f\r\n';
%     fileID = fopen('Ratio.txt','a');
%     fprintf(fileID, formatSpec, name,R);


    % area of bright spots
    area{i} = [stats.Area];     % lists all bright spots
end
%-------------------------------------------------------------------------
% GRAPHS AND VISUALS
%-------------------------------------------------------------------------
% --------------------ROUGHNESS SURFACE IMAGE ---------------------
    % Visual representation of the surfaces from the gray scale image. Not
    % true representation since there is no height value to correspond to
    % intensity.

    [x,y] = size(img0);
    X = 1:x;
    Y = 1:y;
    [xx,yy] = meshgrid(Y,X);
    result = [xx(:),yy(:),img0(:)];
    j=im2double(img0);
    j = j*0.05;
    figure;
```

```
    mesh(j);

    %  a = xx(:);
    %  b = yy(:);
    %  c = subtract(:);
    % surf(a,b,c,'filled');
    axis([0 x 0 y -0.1 0.3]);


%----------------------------HISTOGRAM----------------------------------
%
[k,l] = size(fileNames); % Histogram of every 9 runs in a graph

histnum = k/9;

for i = 1:histnum;
    h = figure;
    set(h, 'Visible', 'off');
    nhist(area(9*i-8:9*i),'noerror','number','legend', {'1','2','3','4',...
        '5','6','7','8','9'},'fsize',9);
    baseFileName2 = sprintf('%d.png',i);
    fullFileName2 = fullfile(fileFolder, 'Histogram', baseFileName2);
    saveas(h, fullFileName2);
end
% ------------------SCATTER AND MEAN/STD GRAPH FOR B/D--------------------

R_num = cell2mat(R(:,2));           % cell array to values
E = reshape(R_num,9, []);           % reorder to rows = section, column = run
T1 = E(1,:);                        % Values in the 1 region, etc.
T2 = E(2,:);
T3 = E(3,:);
T4 = E(4,:);
T5 = E(5,:);
T6 = E(6,:);
T7 = E(7,:);
T8 = E(8,:);
T9 = E(9,:);

T_sum = [];
T_sum(3,3) = mean(T9); % mean value for each column
T_sum(3,2) = mean(T8);
T_sum(3,1) = mean(T7);
T_sum(2,1) = mean(T6);
T_sum(2,2) = mean(T5);
T_sum(2,3) = mean(T4);
T_sum(1,3) = mean(T3);
T_sum(1,2) = mean(T2);
T_sum(1,1) = mean(T1);

T_std = [];
T_std(3,3) = std(T9); % std dev value for each column
T_std(3,2) = std(T8);
T_std(3,1) = std(T7);
T_std(2,1) = std(T6);
T_std(2,2) = std(T5);
T_std(2,3) = std(T4);
T_std(1,3) = std(T3);
T_std(1,2) = std(T2);
T_std(1,1) = std(T1);

T_inv = 1./T_sum; % B/D is greater if the surface is smooth, for
```

```
                % visualization purposes values are inverted so rougher is
greater

Z =(T_sum - min(T_sum(:)))./(max(T_sum(:)) - min(T_sum(:))); % normalizing

figure;
b = bar3(Z);
title({'Normalized Averages of B/D values of Each Region';'Dose-2X Speed-100
mm/s Run 2'});
colorbar;
for k = 1:length(b)
    zdata = b(k).ZData;
    b(k).CData = zdata;
    b(k).FaceColor = 'interp';
end



% D_inv = 1./E;               % inv to show increasing values as increasing
roughness
% Z1 = (D_inv - min(D_inv(:)))./(max(D_inv(:)) - min(D_inv(:)));
%
% figure;
% c = bar3(Z1);
% colorbar;
% for k = 1:length(c)
%     edata = c(k).ZData;
%     c(k).CData = edata;
%     c(k).FaceColor = 'interp';
% end

%
%D = transpose(E);    % 9 columns
C(:,2)= reshape(E, [],1);   % one vector of values

% Preparing data points for scatter graphing
row = 1;
for i = 1:length(C)         % append column value to first column of C
    C(i,1) = row;
    row = row+1;
    if row >= 10
        row = 1;
    end
end

save('C2X100R2.mat','C'); % to combine with othe runs

C_avg =[];               % reorganize values into one matrix
for i=1:9
    C_avg(i,1) = i;
    C_avg(i,2) = mean(E(i,:));
    C_avg(i,3) = std(E(i,:));
end

save('C2X100R2avg.mat','C_avg');

% Plot scatter dot plot with regions
figure;
scatter(C(:,1),C(:,2),'x','k');
hold on
scatter(C_avg(:,1),C_avg(:,2),'r','filled');
hold on
```

```
errorbar(C_avg(:,1),C_avg(:,2),C_avg(:,3),'r','LineStyle','none');
box on
xlabel('Powder Bed Region');
ylabel('B/D');
title({'B/D: Dose-2X Speed-100 mm/s','Run 2'});
xlim([0 10]);
ylim([0.24 0.5]);
set(gca, 'XTick',[1:1:9],'YTick', [0.24:0.02:0.5]);
set(0,'defaultAxesFontSize', 12,'defaultAxesFontName','Times New Roman');
set(0,'defaultAxesXColor','k','defaultAxesYColor','k');

% ------------------PXIXEL AREA MEAN AND STD DEV GRAPH -------------------

area = reshape(area,9, []);
Area_1 = cell2mat(area(1,:));          % cell array to values
Area_2 = cell2mat(area(2,:));
Area_3 = cell2mat(area(3,:));
Area_4 = cell2mat(area(4,:));
Area_5 = cell2mat(area(5,:));
Area_6 = cell2mat(area(6,:));
Area_7 = cell2mat(area(7,:));
Area_8 = cell2mat(area(8,:));
Area_9 = cell2mat(area(9,:));


Area_avg = [];
Area_avg(:,1) = [1:1:9];

Area_avg(1,2) = mean(Area_1);
Area_avg(2,2) = mean(Area_2);
Area_avg(3,2) = mean(Area_3);
Area_avg(4,2) = mean(Area_4);
Area_avg(5,2) = mean(Area_5);
Area_avg(6,2) = mean(Area_6);
Area_avg(7,2) = mean(Area_7);
Area_avg(8,2) = mean(Area_8);
Area_avg(9,2) = mean(Area_9);

Area_avg(1,3) = std(Area_1);
Area_avg(2,3) = std(Area_2);
Area_avg(3,3) = std(Area_3);
Area_avg(4,3) = std(Area_4);
Area_avg(5,3) = std(Area_5);
Area_avg(6,3) = std(Area_6);
Area_avg(7,3) = std(Area_7);
Area_avg(8,3) = std(Area_8);
Area_avg(9,3) = std(Area_9);

save('area2X100R2.mat','Area_avg');


figure;
errorbar(Area_avg(:,1),Area_avg(:,2),zeros(1,9),Area_avg(:,3),'b', 'LineStyle',
'none');
hold on
scatter(Area_avg(:,1),Area_avg(:,2),50, '*','b');
xlim([0 10]);
xticks([1:1:9]);
xlabel('Powder Bed Region');
ylabel('Pixel Area');
title({'Pixel Area: Dose-2X Speed-100 mm/s', 'Run 2'});
```

```
%--------------------------------------------------------------------------
%OTHER THINGS THAT DIDN'T WORK
%--------------------------------------------------------------------------

% -------------Experiment with dilation and erode----------------------
% se = strel('disk', 1,0);
% BI_1=imclose(BW3_1,se);
% BW4_1 = imdilate(BW3_1,strel('disk',3));
% BW4_2 = imerode(BW4_1,strel('disk',3));
% BW4_3 = imfill(BW4_2,'holes');
%
% figure;
% imshowpair(BI_1,BW4_3,'montage');
% title ('image close and fill');

%--------------Iterative Dilation to close edges-----------------------
% So, let's try closing them by iterative dilations
% cc = bwconncomp(BW4_1);
% BWblank = false(cc.ImageSize);
% stats = regionprops(cc,'ConvexImage','EulerNumber');
% for i = find([stats.EulerNumber]>0)
%     distIm = bwdist(~stats(i).ConvexImage);
%     maxClose = ceil(max(distIm(:)));
%     BWslice = BWblank;
%     BWslice(cc.PixelIdxList{i}) = true;
%     if isinf(maxClose), continue; end;
%     for dilSz = 2:maxClose
%         BWnew = imdilate(BWslice,ones(dilSz));
%         statsNew = regionprops(BWnew,'EulerNumber');
%         if statsNew.EulerNumber<=0
%             BWnew = imerode(imfill(BWnew,'holes'),ones(dilSz));
%             cc.PixelIdxList{i} = find(BWnew);
%         end
%     end
% end
% figure, imagesc(imfill(labelmatrix(cc),'holes')), drawnow
% % That got almost all of them. Some are left over where the dilation itself
% % filled everything so the euler number stayed at 1. Let's just replace
% % those with their convex hull
% stats = regionprops(cc,'ConvexImage','EulerNumber','BoundingBox');
% for i = find([stats.EulerNumber]>0)
%     maxClose = ceil(max(distIm(:)));
%     BWslice = BWblank;
%     BWslice(cc.PixelIdxList{i}) = true;
%     distIm = bwdist(~BWslice);
%     if ~any(distIm(:)>1)
%         BWnew = BWslice;
%         bb = ceil(stats(i).BoundingBox);
%         BWnew((1:bb(4))+bb(2)-1,(1:bb(3))+bb(1)-1) = stats(i).ConvexImage;
%         cc.PixelIdxList{i} = find(BWnew);
%     end
% end
% L = imfill(labelmatrix(cc),'holes');
% figure, imagesc(L)
% % Now we know that any blobs surrounded by other blobs are actually holes
% indsOfHoles =
find(arrayfun(@(i)mode(double(L(bwmorph(L==i,'dilate',1)&~(L==i)))),1:cc.NumObj
ects));
% L(ismember(L,indsOfHoles)) = 0;
% figure, imagesc(L)
%
```

```
%----------------------bwperim - for one blob--------------------------

% layover = bwperim(subtract);
% figure;
% imshow(layover);
%
% SegoutR = img2;
% SegoutG = img2;
% SegoutB = img2;
% SegoutR(layover) = 0;
% SegoutG(layover) = 0;
% SegoutB(layover) = 220;
% SegoutRGB = cat(3, SegoutR, SegoutG, SegoutB);
% figure;
% imshow(SegoutRGB);

% %% bwulterode
% % performs ultimate erosion - not needed
% img2 = imread('4M.tiff');
% bw = adapthisteq(img2);
% ultimateErosion = bwulterode(bw);
% figure;
% imshow(ultimateErosion)
%



%---------------- Watershed segmentation-----------------------------------

% hy = fspecial('sobel');
% hx = hy';
% Iy = imfilter(double(BW4), hy, 'replicate');
% Ix = imfilter(double(BW4), hx, 'replicate');
%
% gradmag = sqrt(Ix.^2+Iy.^2);
% figure
% imshow(gradmag,[]);
%------------------ Comparison to straight binary----------------------

% I2 = imread('4M.tiff');
% compar = imadjust(I2, stretchlim(I2), [0 1]);
% level = graythresh(compar);
% compar2 = im2bw(compar,level);
% imshow(compar2);
%
% comparedge = edge(compar2,'Sobel',[0.15]);
% figure (1);
% imshowpair(compar,comparedge,'montage');
% title('Edge Detection w/ Sobel Filter');
%
% comparse = strel('disk', 1,0);
% comparclose = imclose(comparedge, comparse);
% comparfill = imfill(comparclose,'holes');
% figure(6);
% imshow(comparfill);
% title('compare');
%-------------comparisons using localized filtering and regular----------
% figure;
% imshowpair(tophatfilt,bothatfilt,'montage');
% title('tophatfilter and bothatfilter');
```

```
%
% figure;
% imshowpair(contrastAdj,contrastAdj1,'montage');
% title('contrast adjustment top hat');
%
%
% figure;
% imshowpair(bothatfilt,bothatfilt1,'montage');
% title('tbottom hat filter');
%
% figure;
% imshowpair(contrastAdjb,contrastAdjb1,'montage');
% title('contrast adjustment bottomhat filter');
%
% figure
% imshowpair(subtract3,subtract4,'montage');
% title('final unlocalized vs localized');

%random contour plot
%step = imcontour(subtract2);

% %% bwmorph test #fail
% bwmorph1 = bwmorph(img2,'remove');
% imshow(bwmorph1);
```

APPENDIX D. GRAPHS

D.1 B/D and Pixel Area Mean and Standard Deviation Graphs

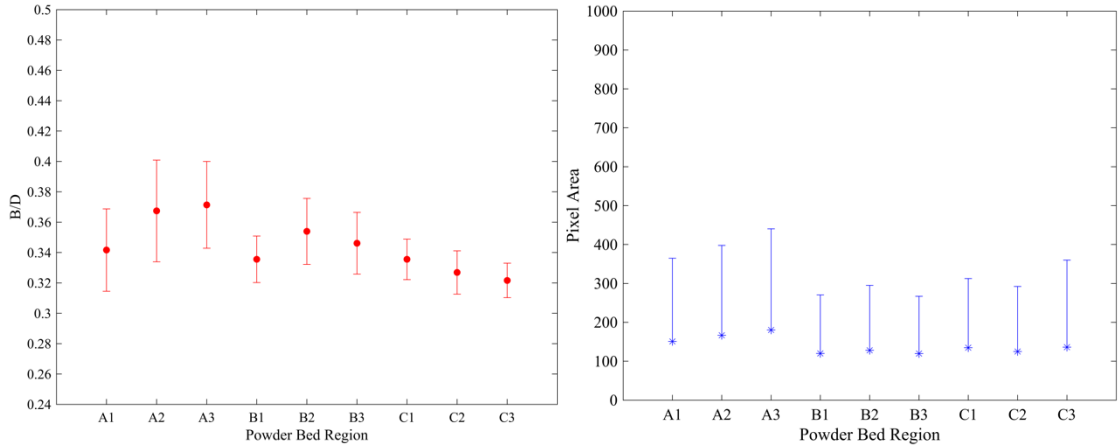

(a) B/D, Dose: 2X Speed: 100 mm/s (b) Pixel Area, Dose: 2X Speed: 100 mm/s

Figure D-1. B/D and Pixel area mean and standard deviation for a dose of 2X and a speed of 100 mm/s. This is Run 1 of 2.

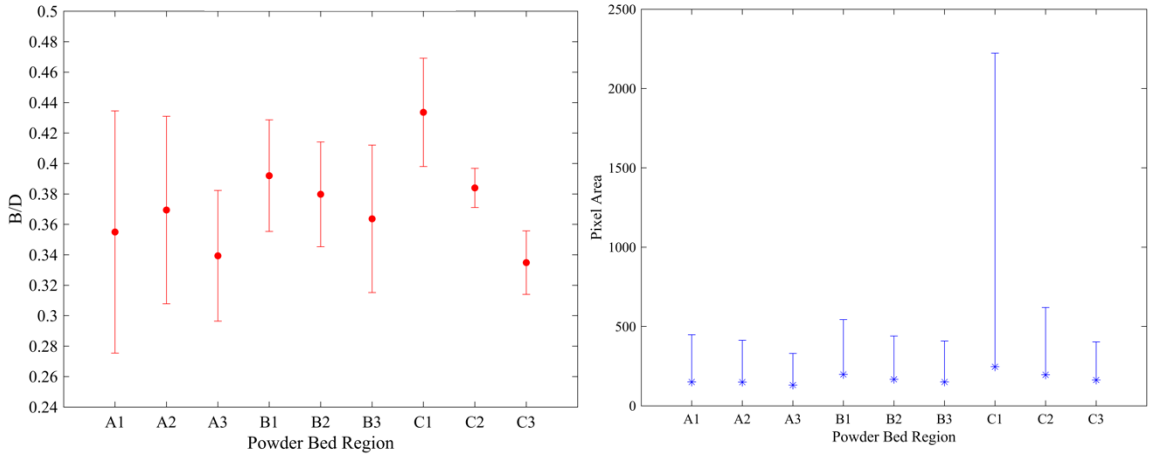

(a) B/D, Dose: 2X Speed: 100 mm/s (b) Pixel Area, Dose: 2X Speed: 100 mm/s

Figure D-2. B/D and Pixel area mean and standard deviation for a dose of 2X and a speed of 100 mm/s. This is Run 2 of 2.

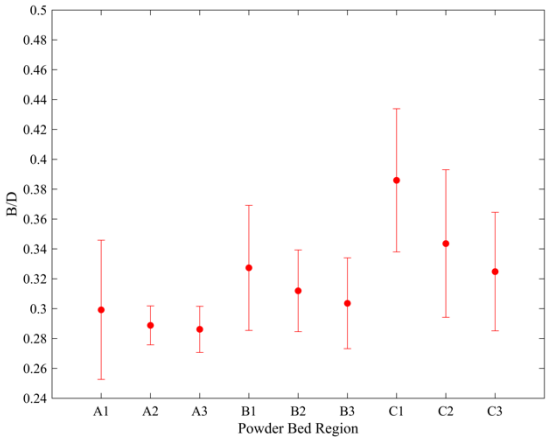

(a) B/D, Dose: 2X Speed: 200 mm/s

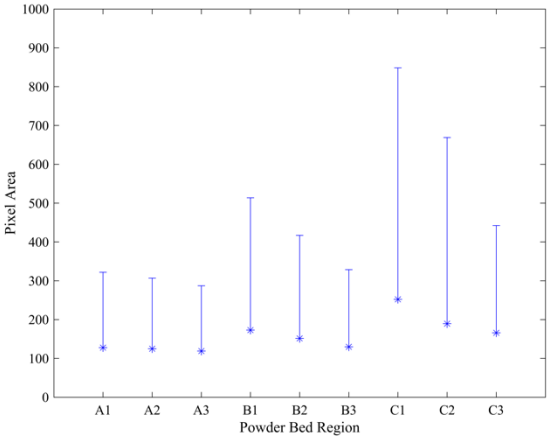

(b) Pixel Area, Dose: 2X Speed: 200 mm/s

Figure D-3. B/D and Pixel area mean and standard deviation for a dose of 2X and a speed of 200 mm/s.

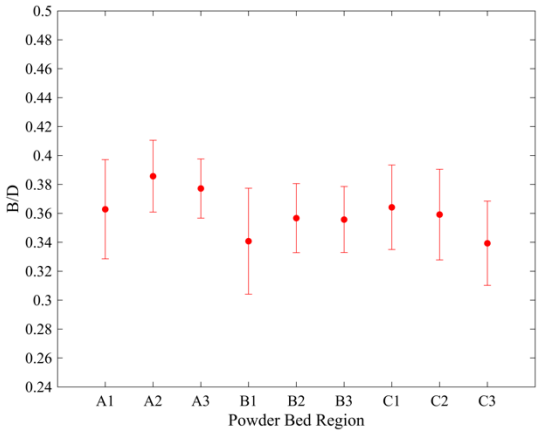

(a) B/D, Dose: 3X Speed: 100 mm/s

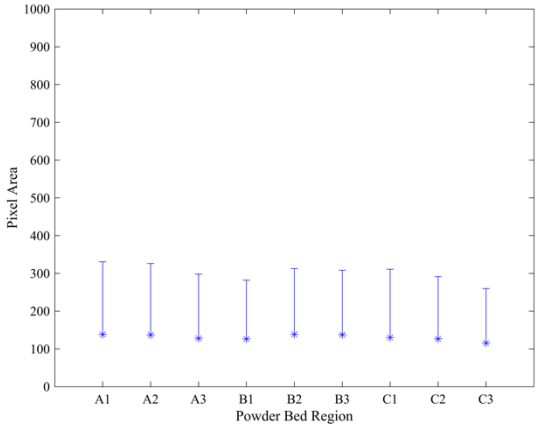

(b) Pixel Area, Dose: 3X Speed: 100 mm/s

Figure D-4. B/D and Pixel area mean and standard deviation for a dose of 3X and a speed of 100 mm/s. This is Run 1 of 2.

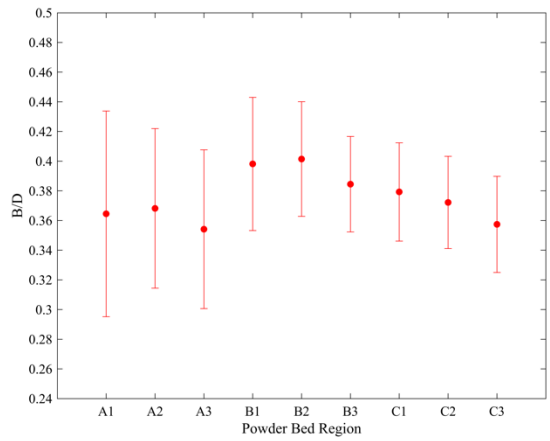

(a) B/D, Dose: 3X Speed: 100 mm/s

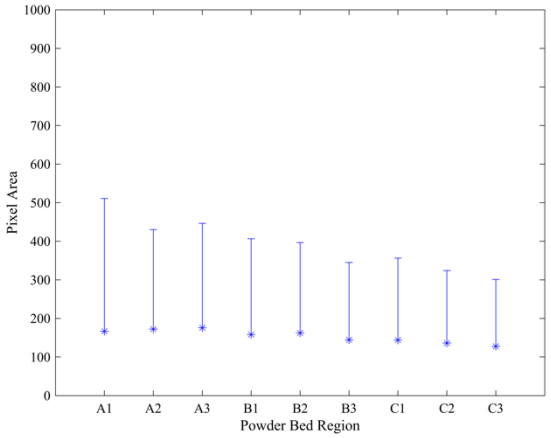

(b) Pixel Area, Dose: 3X Speed: 100 mm/s

Figure D-5. B/D and Pixel area mean and standard deviation for a dose of 3X and a speed of 100 mm/s. This is Run 2 of 2.

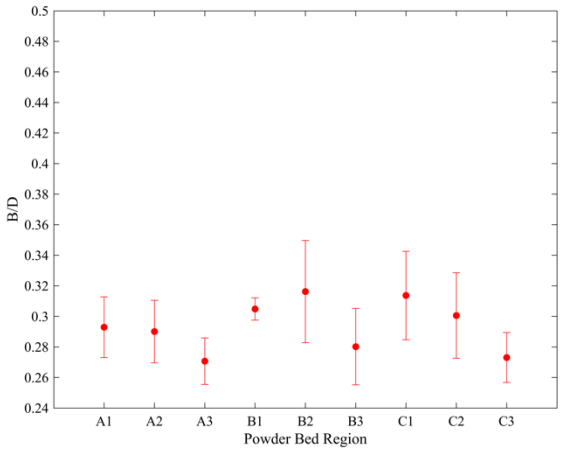

(a) B/D, Dose: 3X Speed: 200 mm/s

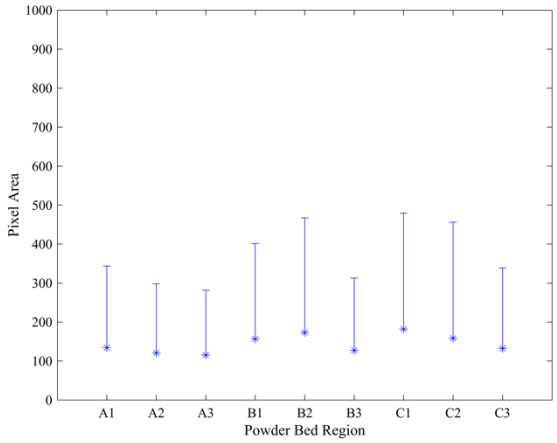

(b) Pixel Area, Dose: 3X Speed: 200 mm/s

Figure D-6. B/D and Pixel area mean and standard deviation for a dose of 3X and a speed of 200 mm/s.

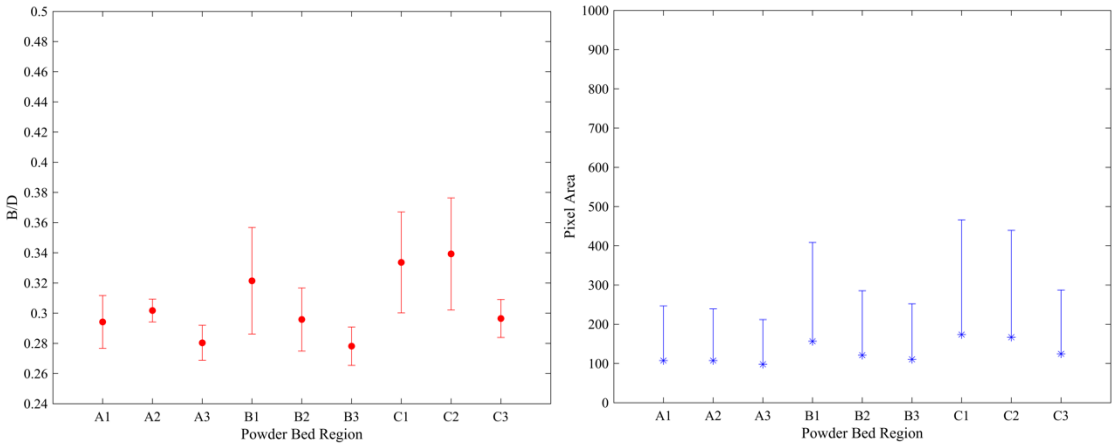

(a) B/D, Dose: 4X Speed: 100 mm/s (b) Pixel Area, Dose: 4X Speed: 100 mm/s

Figure D-7. B/D and Pixel area mean and standard deviation for a dose of 4X and a speed of 100 mm/s. This is Run 1 of 2.

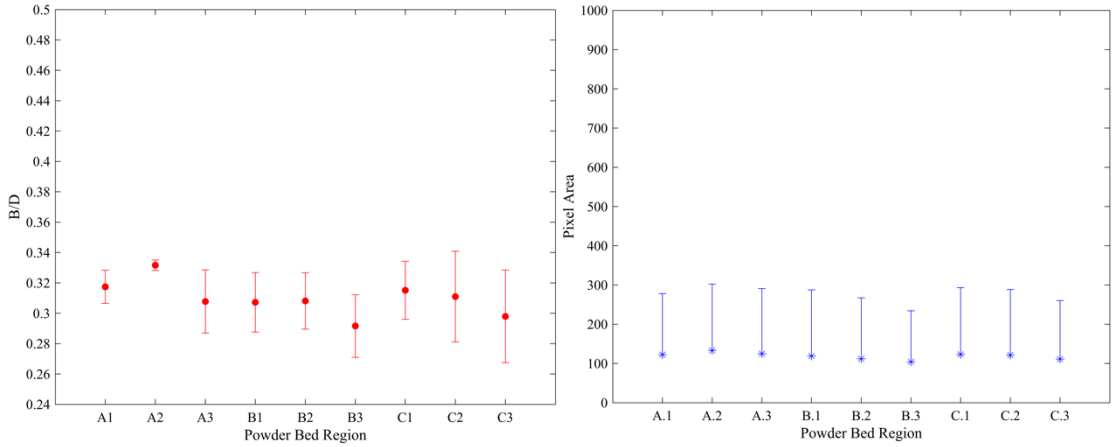

(e) B/D, Dose: 4X Speed: 100 mm/s (b) Pixel Area, Dose: 4X Speed: 100 mm/s

Figure D-8. B/D and Pixel area mean and standard deviation for a dose of 4X and a speed of 100 mm/s. This is Run 2 of 2.

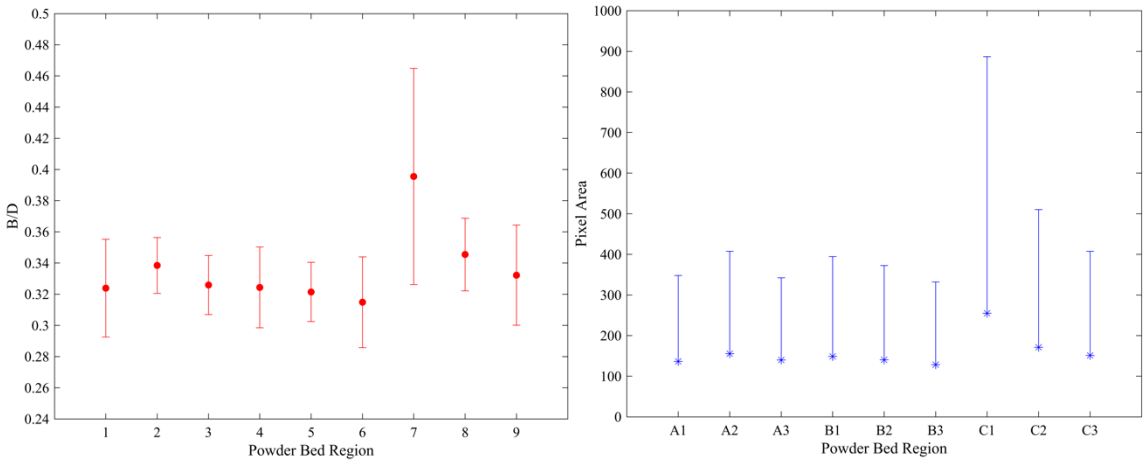

(a) B/D, Dose: 4X Speed: 200 mm/s (b) Pixel Area, Dose: 4X Speed: 200 mm/s

Figure D-9. B/D and Pixel area mean and standard deviation for a dose of 4X and a speed of 200 mm/s.

D.2 Normalized Bar Plots of Average B/D Values

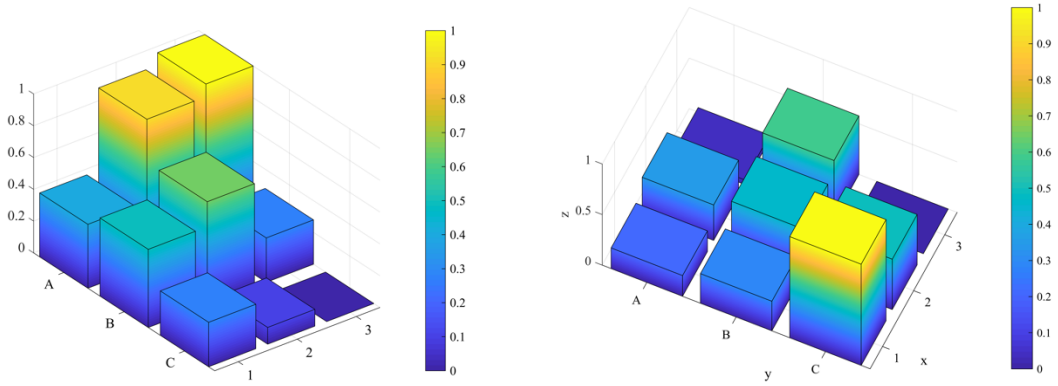

(a) Run 1 (b) Run 2

Figure D-10. Normalized B/D values for a dose rate of 2x and a speed of 100 mm/s.

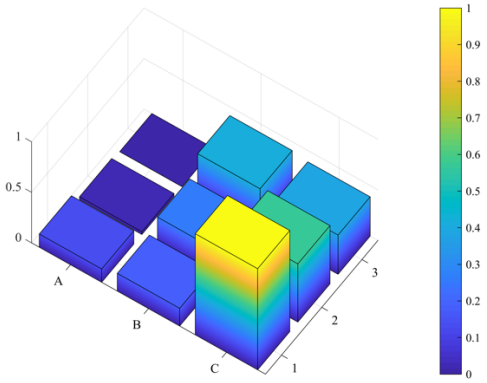

Figure D-11. Normalized B/D values for a dose rate of 2x and a speed of 200 mm/s.

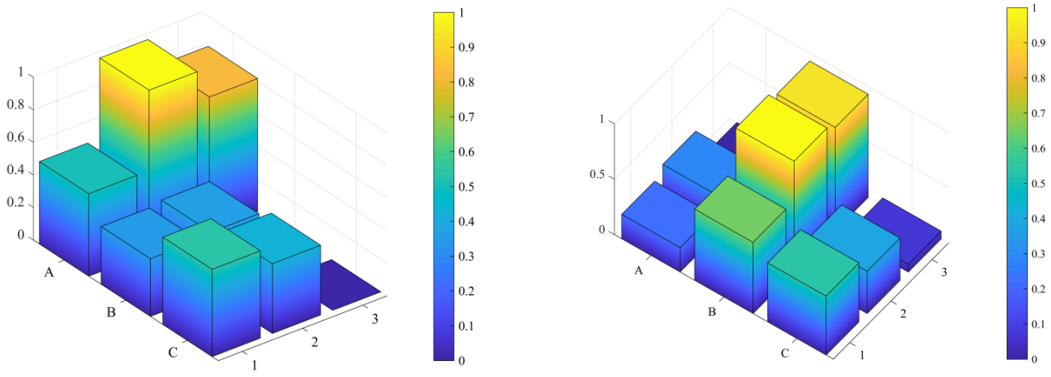

(a) Run 1 (b) Run 2

Figure D-12. Normalized B/D values for a dose rate of 3x and a speed of 100 mm/s.

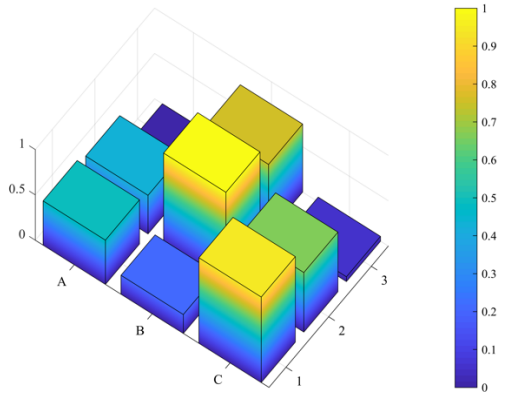

Figure D-13. Normalized B/D values for a dose rate of 3x and a speed of 200 mm/s.

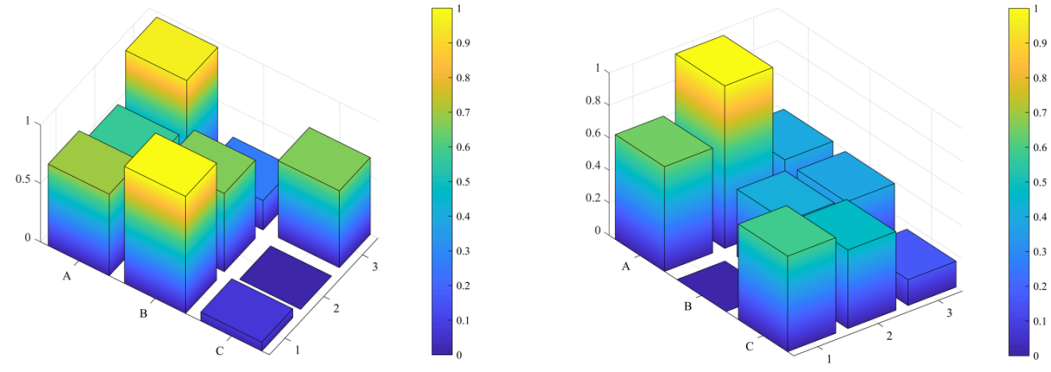

(a) Run 1 (b) Run 2

Figure D-14. Normalized B/D values for a dose rate of 4x and a speed of 100 mm/s.

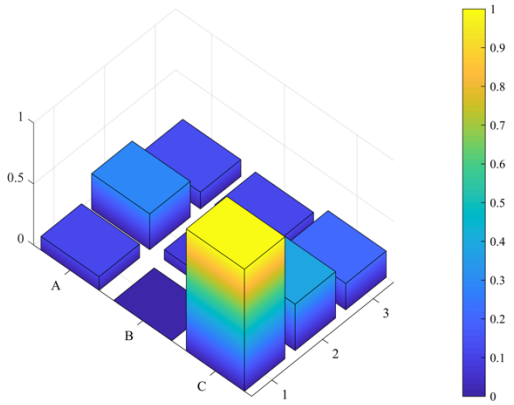

Figure D-15. Normalized B/D values for a dose rate of 4x and a speed of 200 mm/s.

APPENDIX E. LIGGGHTS INPUT FILE

```
### Powder Bed Fusion Simulations - insert/stream
### This simulation pushes powder of a certain thickness over to a build plate.
### Particles are x10 the size of the actual particles in the distribution. The particle is generated, and
### then given time to settle. Once settled, the blade will push the powder over.

### Initialization ----------------------------------------------------------

#Preliminaries
units                   micro
atom_style              granular
boundary                m m m
newton          off
communicate             single vel yes


# Declare Domain
#region domain block  -37500 37500 -20000 20000 -1000 31000 units box
region domain block  -27500 27500 -15000 15000 -1000 20000 units box
create_box 2 domain

# Neighbor Listing
neighbor        0.3 bin
neigh_modify    delay 0

### Setup -------------------------------------------------------------------

# Material and interaction properties required, need to check
Fix     m1 all property/global youngsModulus peratomtype 2e4 0.69e4 # type 1-particle, type 2-wall
fix     m2 all property/global poissonsRatio peratomtype 0.28 0.35
fix     m3 all property/global coefficientRestitution peratomtypepair 2 0.6 0.5 0.5 0.5 #particle-particle,
        particle-wall1
fix     m4 all property/global coefficientFriction peratomtypepair 2 0.6 0.6 0.6 0.8
#fix    m5 all property/global coefficientRollingFriction peratomtypepair  2 0.001 0.003 0.003 0.005
fix     ced all property/global cohesionEnergyDensity peratomtypepair 2 50 50 50 50

# Particle insertion
fix     pts1 all particletemplate/sphere 24671 atom_type 1 density constant 4 radius constant 50
fix     pts2 all particletemplate/sphere 25373 atom_type 1 density constant 4 radius constant 100
fix     pts3 all particletemplate/sphere 25913 atom_type 1 density constant 4 radius constant 150
fix     pts4 all particletemplate/sphere 25951 atom_type 1 density constant 4 radius constant 200
fix     pts5 all particletemplate/sphere 25583 atom_type 1 density constant 4 radius constant 250
fix     pts6 all particletemplate/sphere 26479 atom_type 1 density constant 4 radius constant 300
fix     pts7 all particletemplate/sphere 26891 atom_type 1 density constant 4 radius constant 350
fix     pts8 all particletemplate/sphere 32452867 atom_type 1 density constant 4 radius constant 400
fix     pts9 all particletemplate/sphere 49979687 atom_type 1 density constant 4 radius constant 450

fix     pdd all particledistribution/discrete/numberbased 15485867 9 pts1 0.05655 pts2 0.3613 &
        pts3 0.45 pts4 0.11 pts5 0.02 pts6 0.002 pts7 0.0001 pts8 0.000045 pts9 0.000005
region  pbox block 3000 22000 -10000 10000 0 3000 units box
```

```
group    nve_group region pbox
#fix     ins_mesh all mesh/surface file factorypbf2.stl type 1 scale 10000
fix      ins nve_group insert/pack seed 123457 distributiontemplate pdd maxattempt 200 &
         insert_every once all_in yes overlapcheck yes volumefraction_region 0.4 region pbox

# Import mesh from cad
fix      cad1 all mesh/surface file pbfbase2.stl type 2 scale 10000 curvature 1e-5
fix      cad2 all mesh/surface file blade2.stl type 2 scale 10000 curvature 1e-5
fix      cad3 all mesh/surface file retainer2.stl type 2 scale 10000 curvature 1e-5

# Use imported mesh as granular wall
fix      geometry all wall/gran model hertz tangential history mesh n_meshes 3 meshes cad1 cad2 cad3
         #rolling_friction cdt cohesion sjkr
fix      sidewall1 all wall/gran model hertz tangential history primitive type 2 yplane -20000
fix      sidewall2 all wall/gran model hertz tangential history primitive type 2 yplane 20000

# Define physics
pair_style       gran model hertz tangential history cohesion sjkr #rolling_friction cdt
pair_coeff       * *

### Detailed Settings ----------------------------------------------------------------------------------------

# Integrator
fix integrate all nve/sphere

# Gravity
fix grav all gravity 9.81e-6 vector 0.0 0.0 -1.0

# Time step
timestep 0.1

# Check timestep
fix      timecheck all check/timestep/gran 1 0.1 0.1
run      1
unfix    timecheck

# Thermodynamic output settings
thermo_style     custom step atoms ke cpu
thermo           10000
thermo_modify    lost warn norm no

# Surface Roughness
#compute          zheight all property/atom z
#variable         ztop atom "c_zheight < 15"
#variable         Ra equal ave(v_ztop)
#run 100000 every 1000 "print '$Ra' Ra.dat"

# Dump output
dump     dumpstl all stl 10000 dump*.stl
dump     dmp all custom 10000 dump.1 id type type x y z ix iy iz vx vy vz fx fy fz omegax omegay omegaz
radius
```

```
### Execution and further settings ----------------------------------------------------------------------------------

# Run 1 sec to insert and settle particles
run                 400000 upto

# Delete atoms above desired height
region              del block 3000 22000 -10000 10000 1500 3000 units box
delete_atoms        region del compress yes

# Start remove retainer Blade
unfix       geometry
fix         geometry all wall/gran model hertz tangential history mesh n_meshes 2 meshes cad1 cad2
            # cohesion sjkr rolling_friction cdt
fix         movecad all move/mesh mesh cad2 linear -0.1 0. 0.

#Run
run 3000000
```

APPENDIX F. PARTICLE DISTRIBUTION DATA

F.1 Sample Particle Distribution Statistics

Figure F-1. Selected Statistics from R3: Dose - 2X, Speed - 100 mm/s

Sample	Average CE Diameter (µm)	D[n,0.5] Diameter (µm)	D[v,0.5] Diameter (µm)	Aspect Ratio	Circularity
1-R3	21.80	21.02	27.77	0.88	0.96
2-R3	23.40	22.34	29.11	0.87	0.96
3-R3	20.85	20.56	27.89	0.88	0.96
4-R3	23.21	22.07	28.20	0.87	0.96
5-R3	22.10	21.09	26.87	0.88	0.97
6-R3	22.22	21.24	27.77	0.88	0.97
7-R3	22.37	21.30	27.77	0.88	0.97
8-R3	21.84	20.98	28.06	0.88	0.96
9-R3	21.29	20.44	27.66	0.88	0.97

Figure F-2. Selected Statistics from R4: Dose - 3X, Speed - 100 mm/s

Sample	Average CE Diameter (µm)	D[n,0.5] Diameter (µm)	D[v,0.5] Diameter (µm)	Aspect Ratio	Circularity
1-R4	21.64	20.58	26.92	0.88	0.97
2-R4	22.22	21.21	27.05	0.88	0.97
3-R4	20.78	20.02	27.36	0.88	0.97
4-R4	22.00	21.16	27.85	0.88	0.96
5-R4	21.69	20.62	27.12	0.88	0.97
6-R4	22.30	21.19	27.23	0.88	0.96
7-R4	22.17	21.04	27.51	0.88	0.96
8-R4	21.62	20.63	27.17	0.88	0.97
9-R4	21.51	20.34	26.58	0.88	0.97

Figure F-3. Selected Statistics from R5: Dose - 3X, Speed - 100 mm/s

Sample	Average CE Diameter (µm)	D[n,0.5] Diameter (µm)	D[v,0.5] Diameter (µm)	Aspect Ratio	Circularity
1-R5	21.78	20.96	27.90	0.88	0.96
2-R5	22.23	21.35	27.95	0.88	0.97
3-R5	20.61	19.68	25.40	0.89	0.97
4-R5	19.83	19.35	25.39	0.88	0.97
5-R5	22.40	21.32	27.48	0.88	0.93
6-R5	22.20	21.00	27.53	0.88	0.97
7-R5	20.33	19.89	26.13	0.88	0.97
8-R5	20.37	19.99	27.19	0.88	0.96
9-R5	21.70	20.82	27.09	0.88	0.97

F.2 Number Percent Distribution Graphs

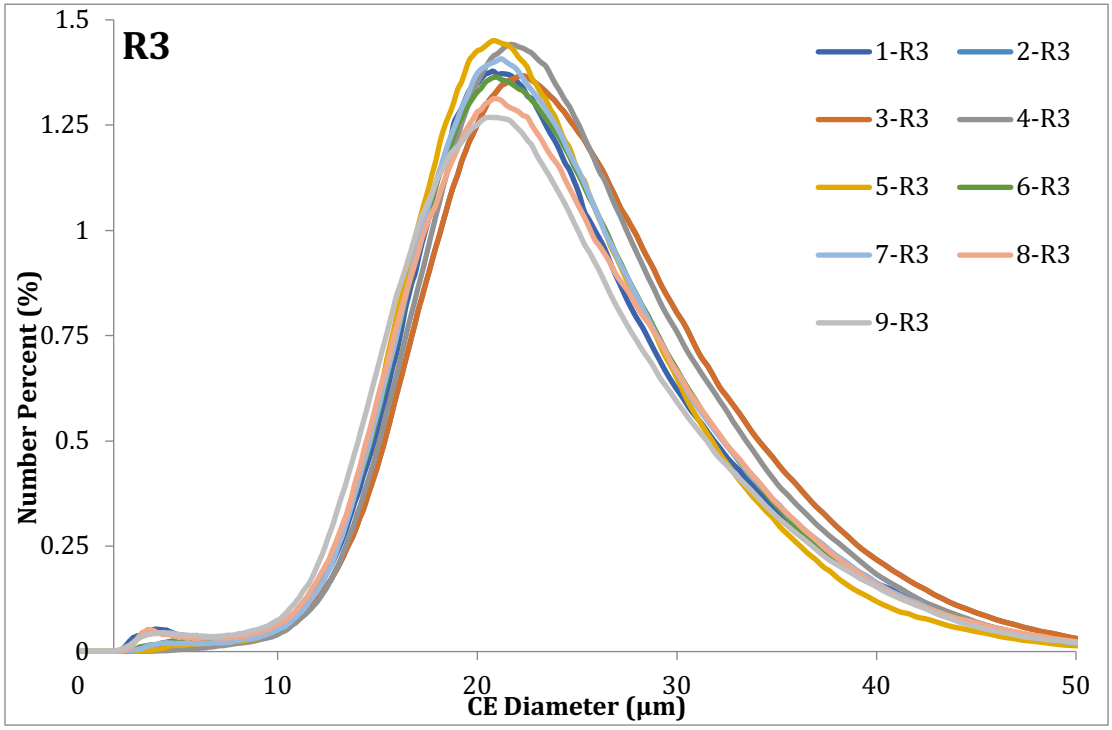

Figure F-4. CE Diameter by number percent for R3: Dose - 2X, Speed - 100 mm/s.

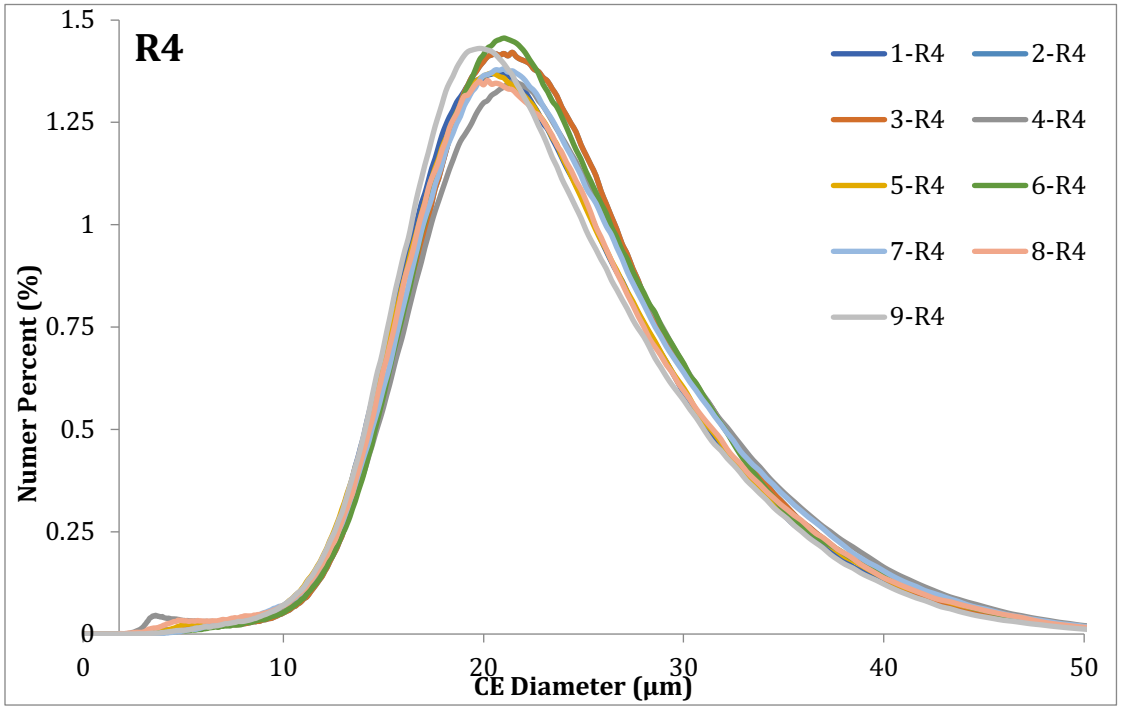

Figure F-5. CE diameter by number percent for R4: Dose - 3X, Speed - 100 mm/s

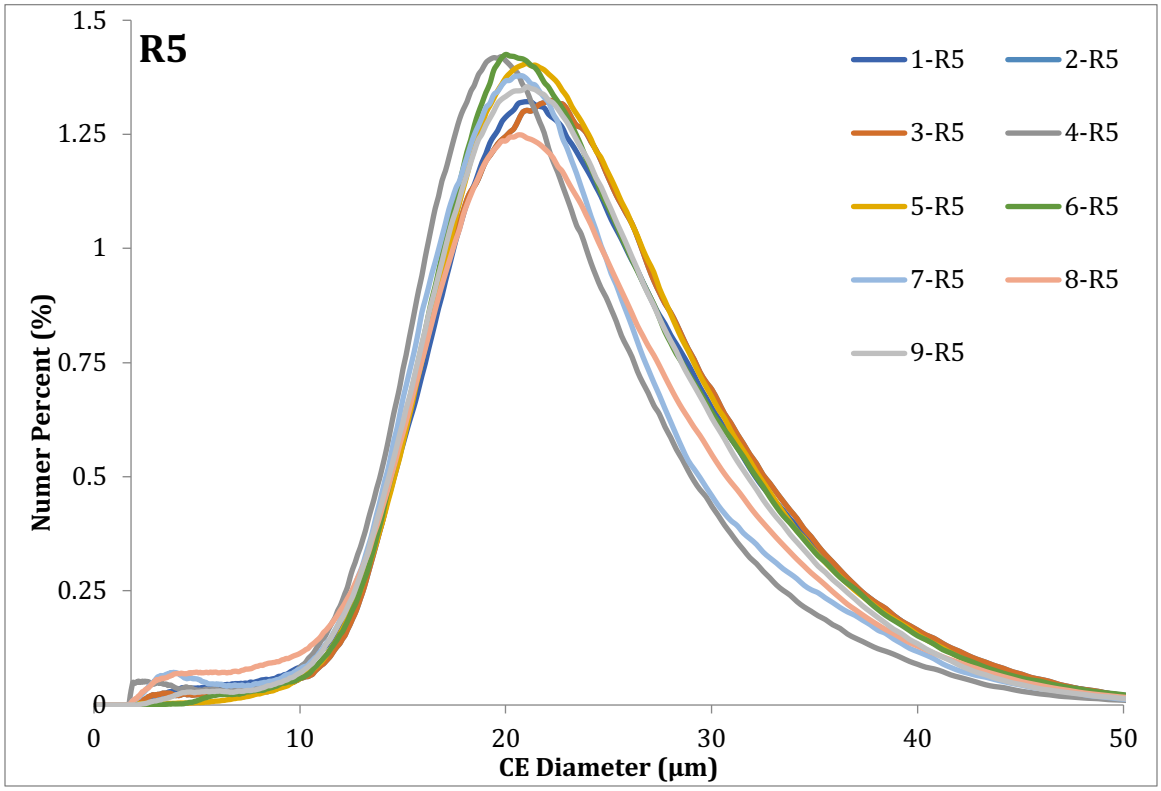

Figure F-6. CE diameter by number percent for R5: Dose - 3X, Speed - 100 mm/s.